High Frequency Acoustic Properties of Urea Ice

A Thesis
Submitted to the Faculty
in partial fulfillment of the requirements for
the degree of

Master of Engineering

by

Mustafa Akbaraly Vahanvaty

Thayer School of Engineering
Dartmouth College
Hanover, New Hampshire

JUNE 1990

Examining Committee:

_____
Prof. Robert Crane

_____
Dr. Kenneth Jezek

_____
Dr. Anthony Gow

_____
Prof. Vijay Gupta

_____
Dean Charles Hutchinson

_____
Mustafa A. Vahanvaty

Thayer School of Engineering
Dartmouth College

High Frequency Acoustic Properties of Urea Ice

Mustafa A. Vahanvaty

Master of Engineering

ABSTRACT

The objective of this experiment was to describe the high frequency acoustic backscatter from simulated arctic sea ice as a function of the physical properties of the ice. In addition, diffraction experiments were performed on the edge of an open lead. These edges are acoustically interesting because saline ice both supports shear waves and is highly absorptive. Experiments were carried out on urea ice grown under controlled laboratory conditions in the cold pit at the Cold Regions Research and Engineering Laboratory, Hanover, New Hampshire. Normal incidence sonar echo amplitude data were collected at kilo-Hertz carrier frequencies from the underside of a growing ice sheet. Using a plane-wave reverberation model, the velocity of the acoustic wave, attenuation and normal incidence reflection coefficient of the ice were measured at 15, 17, 20, 25 and 190 kHz. Analysis showed that the urea ice had reflection coefficients of about 0.4 in the tens of kHz range, significantly higher than saline ice. Attenuation at those frequencies was about 0.3 dB/cm. At higher frequencies, the acoustic properties of the urea ice begin to approach those measured on saline ice. For the diffraction phase of the experiment, a slot was cut in in the ice and the transducers were moved laterally under the edge of the lead. The diffracted and reflected echo arrivals were resolved and the amplitude of the diffracted signal was measured. A good comparison was found between the diffracted arrival values and Helmholtz-Kirchoff theory.

Table of Contents

List of Figures

List of Tables

Appendices

1. Introduction:

Recent laboratory experiments on acoustic propagation through thin saline ice (Stanton et al., 1986; Jezek et al., 1989) have demonstrated that the acoustic properties of saline ice are strongly correlated with the ice texture and morphology. These experiments have shown that for frequencies above 100 kHz, coupling into the ice is very good (reflection coefficients are typically less than 0.1) and the attenuation through the ice is high (3 dB/cm). Based on statistical analysis of echo amplitude data, they conclude that these acoustic effects are associated with the dendritic ice-water interface of growing sea ice and the entrapment of brine up into the body of the ice sheet.

The sea ice cover of the polar oceans can develop complicated geometries. Scattering from the edges of open leads (channels of water) or from irregular blocks that comprise the keels of sea ice ridges are important factors in acoustic propagation. High frequency acoustic backscatter from flat sea ice has been studied since the 1960's by C.S. Clay and H. Medwin (1977 pp544), J.R. Brown et al. (1966,1967), G.R. Garrison et al. (1978), and R.E. Francois (1988) and others. Only recently, however, has theoretical and experimental work focused on backscatter from more complex topographical features such as ice keels. A sophisticated model of under-ice acoustic backscatter from the Arctic ice sheet has been developed by G.C. Bishop (1989), and other studies by Posey et al. (1985) and Chin Bing (1985, 1987) have reported under-ice propagation and scattering.

The primary objective of this experiment was to describe high frequency acoustic backscatter from simulated arctic sea ice as a function of the physical properties of the ice. Diffraction experiments were performed on the edge of a large hole cut in the ice sheet. The edges of open leads are acoustically interesting because saline ice both supports shear waves and is highly absorptive. However, to understand the diffraction mechanism it was essential to characterize the bulk acoustic properties of the ice.

The experiment was carried out under controlled laboratory conditions in the indoor facilities at the U.S. Army Cold Regions Research and Engineering Laboratory, Hanover, New Hampshire. Urea ice is widely used as a modelling material for saline ice in laboratory tests because it is non-corrosive and has similar mechanical properties. In addition, the acoustic properties of ice are believed to be dependent on morphology, and independent of ice chemistry. We used urea ice as a substitute for saline ice in our experiment since they are considered morphologically very similar.

The experiment was divided into two parts:

a) The growth phase: Reverberation experiments were performed on the growing ice sheet. Normal incidence sonar echo amplitude data were collected at frequencies of 15kHz, 17 kHz, 20 kHz, 25 kHz and 190 kHz. Measurements were taken every 0.5 cm of growth in thickness. The echo amplitudes were tabulated

as a function of ice thickness and then fitted to a plane-wave reverberation model. The attenuation, reflection coefficient and phase velocity of the acoustic wave in the ice were then determined.

b) The diffraction phase: Echo amplitudes were measured as the transducers were moved along a horizontal plane beneath the ice edge. The various echoes from the ice surface, water surface, and from the ice edge were observed. The received waveforms were then digitized and the diffracted arrival isolated from the other signals. The amplitude of the diffracted arrival was recorded and found to be in agreement with values predicted using Helmholtz-Kirchoff theory.

2. Background:

2.1 Ice Texture and Morphology:

In recent years, urea ice has been widely used for modelling sea ice in test tanks in North America and Europe (Gow, 1984). When urea-doped water freezes, the build-up of urea at the ice-water interface eventually becomes too large to sustain a planar geometry. The interface then develops a cellular, or dendritic, morphology. After a stable dendritic interface forms, further freezing leads to the growth of dendrite tips which protrude down into the urea solution. Simultaneously, urea enriched liquid becomes entrapped in the grooves between the dendrites. This mechanical entrapment of urea is mostly confined to the grooves between the dendrites. The dendrites themselves are elongated parallel to the crystallographic basal plane, that is, normal to the c-axis. (See Figure 2.1) The c-axis is the principal hexagonal axis of the ice crystal; it is widely used as the reference axis for describing crystal structure and related physical and optical properties of the ice (Gow, 1984). The dendrites themselves contain negligible amounts of urea. As the ice grows, we see the formation of long columnar crystals, with each crystal composed of several plate-like dendrites. The resulting crystal substructure of ice plates and urea lamellae is in every way analogous to the ice plate and brine pocket substructure of the saline ice.
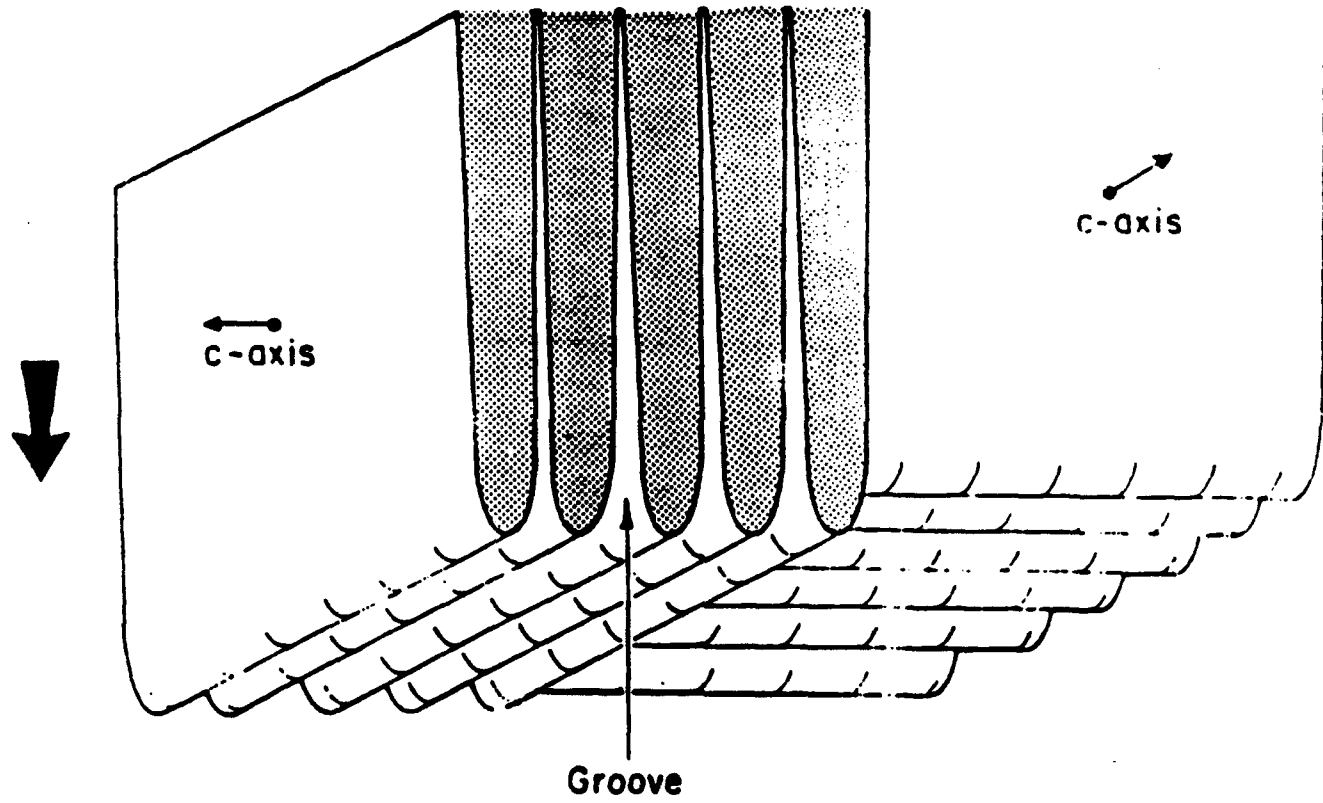
Figure 2.1: Schematic of interface geometry of two adjacent crystals of sea ice, showing vertical dendrite and groove structure and horizontal c-axes. Brine entrapment is confined to the grooves. The larger arrow on the left indicates the downward direction of growth.

The two ice types appear to be very similar morphologically (See Figure 2.2). For both ice types we notice multi-plate composition of individual crystals, liquid inclusions along the boundaries between the plates and the cellular structure of the individual plates. (Gow, 1984)

Seeded urea-ice sheets characteristically possess a multi-layered structure that is best observed in both vertical and horizontal thin sections (See Figure 2.2). A thin section is a sheet of ice less than 1 mm thick, mounted on a glass slide. The top layer of the ice sheet is called the seed layer (designated S), and consists of seed crystals generally less than 1mm in diameter and up to 3 cells thick. Underneath the seed layer are one or more layers of columnar crystals in which the c-axes are either vertical or horizontal. Layers of mixed orientation are not uncommon, although individual layers tend to be dominated by crystals of one orientation or the other. The columnar crystals in this layer known as the incubation layer and designated ic, exhibit crystal growth controlled by planar interface geometry. Textures and orientations encountered in the ic layer are those typically observed in freshwater ice. Individual crystals in the ic layer contain very few liquid or gasesous inclusions; the resultant structure is optically transparent, in contrast to the milky semi-opaque appearance of the underlying ice (Gow, 1984). By quickly reducing the temperature to 10°F at the time of seeding the urea ice sheet, we can confine the incubation layer to thicknesses ranging from 0.5 to 1 cm.

Figure 2.2 : **Comparative Morpholgy**

1mm

Saline Ice Sample   **Urea Ice Sample**

The incubation layer is underlain by the dendritic columnar layer, designated dc, which is composed of large, columnar crystals of dendritic origin. This layer forms the bulk of the thickness of the ice sheet. It consists mainly of crystals with horizontal c-axes since any crystals with c-axis orientations other than horizontal are usually eliminated by the process known as geometric selection. This process is well documented for sea ice (Perey and Pounder, 1958; Weeks and Lee, 1958).

The tips of the dendrites, which protrude down into the solution, form the final layer known as the dendritic interface. As growth occurs, substantial am unts of urea are systematically incorporated as layers of inclusions between the ice plates in individual crystals. It is assumed that this interface plays a significant role in the transmission and absorption of acoustic energy into the ice sheet. The ragged, feathery appearance of crystals from the bottom of the ice sheet is evident in the photomicrograph. (See Figure 2.3) Rigorous quantitative measurements to determine the exact length of these tips have not been made, but a qualitative estimation shows that in saline ice these dendritic tips are elongated and pointed while the dendritic tips of urea ice appear shorter and sturdier (See Figures 2.3, 2.4).

Figure 2.3: Photograph of basal thick section of urea ice sheet grown in October, 1989 showing structure of dendrites and interdendritic grooves. Amplification is X 7.

Figure 2.4: Photograph of basal thick section of saline ice sheet grown in 1985 showing structure of dendrites and interdendritic grooves. Amplification is X 7. The thin white lines are the interdendritic grooves while the darker sections show the dendrites of pure ice.

2.2 Acoustic Theory:

2.2.1 Transmission of Power-

Assume that the source is a small sphere. It expands and contracts uniformly and the signal travels outward radially. At normal incidence, in the far field ($kR \gg 1$) of the circular piston transducers of the type we were using, the signal might be assumed to be only a function of the distance R.

Following Clay and Medwin (p79-82), the wave equation for radially propagating waves in a spherical co-ordinates system is

$$\frac{1}{R^2}\frac{\partial}{\partial R}\left(R^2\frac{\partial \, p(R,t)}{\partial R}\right) = \frac{1}{c^2}\frac{\partial^2}{\partial t^2} \, p(R,t) \qquad (1)$$

where p(R,t) is the travelling pressure signal. Guessing the answer, we write

$$p(R,t) = (b/R) \, g(R,t) \qquad (2)$$

where b is a constant.

Substituting g(R,t) into (1) gives

$$\frac{\partial^2}{\partial R^2} g(R,t) = \frac{1}{c^2} \frac{\partial}{\partial t^2}^2 g(R,t) \qquad (3)$$

which has the same form as the one dimensional plane wave equation. Its solutions are $g(R,t) = g(t-R/c)$ and $g(t+R/c)$.

We will choose the outgoing signal $p(R,t) = (b_c/R) g(t- R/c)$, in complex form with time dependence $\exp(i\omega t)$ and write

$$p(R,t) = (b_c/R) \exp(i\omega(t- R/c))$$

Now we can evaluate b_c by assuming that the rms source pressure is P_0 at R_0, therefore $b_c = P_0 R_0$.

Alternatively, the real expression can be used

$$p(R,t) = (b_r/R) \cos(\omega(t- R/c))$$

The mean square value of the cosine function is 0.5, the source is P_0 at R_0, therefore $b_r = \sqrt{2} P_0 R_0$

Now we can write the expression for $p(R,t)$ as

$$p(R,t) = (P_0 R_0/R) \exp(i\omega(t- R/c))$$
$$p(R,t) = (\sqrt{2} P_0 R_0/R) \cos(\omega(t- R/c)) \qquad (4)$$

For a relation between the acoustic pressure and the particle velocity, we

may represent their relation in radial components

$$\frac{\partial p(R,t)}{\partial R} = -\rho_A \frac{\partial u(R,t)}{\partial t} \tag{5}$$

where $u(R,t)$ is the radial component of the particle velocity. Substituting (4) into (5) and using $\omega = kc$ yields

$$\frac{ikb}{R}\exp\{i(\omega t - kR)\}\ (1+\frac{1}{ikR}) = \rho_A \frac{\partial u(R,t)}{\partial t} \tag{6}$$

Since u must have time dependence $\exp(i\omega t)$ we use $\frac{\partial u}{\partial t} = i\omega u(R,t)$
Then (6) becomes

$$p(R,t)\ (1+\frac{1}{ikR}) = (\rho_A c)\ u(R,t) \tag{7}$$

For large kR (i.e. many wavelengths from the source), u is in phase with p and the relation is the same for plane waves

$$p(R,t) = (\rho_A c)\ u(R,t) \qquad\qquad kR \gg 1$$

The source transmits the power into the water. We define power as force times the velocity in the same direction. The instantaneous intensity, the power that passes through a unit area, is $p(R,t)u(R,t)$ when both quantities are real. Alternatively we use the real part of $p(R,t)u^*(R,t)$ when the quantities

are complex. For the sound pressure P_0 at R_0, the complex pressure and particle velocity are

$$p(R,t) = (P_0 R_0 / R) \exp(i\omega(t - R/c))$$

$$u(R,t) = \frac{P_0 R_0}{R \rho_A c} (1 + \frac{1}{ikR}) \exp[i(\omega t - kR)] \qquad (8)$$

The average intensity $<I>$, or the average power passing through a unit area, at distance R is

$$<I> = \mathrm{Re} \frac{1}{T} \int_0^T p(R,t) u^*(R,t)$$

Substitution of (8) followed by integration yields

$$<I> = P_0^2 \frac{R_0^2}{R^2 \rho_A c} \qquad (9)$$

Since the beam pattern geometry in the near field of the transducers may confuse the measurements, we take our calibration readings in the far field which is defined as

$$R_c \geq \pi a^2 / \lambda$$

by the American National Standards Institute (Clay and Medwin, p. 155) where a is the radius of the transducer and λ is the wavelength of the

transmitting wave. At 20 kHz, the wavelength of the acoustic wave in water is 0.07m and the radius a is 0.03m. Thus, the far field for our circular piston transducer was approximately 4 cm. The 1/R calibrations were made with the surface of the water about 60-80 cm away from the transducers. Similarly, beam pattern measurements were made in the far field with the target approximately 50-60 cm from the transducers. Assuming that the sound velocity in water is 1400 m/s, the value of k at 20 kHz is 89.75 m^{-1}. Since the range, R, between the transmitter and receiver is about 1m, we satisfy the condition that the above calculations be made where kR » 1.

The total power from the source Π is the integral of <I> that passes through the surface of the sphere of radius R

$$\Pi = \int_s <I> dS = \int_{4\pi} <I> R^2 d\Omega \qquad (10)$$

where $d\Omega = dS/R^2$ is the element of the solid angle.
Since I and R are constant over the spherical suface

$$\Pi = <I> R^2 \int_s d\Omega$$

$$\Pi = 4\pi P_0^2 \frac{R_0^2}{\rho_A c} \qquad (11)$$

This is the power radiated through the spherical surface at any radius, provided there is no loss of energy in the medium.

The rms pressure at the reference radius R_0 is

$$P_0 = \left(\frac{\Pi \rho_A c}{4 \pi R_0^2}\right)^{\frac{1}{2}} \tag{12}$$

In mks units, pressure is in newtons per square meter (N/m^2) = pascals (Pa), power in watts, distance in meters, and ρ_A in kilograms per cubic meter. Generally, 1 m serves as the reference R_0 because it is convenient in computation.

The rms pressure P at a distance R is inversely proportional to the the distance R .

$$P = \frac{P_0 R_0}{R} = \left(\frac{\Pi \rho_A c}{4 \pi R^2}\right)^{\frac{1}{2}} \tag{13}$$

(Clay and Medwin, p. 82)

2.2.2 The Sonar equation:

All the characteristics of the sonar system, (the sound transmission, the scattering characteristics of objects) are combined in the sonar equation. (Clay and Medwin, p.103) After all the quantities have been made dimensionless using reference distances and reference sound pressure levels, the sonar equation is usually expressed in decibels. Thus, the the sonar equation for transmission to a distant point (i.e. in the far field) is

$$SPL = SL - TL$$

where $SPL = 20 \log(P/P_r)$ dB re P_r

and $SL = 20 \log(P_0/P_r)$ dB re P_r

and $TL = 20 \log(R/R_0) + aR$

where P_r is the reference pressure ($1N/m^2$), R_0 is the reference distance (1m), a is the attenuation coefficient. SL refers to the source level, TL to transmission loss, and SPL to sound pressure level at the field position.

However when the ray paths reflect off another surface, the amplitude of the reflected signal is the amplitude of the incident signal multiplied by the reflection coefficient. We assume that the local interface is planar with respect to the wavelength of the incident wave. We describe this reflection process in the sonar equation by defining the bottom loss as

$$BL = -20 \log R_{12}$$

The net SPL is

$$SPL = SL - TL - BL$$

The bottom loss may conversely be used to compute the reflection coefficient of the reflecting surface.

We used a system of relative calibration to compute the reflection coefficient of the ice. In order to reference the reflection coefficients of the ice with a known quantity, we assume that the magnitude of the reflection coefficient off the open water is 1. Thus the bottom loss from open water is 0. Now,

$$SPL_{ice} = SL_{to\ ice} - TL_{to\ ice} - BL_{ice} \tag{1}$$

$$SPL_{water} = SL_{to\ water} - TL_{to\ water} - BL_{water} \tag{2}$$

For similar distances,

$$SL_{to\ ice} = SL_{to\ water}$$

and $\quad TL_{to\ ice} = TL_{to\ water}$

Therefore, subtracting (1) from (2) we get

$$SPL_{water} - SPL_{ice} = BL_{ice}$$

$$20 \log (P_{water}/P_r) - 20 \log (P_{ice}/P_r) = -20 \log R_{13}$$

$$P_{ice}/P_{water} = R_{13}$$

This method defines our method of relative calibration. By reading the amplitude of the SPL off the ice, and comparing it to the amplitude of the SPL off open water at a comparable distance, we can derive the total reflection coefficient, R_{13}, for the ice.

2.2.3 The Plane Wave Reverberation Model:

The reflection coefficients derived for the various frequencies as a function of ice thickness can be explained using a well-known theory for describing plane wave reverberation by a slab (e.g. Clay and Medwin, p. 64). For a loss-less slab, the normal incidence reflection coefficient is given by

$$R_{12} = \frac{\rho_2 c_2 - \rho_1 c_1}{\rho_2 c_2 + \rho_1 c_1}$$

where ρ is the density of the medium and c is the velocity of the acoustic wave in the medium. In order to introduce absorption loss, we let the sound speed (or alternatively the wave number) in the slab medium be complex i.e. $c_2 = c_2' + i c_2''$ where c_2' and c_2'' are real.

Now consider an acoustic pressure wave incident normally from below on a sheet of ice. The total down-travelling signal is the sum of the partial transmissions and reflections. Each path within the layer has a phase delay of 2Kh where K is the wave number and is defined as

$$K = k + ia$$
$$k = \omega/c_2'$$
$$a = \omega c_2''/c_2'$$

Here k is the real component of the wave number and a is the attenuation in the medium in nepers/m. The above approximations are valid only when $|c_2''|$ is much less than c_2'. By letting the incident signal have unit amplitude, we can conclude that the total reflection is

$$R_{13} = R_{12} + T_{12} T_{21} R_{23} e^{-2iKh} + T_{12} T_{21} R_{23}^2 R_{21} e^{-4iKh} + \ldots\ldots$$

After R_{12} the terms in the above equation have the form of a geometric series

$$S = \sum r^n = (1-r)^{-1} \qquad \text{for } r < 1$$

$$R_{13} = R_{12} + T_{12} T_{21} R_{23} e^{-2iKh} \sum [R_{23} R_{21} e^{-2iKh}]^n$$

Now assuming that

$$R_{12} = -R_{21}$$

and $$T_{12} T_{21} = 1 - R_{12}^2$$

we can express R_{13} as

$$R_{13} = \frac{R_{12} + R_{23} e^{-2iKh}}{(1 + R_{12} R_{23} e^{-2iKh})}$$

$$R_{13} = \frac{(R_{12} + R_{23} e^{-2i(k+ia)h})}{(1 + R_{12} R_{23} e^{-2i(k+ia)h})}$$

In our case, the slab of urea ice is bounded on the top by a layer of air and on the bottom by a layer of water. Assuming that there is total reflection from the top air-ice interface, R_{23}= -1. The magnitude of the reflection coefficient (R_{13}) appropriate for the transducers in the water is given by

$$|R_{13}|^2 = \frac{(R_{12}{}^2 + e^{-4ah} - R_{12}e^{-2ah}(2Cos(2kh)))}{(1+R_{12}{}^2e^{-4ah} - R_{12}e^{-2ah}(2Cos(2kh)))} \qquad (1)$$

where R_{12} is the reflection coefficient between the ice and water, a is the attenuation through the ice in nepers/m, h is the thickness of the ice in cm and k is the wave-number in ice. Complex wavenumbers are intended to model absorption loss. Because, the real part of the reflection coefficient is almost a factor of 10 larger than the imaginary part, the magnitude of the real part dominates the complex value. To simplify the computations, we assume the reflection coefficients to be real. This assumption is reasonable for the frequencies we are operating at and the attenuation measured (at 20 Khz, k=36 m^{-1} and a=3 m^{-1}). The model assumes uniform attenuation throughout the ice and no additional spreading loss owing to refraction. (Jezek et al. 1990)

2.2.3.1 Limitations of the model

The plane wave reverberation model described above assumes the medium to consists of a single layer with uniform bulk acoustic properties. However, previous experimental work (Jezek et al. 1988) done on saline ice has shown the properties of the ice to change as a function of depth. As the ice thickens the temperature distribution within the ice sheet varies. This causes changes in the salinity, porosity and permeability of the ice sheet. The structure and density of the brine-filled pockets show changes. Since the ice rejects brine as the sheet gets thicker, the brine trapped in the early stages of growth of the ice sheet gets pushed out towards the top of the ice sheet. Since brine is entrapped into the body at the base, the salinity of the sheet is highest near the top and bottom of a thick ice sheet. Langleben and Pounder (1970) in their study of Arctic sea ice conducted their experiments at 1 m depth in 2 m thick ice and the direction of propagation of the acoustic wave was perpendicular to the direction of ice growth. They reported attenuations much lower than those found by Jezek et al. (1989) for 18 cm thick saline ice. Jezek et al. also took normal incidence backscatter measurements and found that attenuation rates for 6 cm ice were measurably lower than those for 3 cm ice, substantiating the hypothesis that attenuation rates are diminished above the dendritic interface. Analysis of reverberation data in the 8-20kHz region suggests that ice less than a few centimeters thick is less lossy than thicker ice, an observation that may be associated with the transition to a dendritic

interface (Jezek et al 1990). It is recognised that the ice may be modeled more accurately using a multi-layered model. The different layers may be the relatively impervious incubation layer, the thin ice layer, thicker ice layer and the dendritic interface.

However, the ice sheet we worked with was young and relatively thin. Because we worked on young, thin ice we make the assumption that the ice sheet is a single, homogenous slab. This seems reasonable given the documented ice structure described in section 3.4 where we notice that the dendritic layer dominates the thickness of the ice. The urinity of this layer is estimated to be fairly constant at 6 ppt. It is also weakly supported by the fact that by using a single layered plane-wave reverberation model, we were able to obtain a reasonably good fit, within ± 10%, for the theoretical and experimental data curves. Finally, given that the ice sheet was grown only to 19 cm thickness, the experimental data at the lower frequencies could not *conclusively* confirm that the attenuation changed as the ice grew. The attenuation parameter changed the rate of decay of the reflection coefficient envelope. The amplitudes of the peaks and troughs would determine the slope of this envelope, and at the lower frequencies we saw only 2-3 peaks by 19 cm thickness. A check of the attenuation parameters, showed that lowering the attenuation parameter 10-15% provided a better fit for the thinner ice data. In addition the ice was morphologically relatively homogenous with no obvious discontinuities, such as bubble layers, that would neccessitate a multi-layered model.

3. Experimental Approach:

Our measurements took place in December 1989, at the Cold Regions Research and Engineering Laboratory's indoor cold pit in Hanover, New Hampshire. The pit was 3m wide by 3m long by 1.3m deep. The pit was filled with tap water raised to a urinity of 10 parts per thousand (ppt) by the addition of finely granulated urea. The ice sheet we examined was the second ice sheet grown for this experiment and was seeded by spraying a fine layer of water droplets evenly on the urea solution. The temperature in the room was maintained between 0° F and 10°F for the duration of the experiment with periodic adjustments made to control the rate of growth of the ice sheet (See Figures 3.1, 3.2). Consequently, the ice growth rate was maintained at 3.5 cm/day for the first 10 cm of growth and then decreased to 2-2.5 cm/day until the ice sheet was 19 cm thick.

3.1 Set up:

Both the growth and diffraction experiments were performed using the same electronic setup (See Figure 3.3a). Two piezoelectric ceramic transducers that resonated at 190kHz with narrow beamwidth (about 9 degrees) were mounted adjacently on a horizontal arm attached to a vertical shaft. The shaft was then mounted on a tripod and deployed below the ice. The tripod allowed the transducers to be rotated 360 degrees.
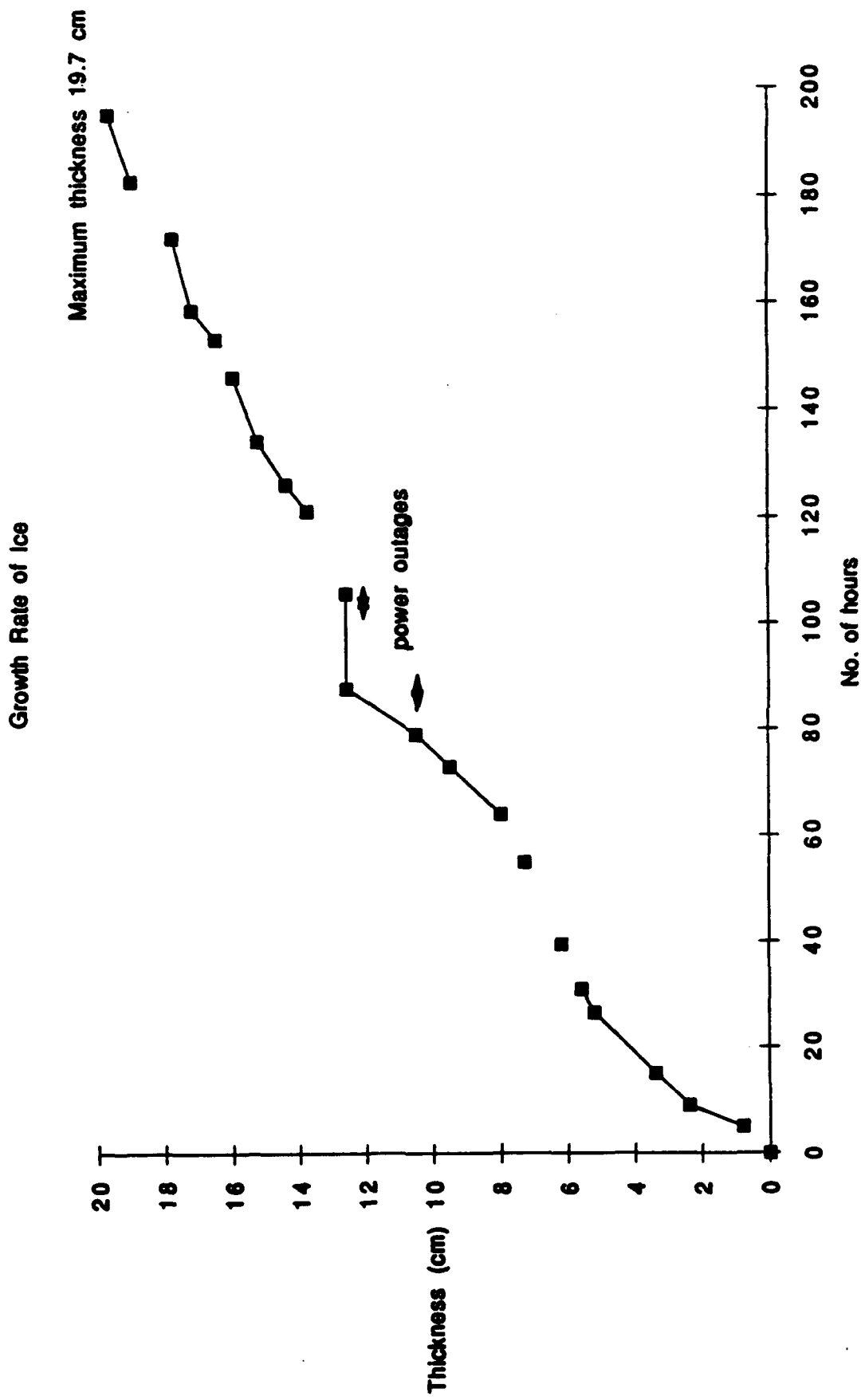
Figure 3.1: Shows thickness of ice as a function of time. Varying growth rates reflect changes in the air temperature caused by power outages.
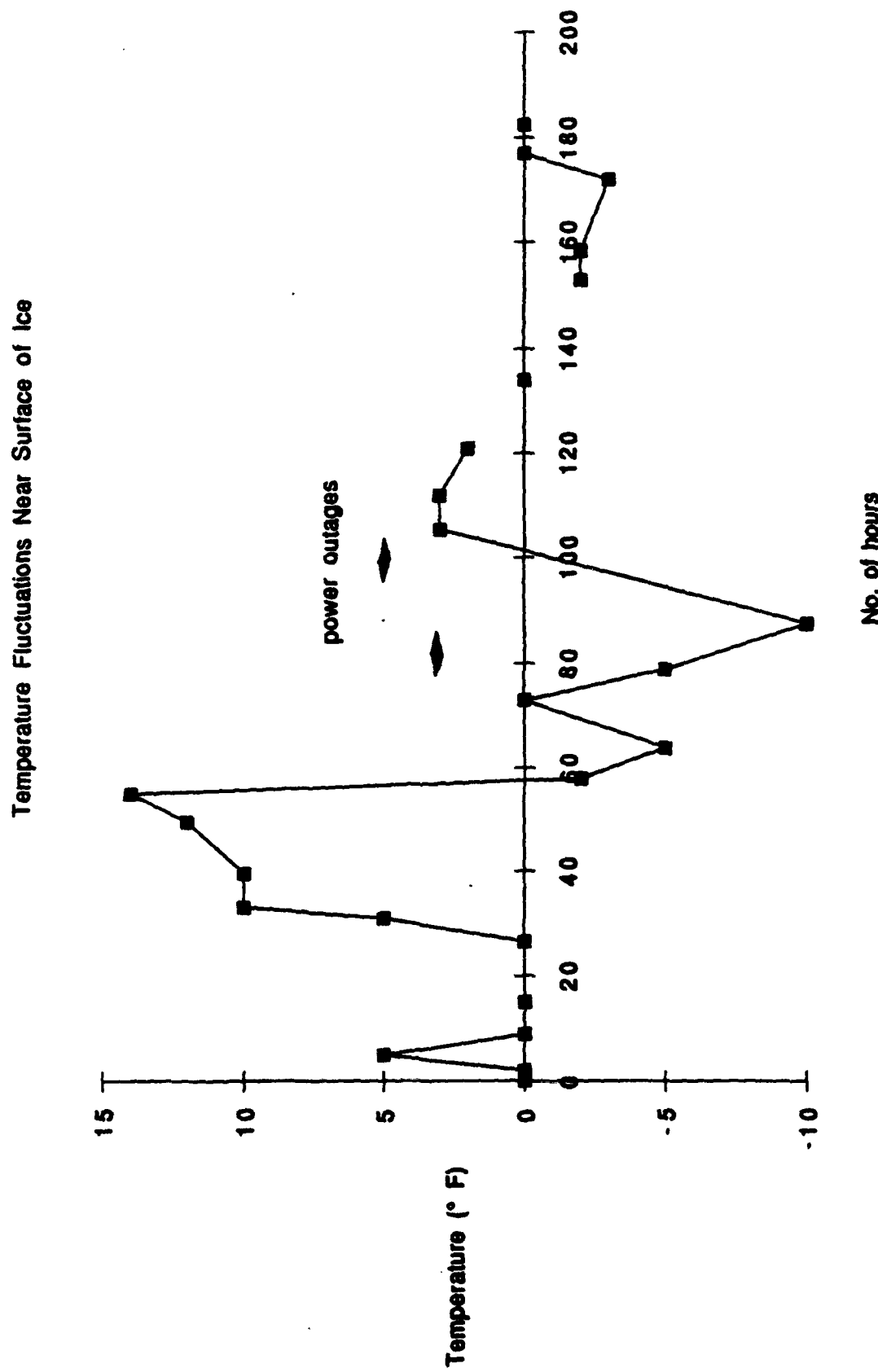
Figure 3.2: Shows temperature of ice as a function of time. The temperature was changed to control the growth rate. Changes in the temperature were also caused by power outages.

Experimental Set-up 15,17,20 and 25 kHz
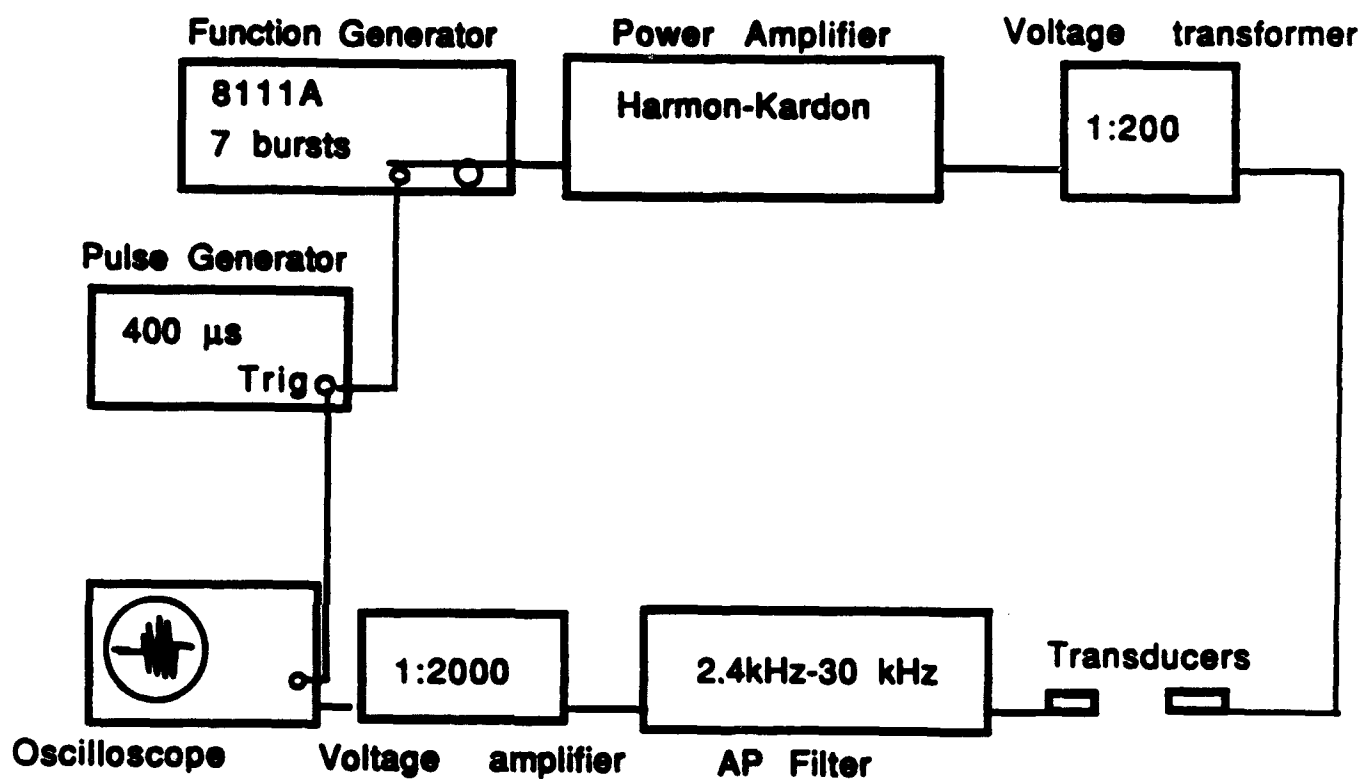
Figure 3.3: Electronics set-up for the growth and diffraction phases of the experiment at the lower frequencies.

Thus, patches of the under-surface of the ice could be independently insonified at normal incidence. A Hewlett Packard (HP) pulse generator 8011A produced trigger timing and gate duration (400 microseconds for all frequencies) for our pings and an HP pulse/function generator 8111A produced tone bursts (no. of wave-cycles) at the various resonance frequencies of our transducers. We used 7 cycles for the lower frequencies and 37 cycles for 190 kHz. These were the minimum number of cycles that allowed the signals to reach a steady-state peak value. The output of the function generator (1V at lower frequencies, 16.57 V at 190 kHz) was amplified through a Harmon-Kardon power amplifier that provided a gain of 30. The Harmon-Kardon fed a 1:200 voltage transformer that was connected to the transmitting transducer. The voltage across the transducer was measured to be approximately 500+ V. The receiving transducer was connected to a AP Circuit Corp Frequency filter with a pass band ranging from 3 kHz to 24 kHz for the lower frequencies and 3 kHz to 240 kHz for the higher frequencies. The output from the filter was passed through an operational amplifier cascade with a gain of 2000 (See Figure 3.4) before being read on a Tektronic digital oscilloscope. The amplifier consisted of a cascade of three 741C operational amplifiers. The first two stages had a gain of 10 and the final stage had a gain of 2. This provided a total amplification of 2000 while still maintaining a bandwidth of 70 kHz. A polaroid camera was used to photograph the observed waveform on the oscilloscope screen. The amplitudes and travel times of the reflected pulses were manually recorded.

Schematic of Op-Amp circuit
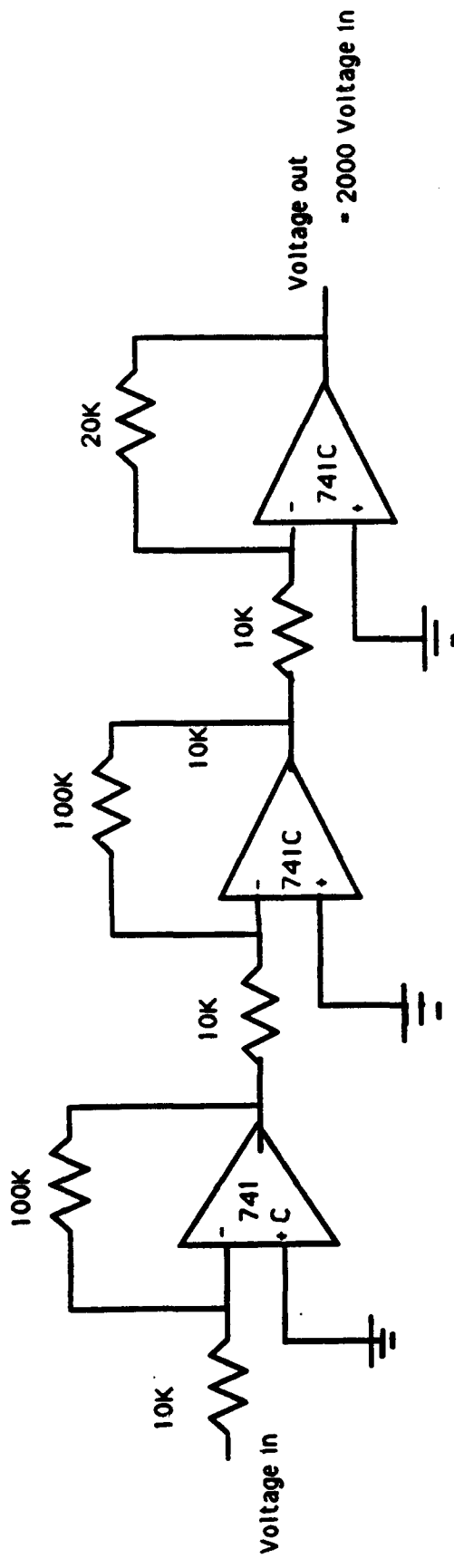
Operational Amplifiers are Analog Devices 741C

Figure 3.4: Schematic of the operational amplifier circuit. Op amps had a cumulative gain of 2000.

Since the transducers had been designed to resonate at 190 kHz, the setup at that frequency was modified by removing all the amplifier stages described above. The transducers were directly connected to the transmit and receive electronics (See Figure 3.5). The received signal still had a 20-25 dB signal to noise ratio without amplification.

Experimental Set-up 190 kHz

Function Generator

8111A
37 bursts

Pulse Generator

400 µs
Trig

Oscilloscope

2.4kHz-300kHz

Transducers

AP Filter
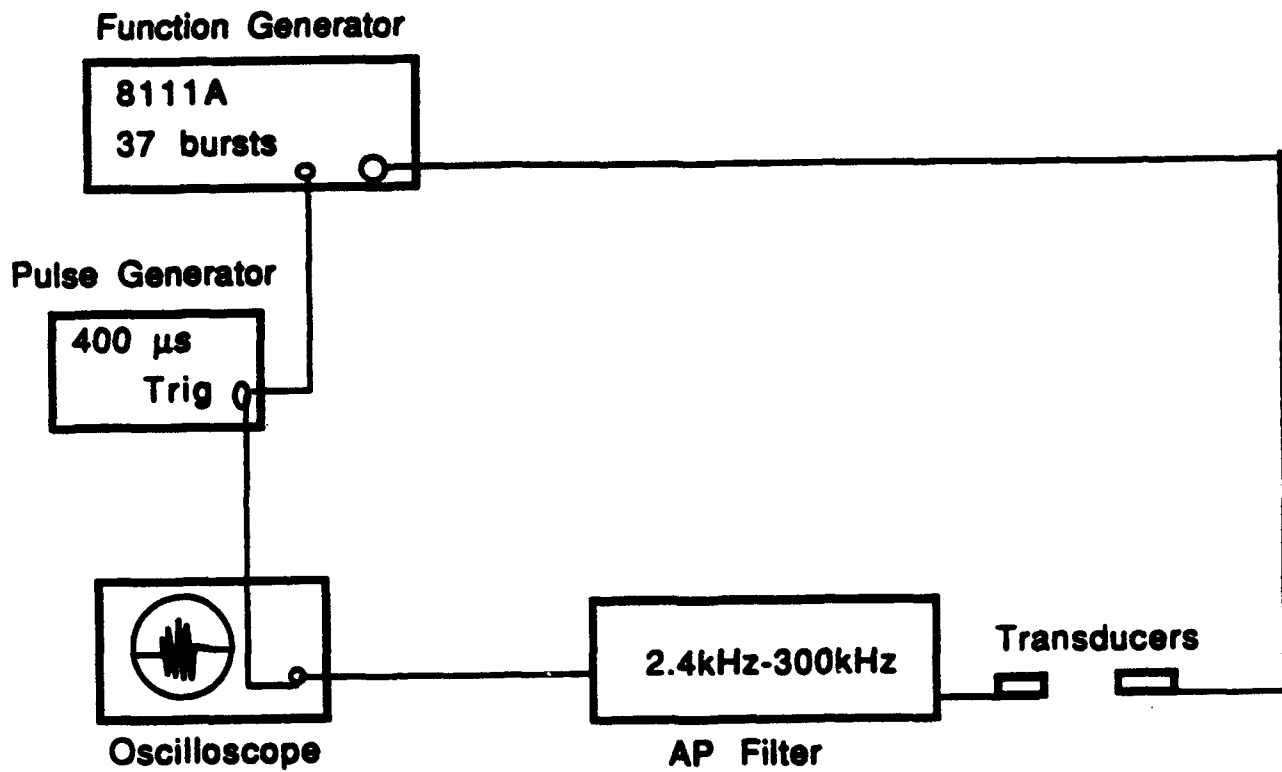
Figure 3.5: Electronics set-up for the growth phase of the experiment at 190kHz. The amplifier circuitry has been removed and the transducers are connected directly to the transmit/receive electronics.

3.2 Calibrations:

3.2.1 1/R calibrations:

1/R calibrations were performed at 15, 17, 20, 25 and 190 kHz in order to verify that the transducers exhibited the predicted range dependence in the far field. (See Figures 3.6a-3.6e) At the lower frequencies, a 7 cycle normal-incidence signal (37 cycles at 190 kHz) was reflected off open water. The peak amplitude and travel times for the reflected signals were measured for various distances, and the results plotted on a log-log graph to verify the 1/R dependence of amplitude vs distance. (See Table 1) The narrow beamwidth (about 9 degrees) of the transducers operated at 190 kHz affected the 1/R calibrations. Since the centres of the transmit and receive transducers had a space of about 7 cm between them, at close range a large part of their beam patterns would not overlap. This angular effect may have led to a diminshed dependence of received power on range (See Figure 3.6e). We find a standard deviation of 23% from a 1/R dependence at 190 kHz.

By carefully measuring the depth of the transducers below the water and then dividing by the observed travel time of the received signal, the speed of sound in water was computed to be 1400 m/s. The speed of sound in the ice was measured to be approximately 3800 m/s (±5%). A short pulse of 3 bursts at 190 kHz was transmitted from under the ice. The difference in travel times

Figure 3.6a: Graph showing 1/R range dependence of the signal amplitude reflected from open water at 15 kHz. Data points include measurements taken before and after experiment. Percentage error = 7%

15 kHz Pre/Post experiment1/R calibration
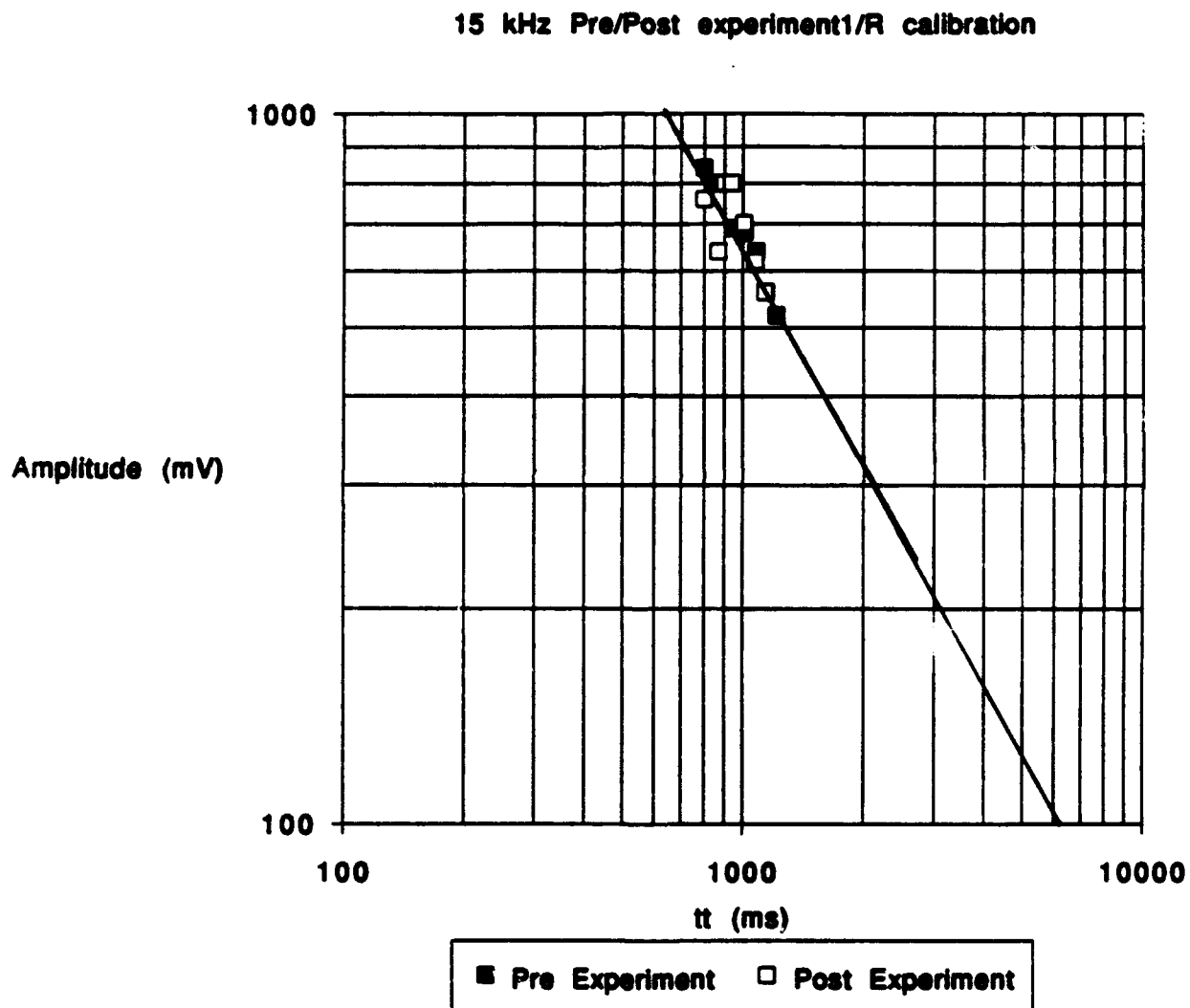
Figure 3.6b: Graph showing 1/R range dependence of the signal amplitude reflected from open water at 17 kHz. Data points include measurements taken before and after experiment. Percentage error = 7%
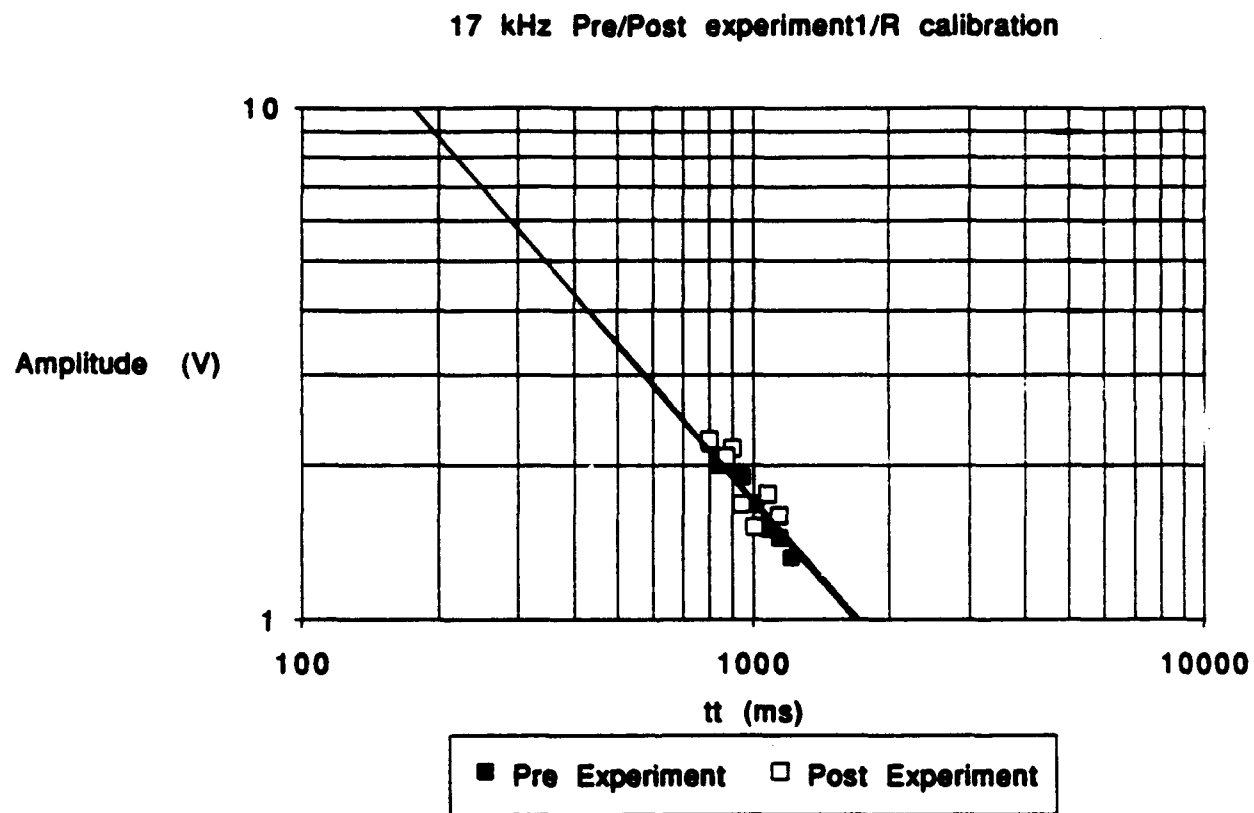
.:gure 3.6c: Graph showing 1/R range dependence of the signal amplitude reflected from open water at 20 kHz. Data points include measurements taken before and after experiment. Percentage error = 10%

20 kHz Pre/Post experiment1/R calibration
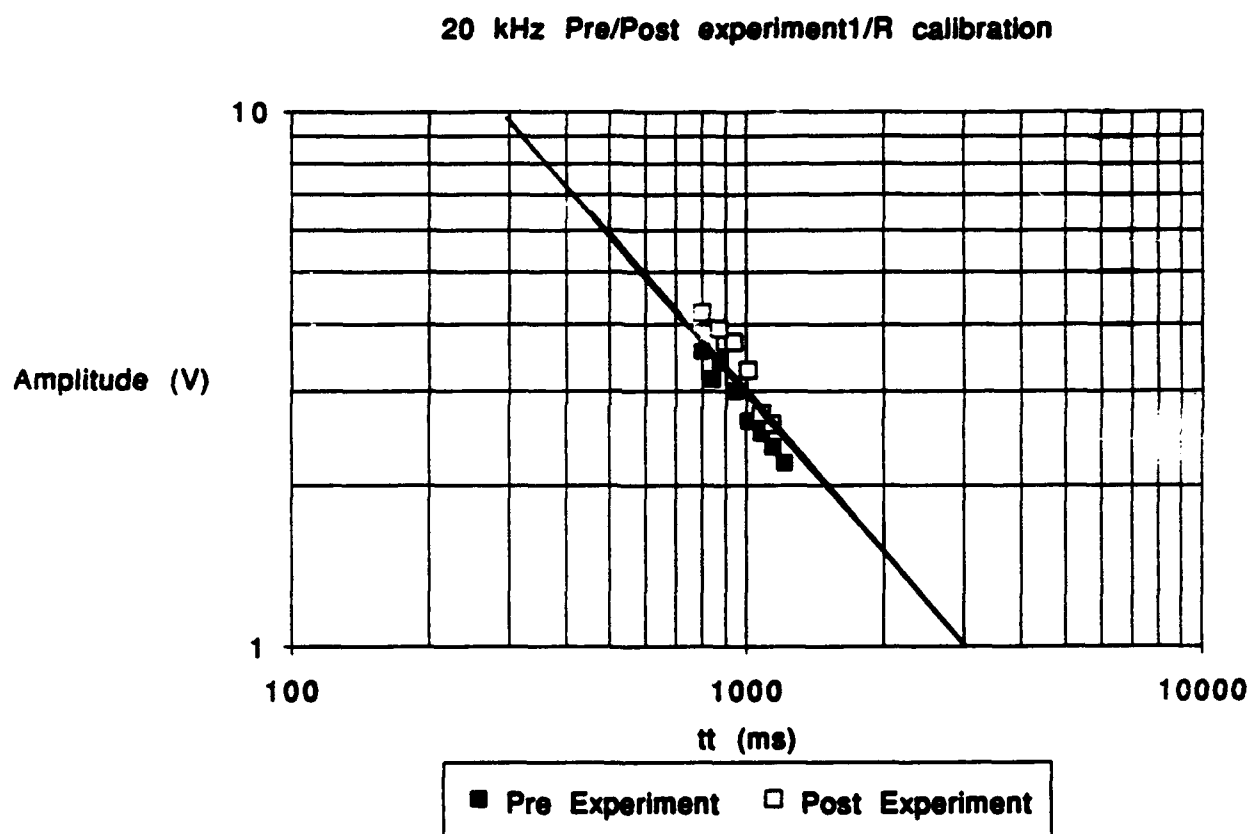
Figure 3.6d: Graph showing 1/R range dependence of the signal amplitude reflected from open water at 25 kHz. Data points include measurements taken before and after experiment. Percentage error = 11%

25 kHz Pre/Post experiment1/R calibration

Amplitude (V)

tt (ms)

■ Pre Experiment   □ Post Experiment
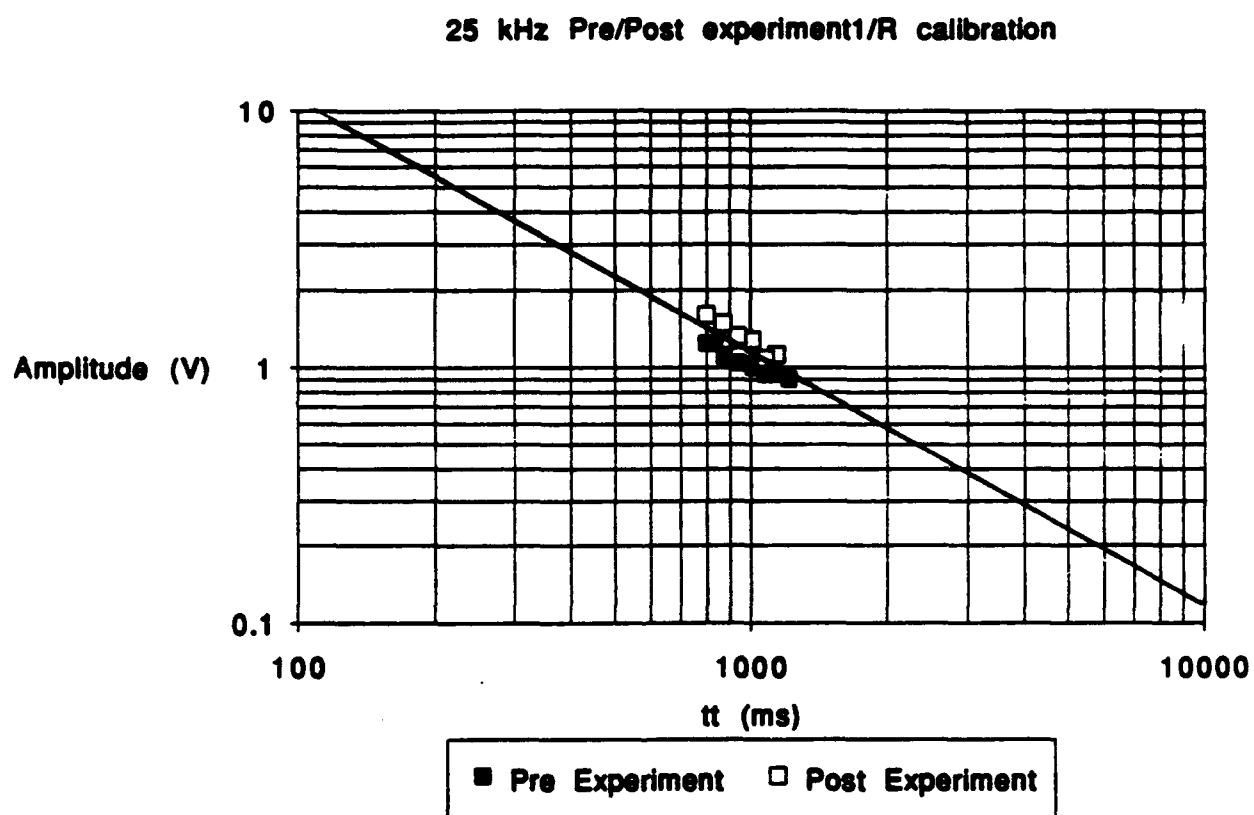
Figure 3.6e: Graph showing 1/R range dependence of the signal amplitude reflected from open water at 190 kHz before experiment. Percentage error = 23%

190 kHz pre experiment 1/R calibration
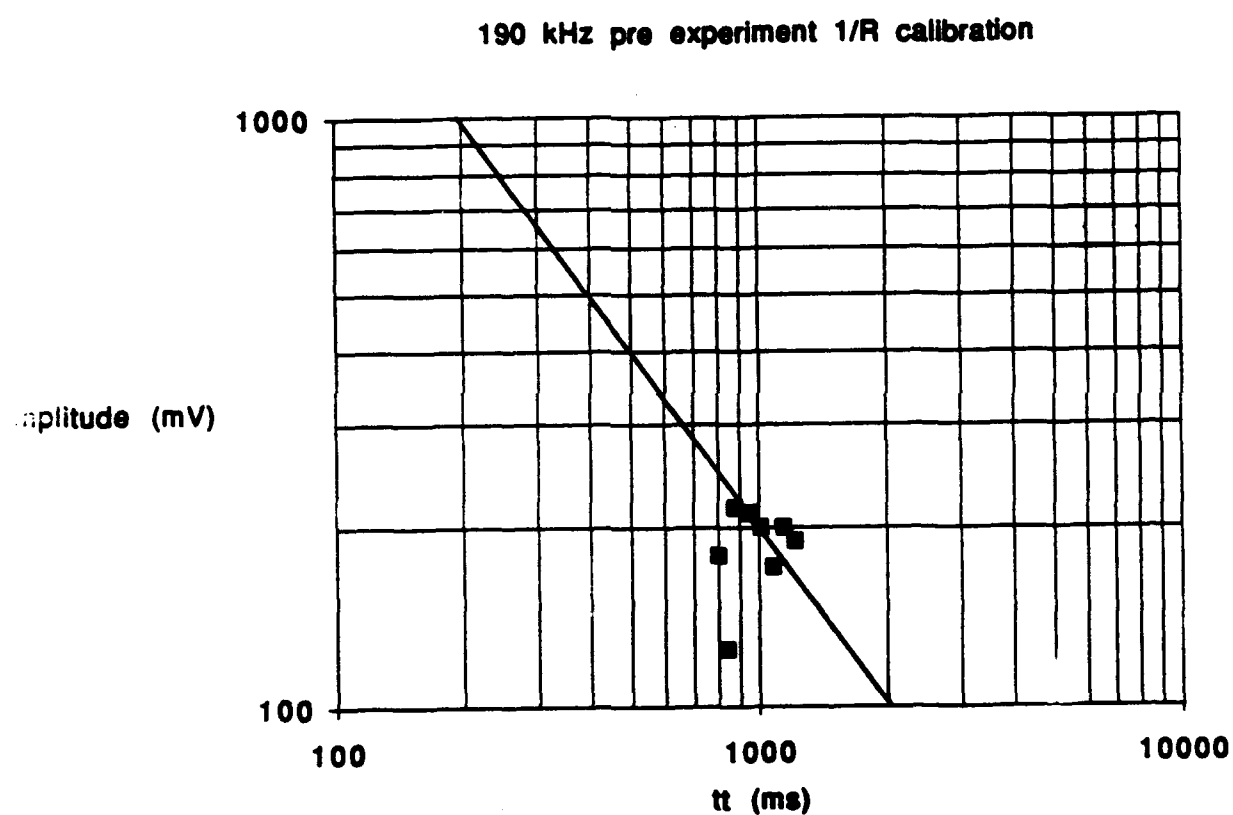
for the received pulses from the water-ice and ice-air interfaces was measured. The speed was computed by dividing the thickness by this difference. The change in acoustic velocity leads to refraction in the ice resulting in beam-spread losses of approximately 2 dB in 20 cm thick ice at 20 kHz (Jezek, verbal communi .tion). This loss, however, has been ignored in the plane-wave reverberation model.

After the experiment had been concluded, 1/R calibrations were repeated to verify the stability of the system throughout the course of the experiment (See Figure 3.6a-3.6d). Unfortunately, the transducers had to be removed from the water prior to the recalibration, and the subsequent re-soaping and re-immersion increased the signal level by -1% 15 kHz, 4% at 17 kHz, 18% at 20 kHz and 22% at 25 kHz.

Assuming a 1/R dependence of the amplitude, we calculated the product of amplitude and travel times for the different frequencies. A percentage error was computed by dividing the standard deviation by the mean value (See Table 3.1). The percentage errors were as follows:

Table 3.1

	15kHz	17kHz	20kHz	25kHz	190kHz
Pre calibration	4%	4%	4%	4%	23%
Post calibration	10%	9%	7%	5%	
Pre-Post	7%	7%	10%	11%	23%

3.3.2 Beam pattern calibration:

Beam Pattern measurements were made to determine the angular dependence of the reflected signal's amplitude. The transducers were submerged in the pool and a vacuumed bulb attatched to a thin rod was suspended approximately 50-55 cm directly above the transducers. The transmitting transducer was excited at 20 kHz. In order to minimize the pulsewidth of the reflected signal and still provide an acceptable signal level, two cycles were transmitted. This provided a pulsewidth of about 75-100 microseconds while generating a S/N ratio of about 15-20 dB. Two sets of measurements were taken. For the first set the bulb was moved parallel to the shaft in increments of 5 cm until the reflected signal was no higher than the noise level of about 40 mV (See Figures 3.7). For the second set the bulb was moved perpendicular to the shaft along the axis connecting the two transducers; again in increments of 5 cm until the signal was indiscernible from the noise (See Figures 3.8). The target was placed in the far field of the transducers because the beam pattern geometry is complicated close to the transducers. The results were plotted on a graph with gain against lateral distance. By knowing the vertical and lateral distances from the transducers to the target, we could calculate the angular dependence of the reflected power.
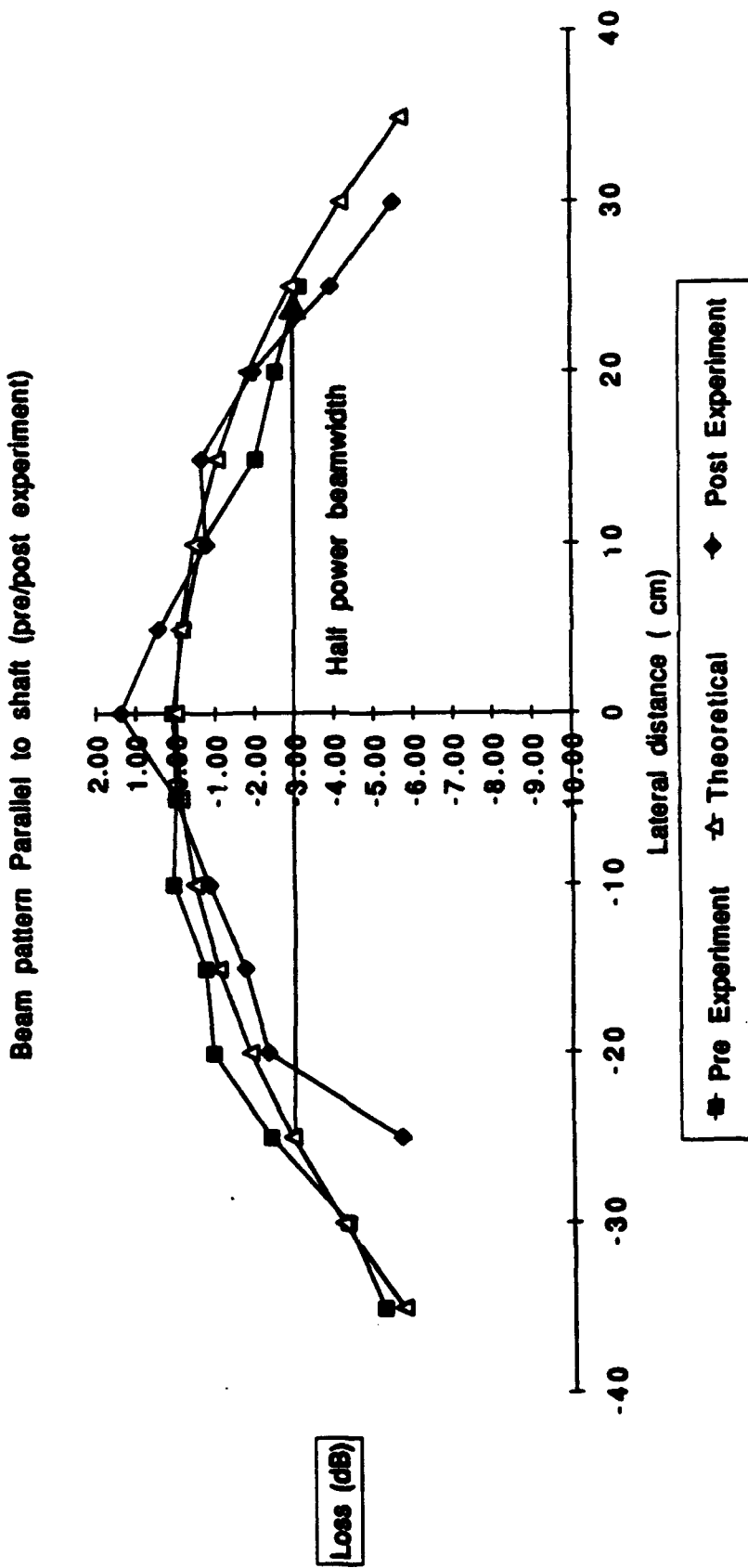
Figure 3.7: Beam pattern calibration showing target strength as a function of lateral distance parallel to the shaft away from the transducers. The 3dB loss level shows the half power beamwidth.
HP beamwidth = 47°
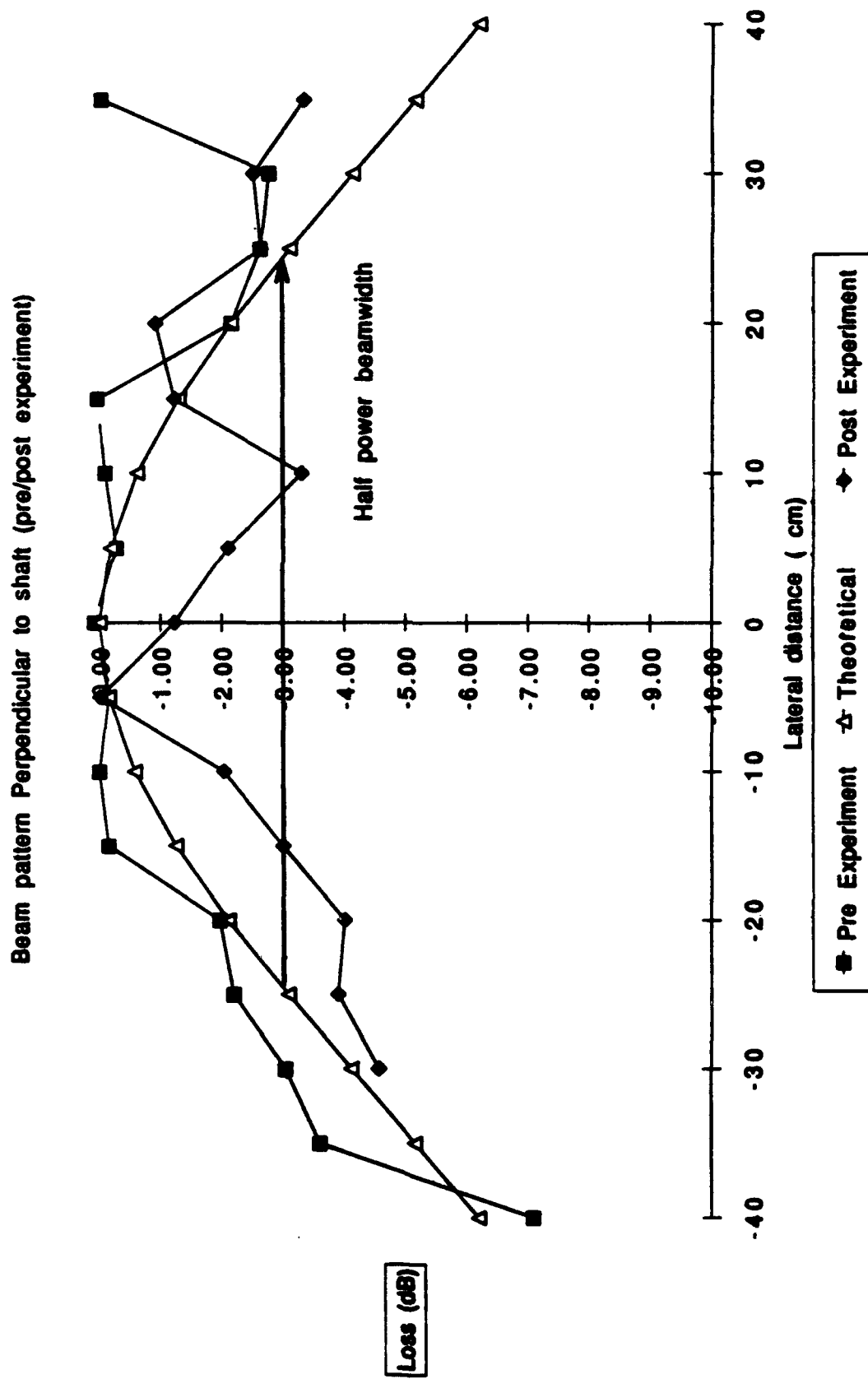
Figure 3.8: Beam pattern calibration showing target strength as a function of lateral distance parallel to the shaft away from the transducers. Calibration was performed after experiment. The 3dB loss shows the half power beamwidth.

3.3.2.1 Beam pattern theory:

For a directional transducer,

$$P = \frac{P_0 R_0 D}{R} \exp(i(\omega t - kR)) \tag{1}$$

where $D = D(\theta)$, the gaussian beam pattern.

Intensity away from the source, at distance R_T from the transmitter is

$$\Pi = \frac{P^2}{\rho_{AC}} = \frac{D^2 P_0^2 R_0^2}{R_T^2 \rho_{AC}} \tag{2}$$

Now, the power intercepted by the target of cross-sectional area, σ, is

$$\Pi = \frac{D^2 P_0^2 R_0^2}{R_T^2 \rho_{AC}} \sigma \tag{3}$$

If we assume spherical spreading of the power scattered from the target, then the scattered power intensity is

$$\Pi = \frac{D^2 P_0^2 R_0^2}{4 \pi R^2 R_T^2 \rho_{AC}} \sigma \tag{4}$$

and the power intercepted by the receiver, at distance R_R from the target,

where a=3 cm.

Now, we have two transducers that have their central axes 7cm apart. Consider the beamwidths to be Gaussian and of the form $e^{-d(\theta/\theta_0)^2}$ where θ_0 is the half-power beamwidth derived above for a single transducer. $\theta_o = 72°$

Now when $\theta = \theta_0/2$ i.e half-power angle, then

$$e^{-d(\theta/\theta_0)^2} = 0.5$$
$$e^{-d(\theta_0/2\theta_0)^2} = 0.5$$
$$e^{-d/4} = 0.5$$
$$d = 2.77$$

Assume that the transducers are placed 7 cm apart and the target is moved 52 cm above the axis connecting their centres. The angle θ_t is the angle made between the target and the normal to the transmitting tranducer, while angle θ_r is the angle made between the target and the normal to the receiving tranducer. Now the Gaussian beam pattern for both transducers is of the form

$$e^{-d(\theta_r/\theta_0)^2} e^{-d(\theta_t/\theta_0)^2}$$

which gives us the theoretical beam pattern.

The effective half-power beamwidth of the main lobe was the angle at which reflected power was half the peak power i.e. the 3dB loss level. This was calculated to be about 49° at 20 kHz (See Table 3.2). The results of the beam pattern tests are summarised below

Table 3.2

Pre experiment:	Measured θ	Theoretical θ
Parallel to shaft	50°	50°
Perpendicular to shaft	57°	52°
Post Experiment:		
Parallel to shaft	45°	50°
Perpendicular to shaft	45°	52°

The half-power beamwidth derived from the theoretical plots is approximately 50-52°. (See Appendix 2)

The lower measured beamwidth may be attributed to the fact that the bulb was not a perfectly spherical target and its reflectivity may vary as the function of its position above the transducers. Another source of error that might account for the skew in the beam pattern data might be the that the transducers were not perfectly horizontal in their mounts, thereby altering the beampattern.

3.4 Observations of Ice Morphology:

The horizontal and vertical thin section of the ice-sheet grown on December 13, 1989, show no large variations from the structure described above. The sections were prepared from samples that were removed periodically from the same general region on the ice sheet. Sections about 0.5 cm thick were mounted on glass slides, and shaved using a microtome to a thickness less than 1 mm. The crystal structure of the ice was highlighted by photographing the sections between crossed polarizers.

The vertical section shows features characteristic of urea ice as described in section 2.1. (See Figure 3.9). The seed layer is barely distinguishable at the top of the ice sheet, because water used to bond the thin section onto the slide melds the edges. The i_c layer is about 0.3-0.4 cm thick and the d_c layer dominates the structure of thicker ice. In the case of ice more than a few centimeters thick, we thereby assume the ice sheet to be a uniform single-layered half space. We note the long parallel lines of urea inclusions within individual crystals. There is a progressive increase in the cross-sectional diameter of the columnar crystals as the ice thickens. The c-axis orientation of the crystals are generally within the horizontal plane. The dendritic interface is not distinguishable in this section, since it is very fragile and disintegrates during the mounting process.

A comparison of the horizontal cross-sections shows how the dendrites progressively increase in size with increasing ice thickness. The photographs taken in plain transmitted light shows vividly the urea inclusions, air bubbles and dendrite boundaries. The photographs taken between crossed polarizers reveals the different crystals by virtue of their different c-axis orientation (See Figures 3.9-3.12). The 0.8 cm thick ice (Sample A) shows the beginning of the dendritic phase where the crystals are 2-3 plates thick. The brine inclusion process has just started and the pockets are not well defined. In the 3.4 cm thick ice (Sample C), the dendritic interface is well formed and individual crystals are well defined and 4-7 dendrites thick. In the 7.3 cm thick ice (Sample E), the dendritic interface has stablised and remains qualitatively unchanged for the rest of the growth phase. The brine inclusions between the dendritic plates are distinct. A fine line of inclusions between the plates is indicative of a fine horizontal cut through the thickness.

A study of the plate-width as a function of thickness revealed that periods of high growth rate are characterised by narrow plate-widths while periods of slow growth are characterised by wider plate-widths (See Table 3.3).

Table 3.3

Sample	Thickness(cm)	Platewidth (mm)	Growth rate (cm/day)
A	0.8	0	3.5
B	2.4	0.35	3.5
C	3.4	0.35	3.5
D	5.1	0.45	3
E	7.3	0.55	1
F	8.1	0.5	1
G	10.5	0.45	3
H	12.6	0.5	0
I	14.4	0.5	2
J	19.7	0.55	1

Initially, the growth rate was 3.5 cm/day and samples A,B, and C show plate-widths of 0.35 mm. As the growth rate fell to 2.5cm/day the platewidth increased to 0.5 mm. In the case of samples H and J, where very little growth had taken place, the platewidth was 0.55 mm. A check of the effect of platewidth on the reverberation data showed no observable co-relation between the normal-incidence reflection coefficient and plate-width.

Smaller bubbles observed in the sections may be air pockets entrapped as the ice grew while the larger blobs (indicated by arrows) are bubbles of air trapped between the glass plate and the ice during the sectioning process. In

the 19.7cm thick ice (Sample J) the crystals have 15-20 dendritic plates. The dendrites themselves are 0.55 mm wide. No significant air bubble layers were noticed and the c-axes orientation of the crystals in the dendritic layer were horizontal. The brine pockets, platelets and grains may all act as sites of stress concentration from passage of the acoustic pressure wave. Since the crystals are not perfectly vertical and do not stretch the entire thickness of the ice sheet, the acoustic wave may find varying paths as it travels through the ice sheet.

The photomicrograph of the thick section of the urea ice (See Figure 2.3) shows that the dendrites are 0.7mm thick and the crystals are much larger than the saline ice crystals. A quantitative measurement of the dimensions of saline and urea ice dendrites, grown under comparable conditions, is essential to conclusively prove that the reflection coefficients are affected by these structures.

C 3.4 cm
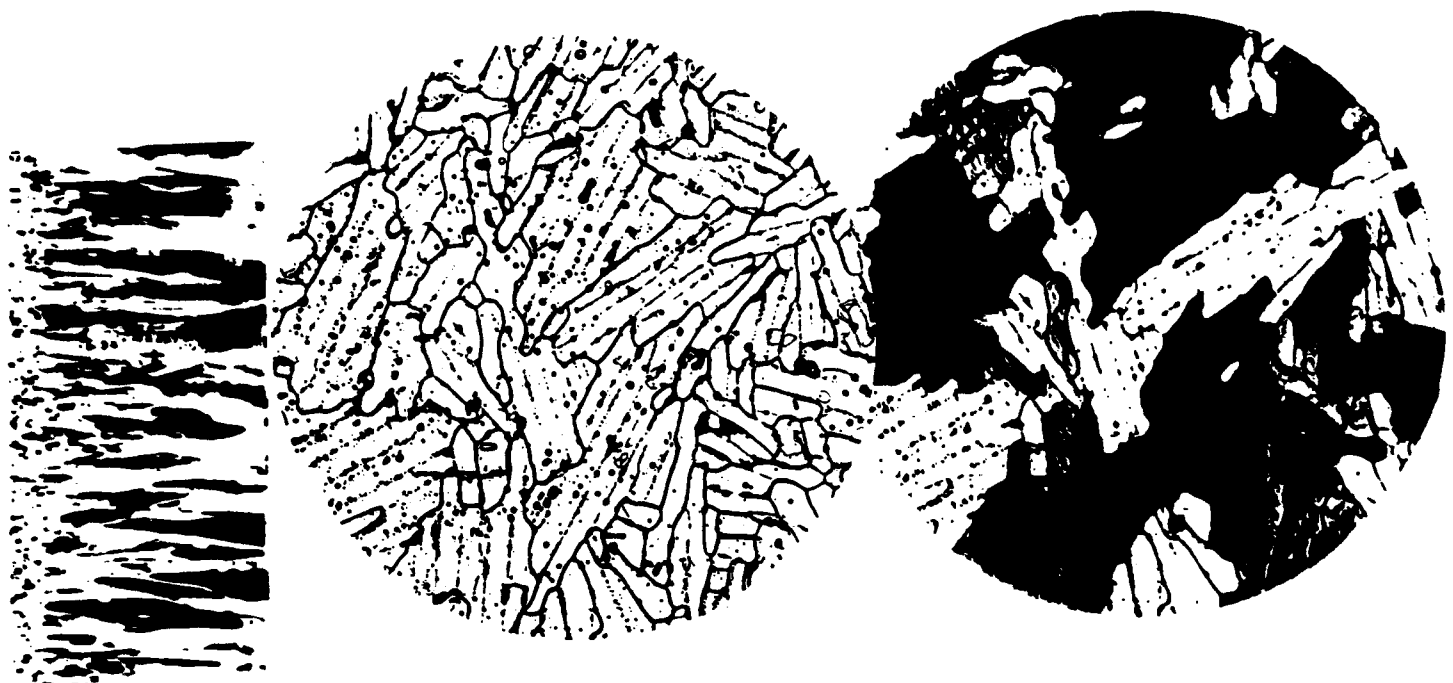
B 2.4 cm
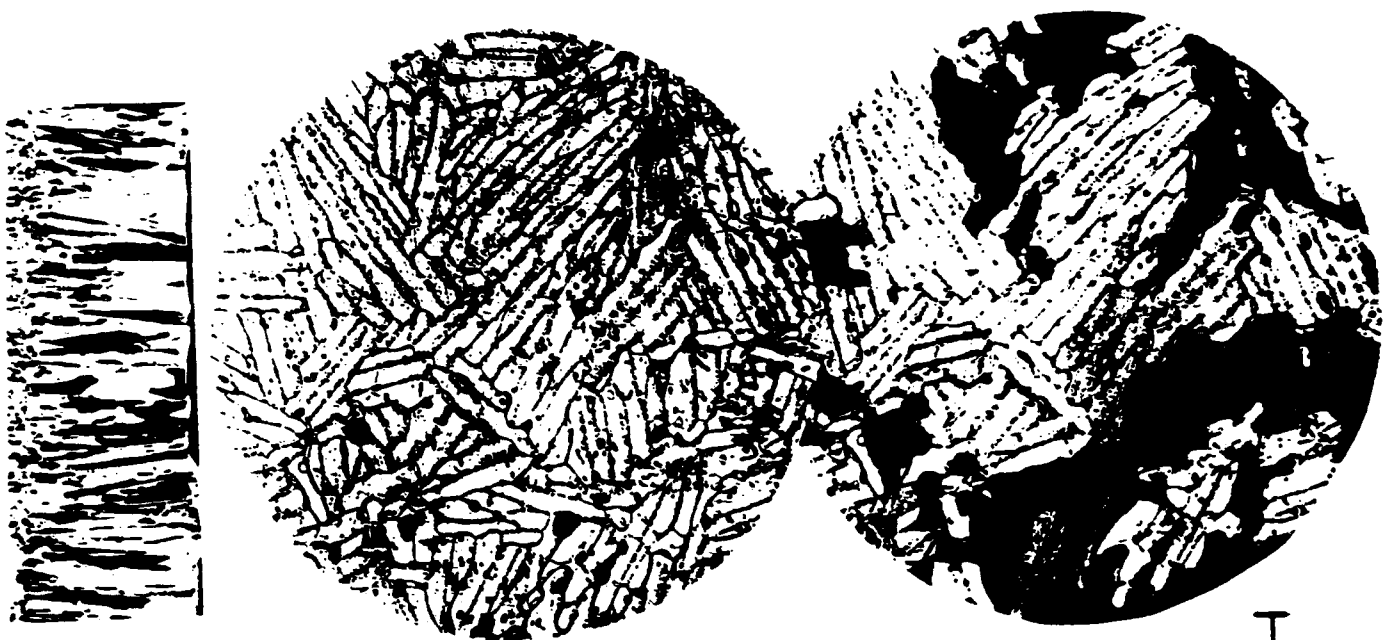
A 0.8 cm

5 mm
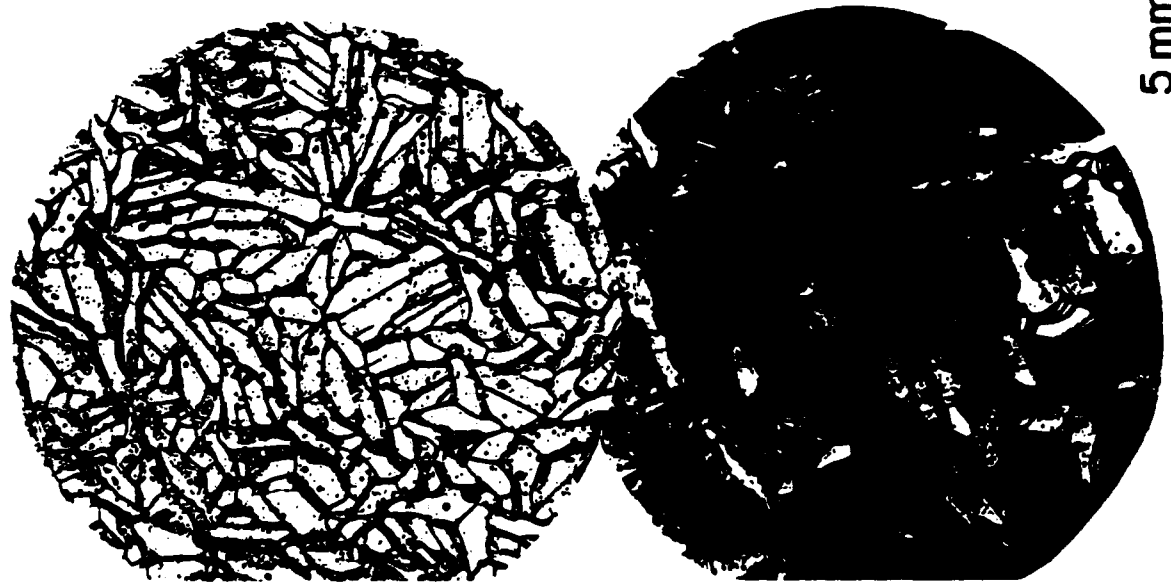
Figure 3.11: Samples A-C of urea ice sheet. Sample A of ice sheet 0.8 cm thick. Sample B of ice sheet 2.4 cm thick. Sample C of ice sheet 3.4 cm
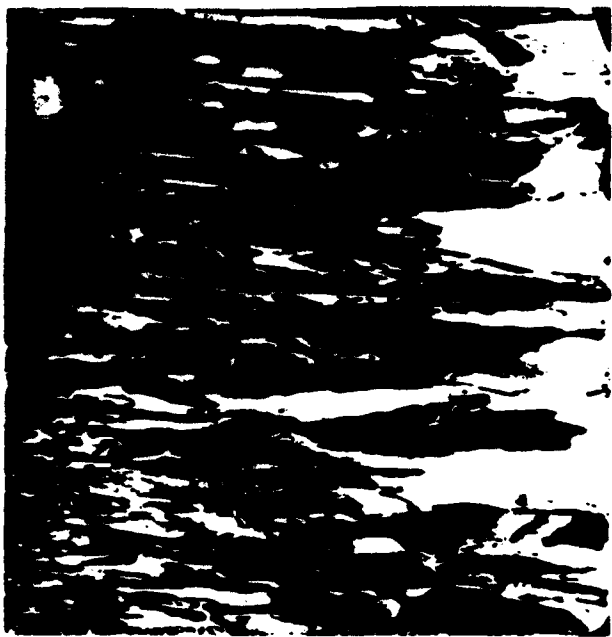
D 5.1 cm

E 7.3 cm

F 8.0 cm

5 mm
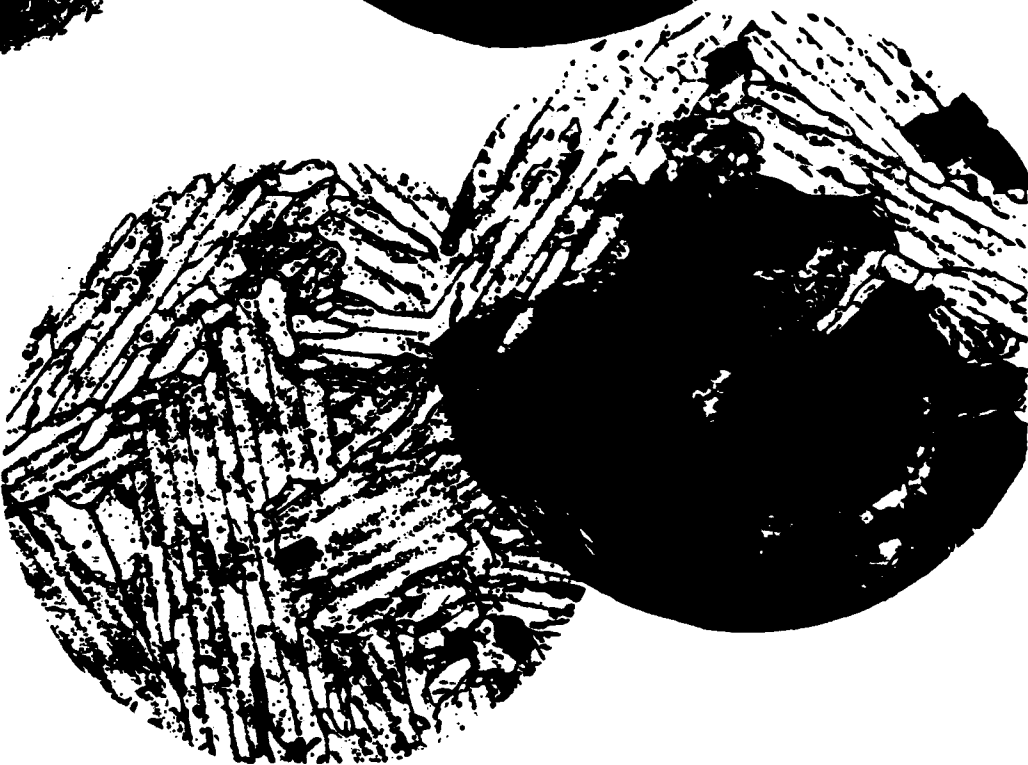
Figure 3.10: Samples D-F of urea ice sheet. Sample D of ice sheet 5.1 cm thick
Sample E of ice sheet 7.3 cm thick. Sample F of ice sheet 8.1 cm
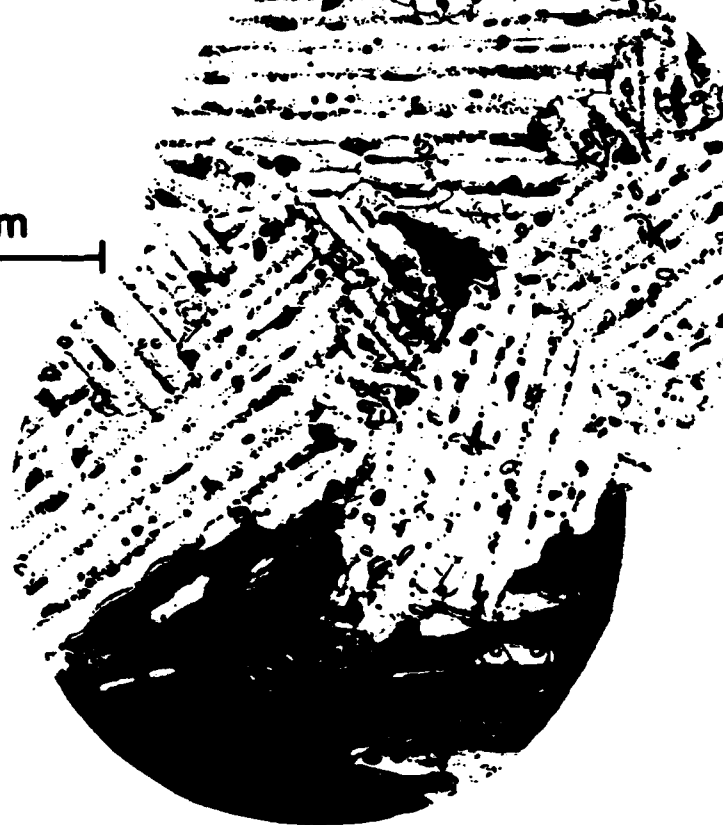
Figure 3.14: Samples G,H of urea ice sheet. Sample G of ice sheet 10.5 cm thick.

I 14.4 cm

J 19.7 cm
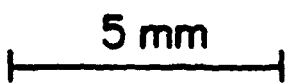
5 mm

Figure 3.18 Samples I, J of wear implants. Sample I of broken at 14.4 and 14.4

4 . Growth Experiment

4.1 Procedure:

As the ice sheet grew, normal incidence reflection coefficient readings were taken at 15, 17, 20, 25 and 190 kHz approximately every 0.5 cm of thickness. The shaft was rotated to allow for several independent areas to be insonified for each frequency. The amplitude of the waveform was recorded where the waveform showed a steady-state, i.e. the amplitude remained unchanged regardless of the number of cycles (See Fig 4.3a). The oscilloscope had two cursors. One cursor was kept constant throughout the experiment at ground level to mark the reference zero as well as the beginning of the transmit pulse. The amplitude of the reflected signal was chosen by moving the second cursor to the peak of the cycle chosen to represent the steady state value (shown with arrow). The difference in the peak value and the ground value were read off the display on the oscilloscope. The travel time of the received waveform was recorded by moving the second cursor to the beginning of the first peak of the received waveform. The difference in travel times between the two cursors was read off the oscilloscope display. Since the transducers had a beamwidth of approximately 40° at the lower frequencies, we took 4-5 readings at each of the lower frequencies and 6-7 readings at 190 kHz. The mean value was considered to be the amplitude of the reflected signal. Thickness samples were taken at periodic intervals (0.8 cm,2.4cm,

3.4cm, 5.1cm, 7.3cm, 8.1cm, 10.5cm, 12.6cm, 14.4cm, 19.7cm) to monitor the growth rate and any changes in the morphology of the ice. At the conclusion of the growth phase of the experiment, in order to statistically validate the accuracy of our reverberation data, we collected 127 distinct points of reflection coefficient data at 190 kHz and 20 independent points of reflection coefficient data at each of the lower frequencies. P.d.f.'s were tabulated for the different frequencies and the statistical variations were computed (See Figures 4.1a-4.1e).

Figure 4.1a: Histograms compiled from the normalized echo amplitude data
collected at the end of the growth phase of the expriment. Data were
collected at 15 kHz when the ice was 19 cm thick.
Mean value = 0.62
St. dev. = 0.014

15Khz pdf

Total Observations = 20

no. of observations

Reflection coefficient
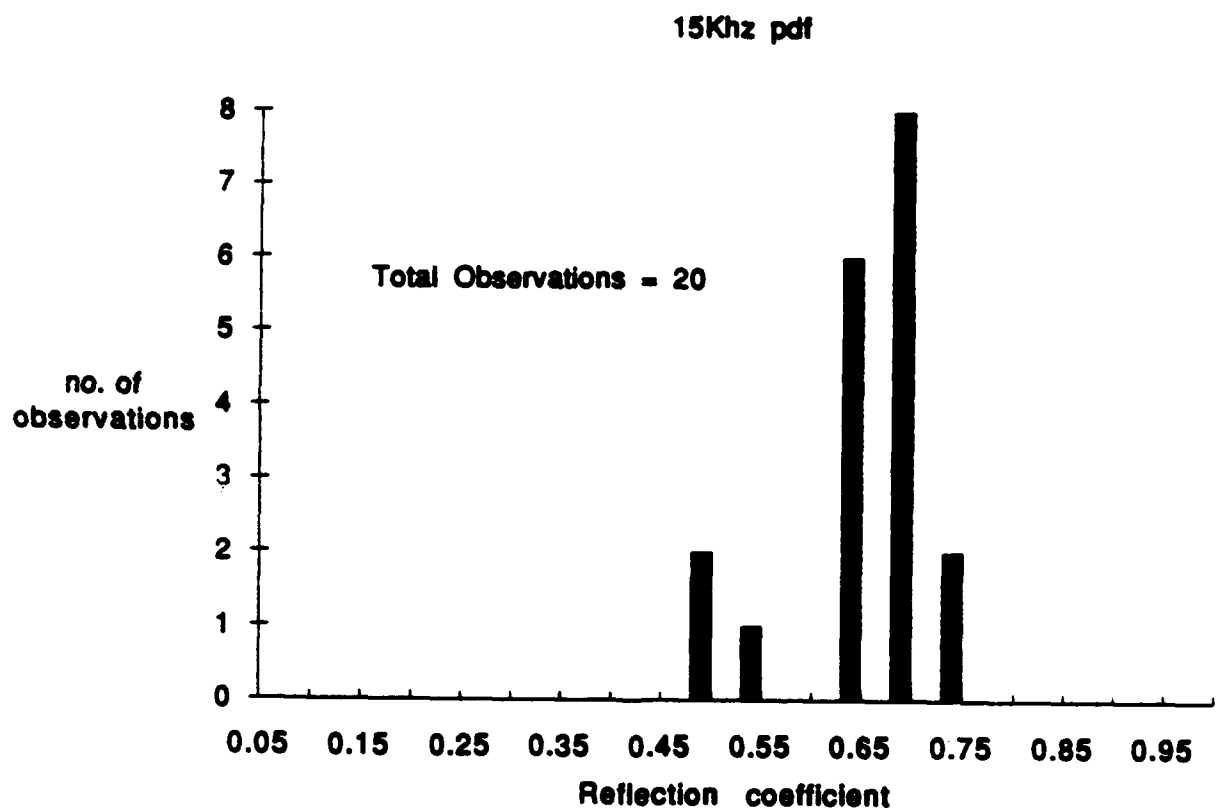
Figure 4.1b: Histograms compiled from the normalized echo amplitude data collected at the end of the growth phase of the expriment. Data were collected at 17 kHz when the ice was 19 cm thick.
Mean value = 0.62
St. dev. = 0.021

17 kHz pdf
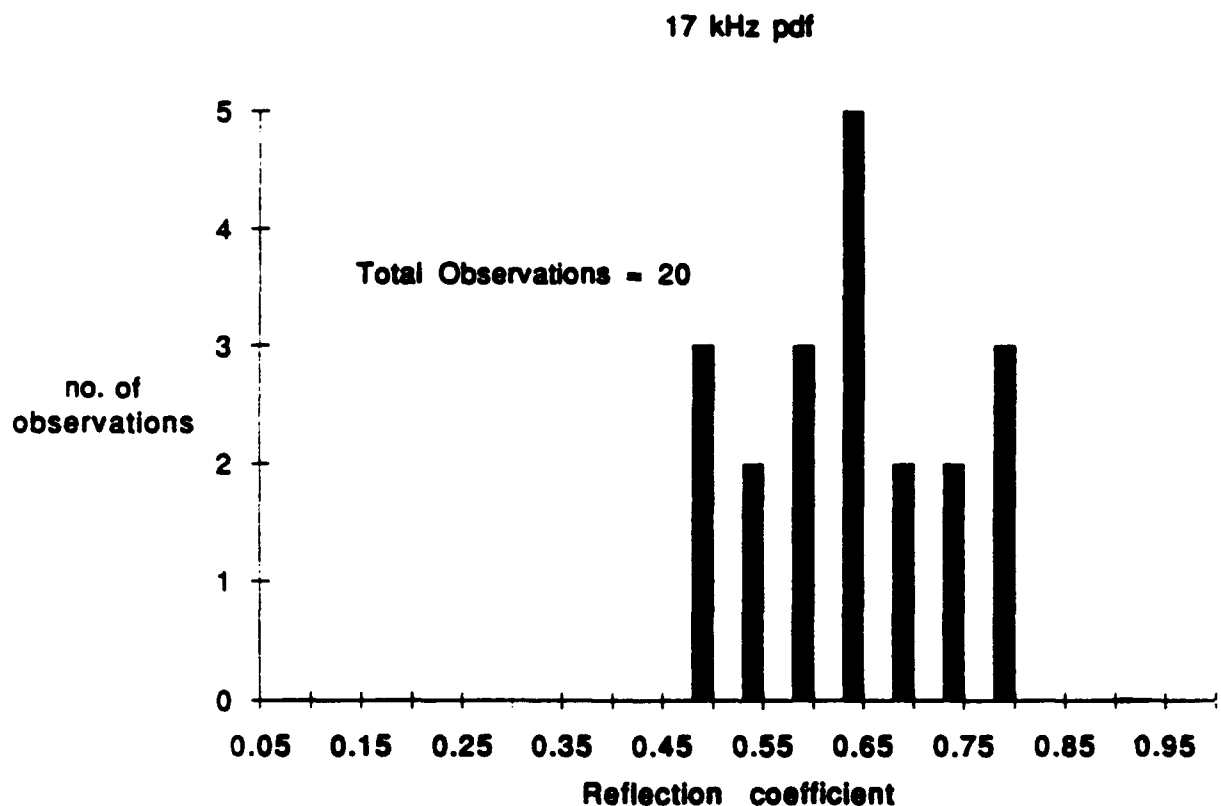
Figure 4.1c: Histograms compiled from the normalized echo amplitude data
collected at the end of the growth phase of the expriment. Data were
collected at 20 kHz when the ice was 19 cm thick.
Mean value = 0.16
St. dev. = 0.014

20 kHz pdf

Total Observations = 20
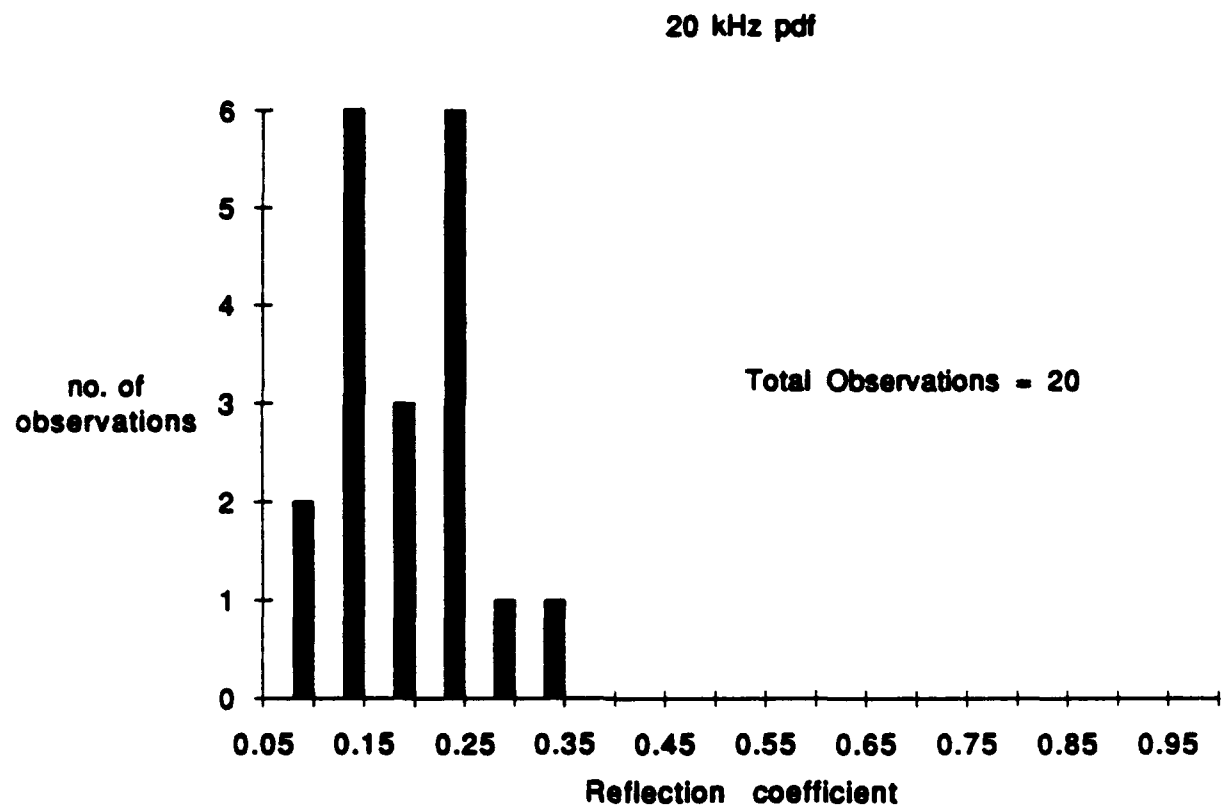
Figure 4.1d: Histograms compiled from the normalized echo amplitude data collected at the end of the growth phase of the expriment. Data were collected at 25 kHz when the ice was 19 cm thick.
Mean value = 0.56
St. dev. = 0.012

25 kHz pdf
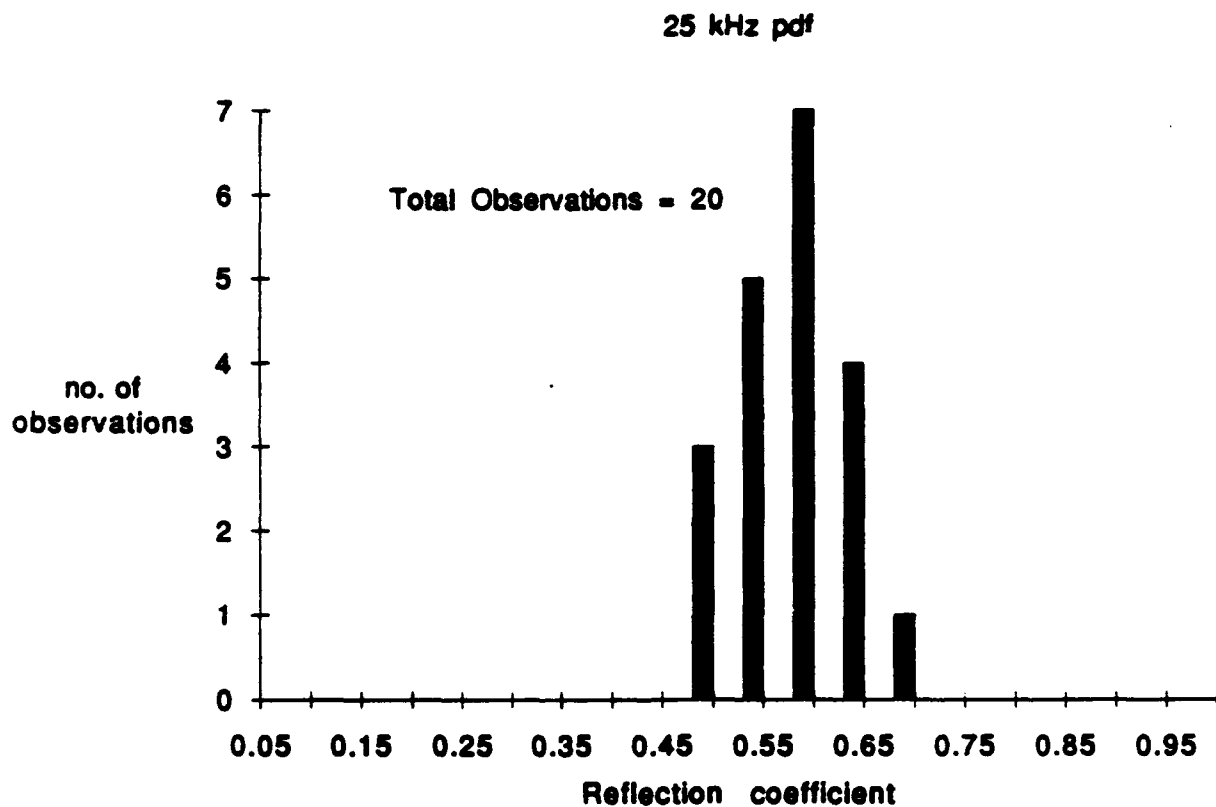
Figure 4.1e: Histograms compiled from the normalized echo amplitude data
collected at the end of the growth phase of the expriment. Data were
collected at 190 kHz when the ice was 19 cm thick.
Mean value = 0.12
St. dev. = 0.004

190 kHz pdf
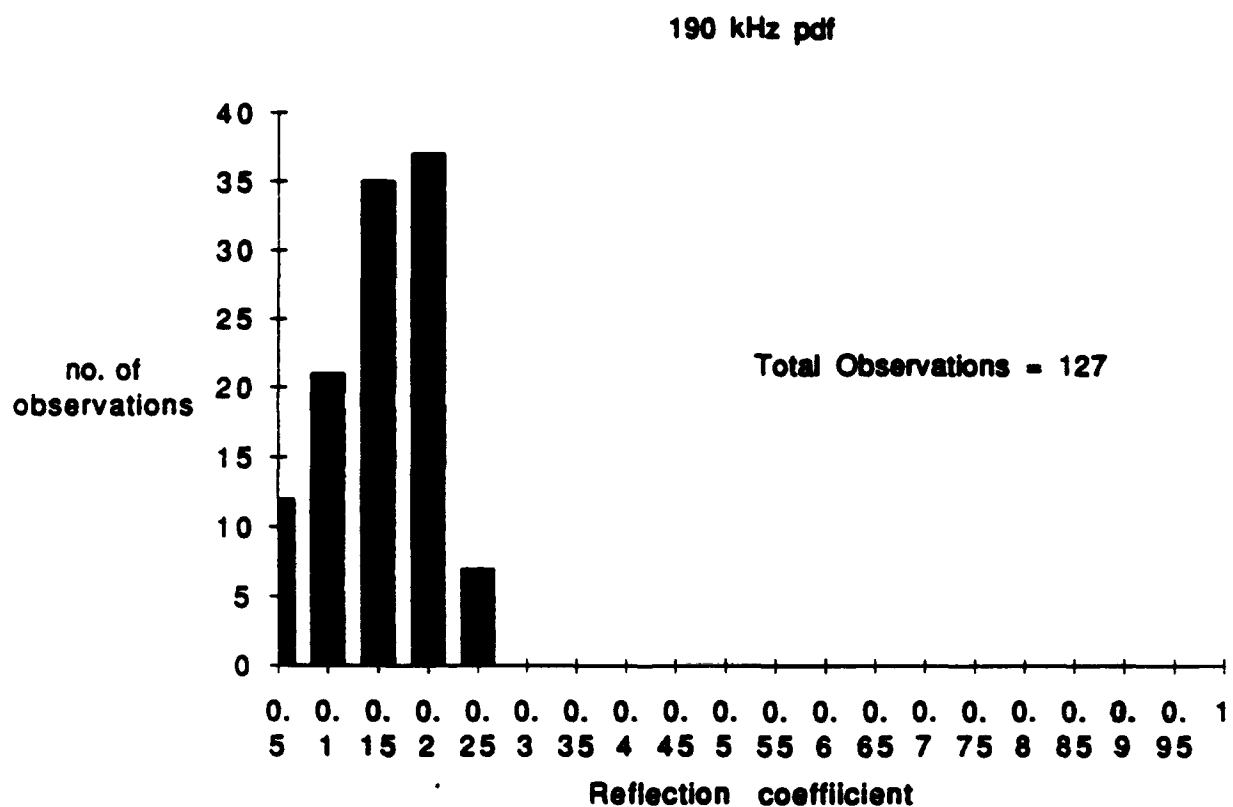
4.2 Precautions:

The surface of the transducer was soaped prior to its immersion in the water to prevent the formation of bubbles. The bubbles would create an impedence mismatch at the transducer-water interface that could adversely affect the coupling of the acoustic signal into the water. In order to prevent the downward transmission of acoustic energy as well as diminish the large acoustic coupling between the transducers, they were mounted on a baffling that consisted of a 1cm layer of cork, atop a 5cm layer of styrofoam. The cork had two circular cavities which snugly housed the transducers. A sponge was stuffed around the transducers to further reduce any coupling. To alleviate electronic coupling, all exposed wiring was physically separated and the receiving and transmitting electronics were placed apart. The coaxial cables from the transducers were taped to the shaft to prevent entanglement in the growing ice sheet. As a further precaution against cutting the wires while freeing the shaft from the ice sheet, a 45cm long circular sleeve was fit snugly around the shaft and extended from 15cm above the water level to 30cm below. (See Figure 4.2)

When determining the amplitude of the received pulse, care was taken to select the right position on the reflected waveform. It is important to choose that part of the waveform that represents the total steady-state reflected signal (See Figure 4.3a). At the lower frequencies, since attenuation through the ice

was low (0.3 dB/cm), there was considerable interference from the reflection off the top layer. For thin ice, the two reflections interfered quickly and a steady-state representative waveform was observed very early. However, as the ice thickened, null points appeared in the total reflection where the reflections off the top and bottom layer were 180 degrees out of phase (See Figure 4.3b). In some cases, 7 cycles were not enough to distinctly see the interference and so the cycles were increased to 10-12 and the amplitude was recorded where the signal leveled out. Sometimes, the reflected signal was highly dependent on frequency and small variations in frequency of 1 or 2 kHz would alter the reflected signal by 10-15 dB. This occured infrequently at the lower frequencies but often at the higher frequencies.

Figure 4.2: The physical setup of the growth phase of the experiment. The
transducers were mounted on an arm suspended from the tripod.
The electronics were housed outside the cold room and connected
to the transducers using 20 ft long coaxial cables.
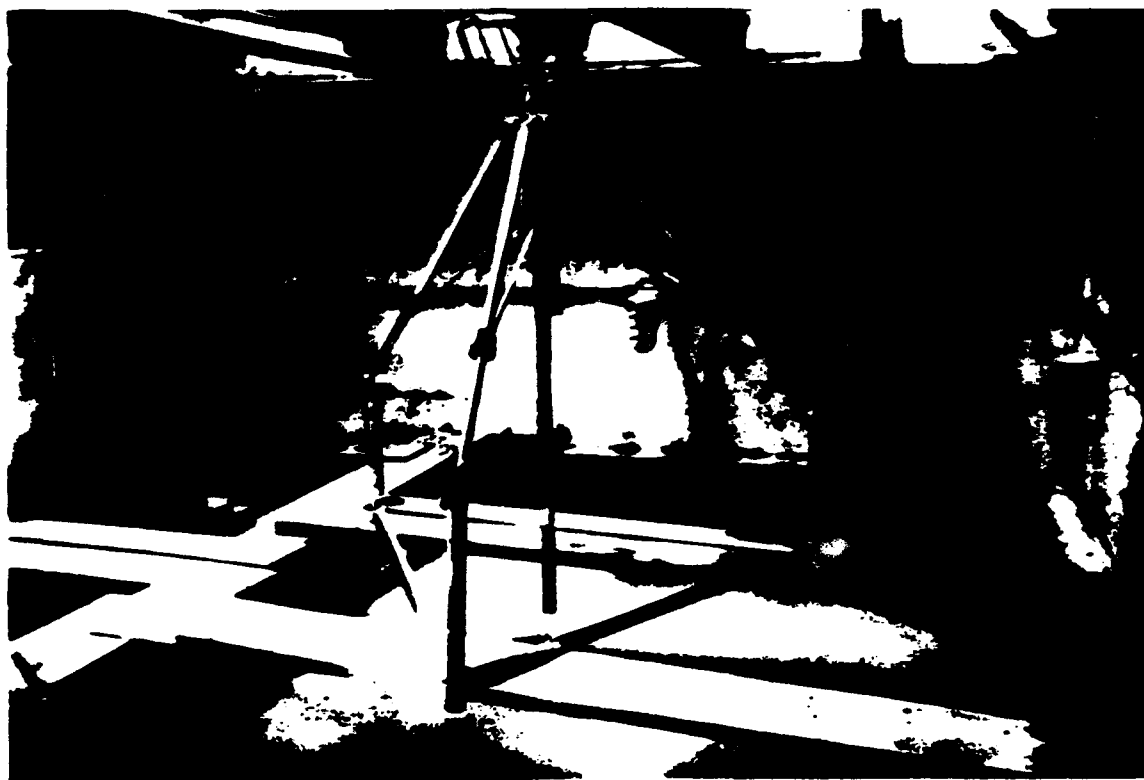
Growth Experiment Set up
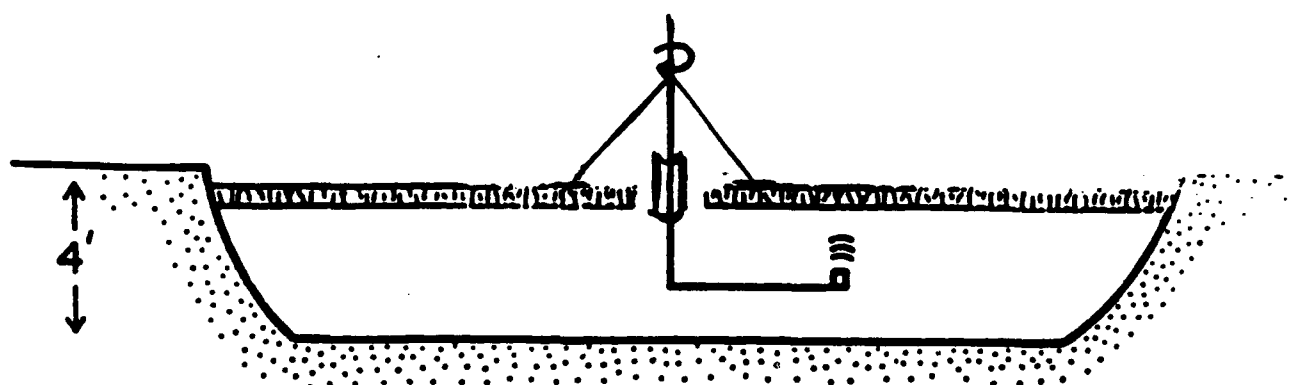
Figure 4.3a: Shows typical 20 kHz waveform. Travel time measured from beginning of pulse, while amplitude was measured by placing cursor at steady state peak of waveform.
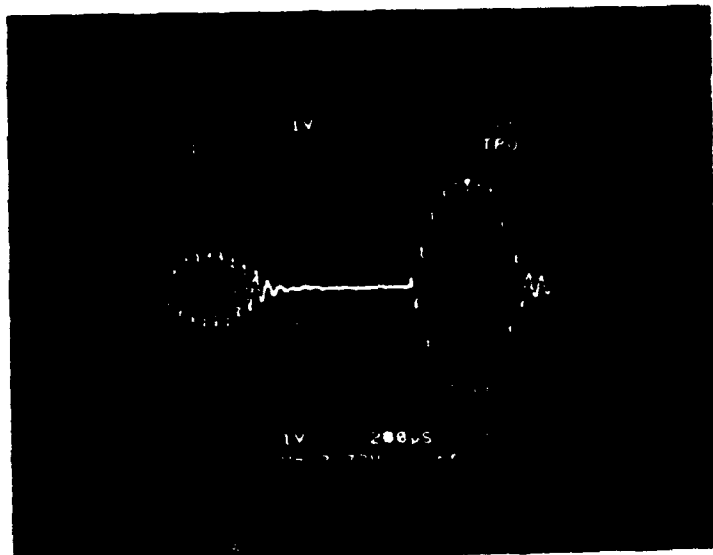
Figure 4.3b: Sometimes, due to interference of the reflections, the steady state value could not be determined within 7 cycles. Hence the number of cycles was increased till the signal levelled out. Photo 1: 7 cycles Photo 2: 10 cycles
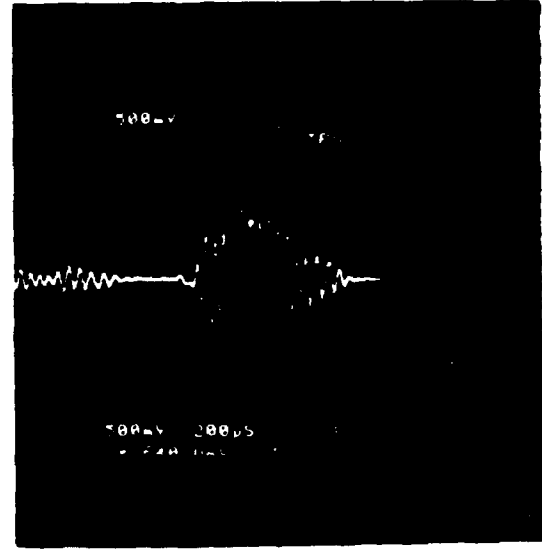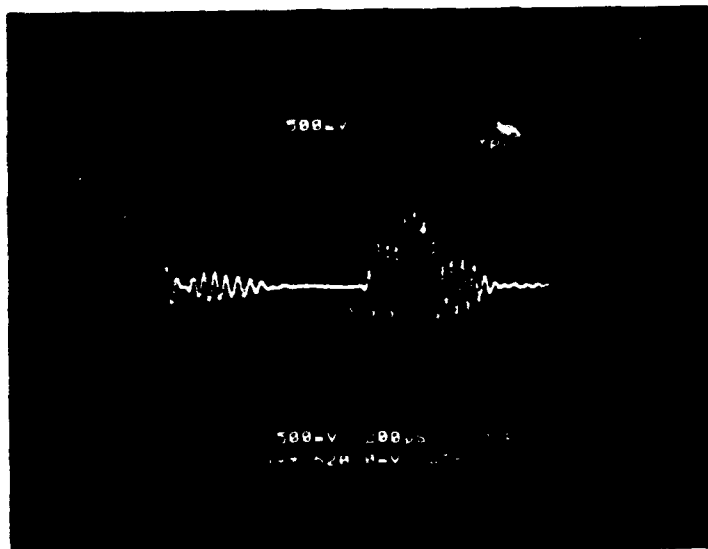
Figure 4.4 Shows the null caused by the interference of reflections from the top and bottom surfaces of the ice sheet. Amplitude of received signal is taken at the trough in the signal after confirming its steady state.
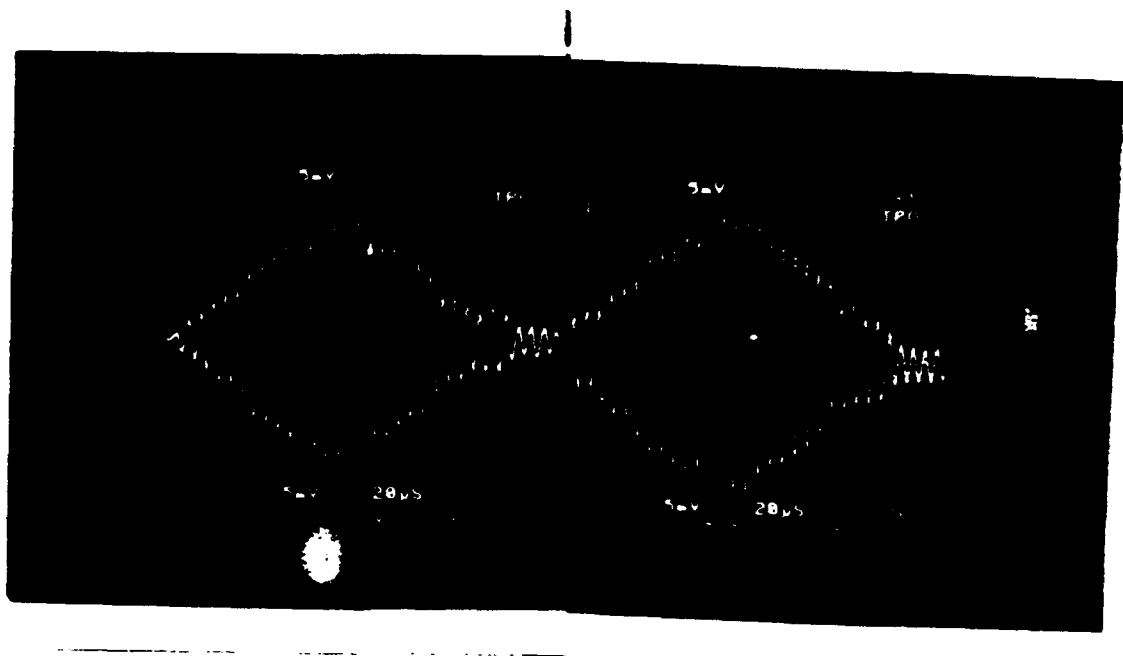
4.3 Observations:

The results of our growth experiment were rather surprising. Considering the similar morphologies of urea and saline ice and assuming that the acoustic properties are independent of the composition of the entrapped brine, we expected comparable bulk properties. However, we observed significant differences at the lower frequencies.

As the ice sheet grew, normal-incidence sonar echo amplitudes were recorded approximately every 0.5 cm of growth. Using the technique described in the sonar equation theory, the total normal-incidence reflection coefficient was derived. **Figures 4.4a-4.4e** show the amplitude of normal incidence reflection coefficients as a function of ice thickness at different frequencies. The experimental data were fitted using a plane-wave reverberation model for a single-layered lossy half-space bound at the top by air and the bottom by water (See Appendix 3). We assumed total reflection from the top air-ice interface. The model had four variable parameters: frequency, attenuation, bottom-surface reflection coefficient and velocity of the acoustic wave in the ice. The frequency parameter influenced the wave number and thereby affected the number of oscillations observed. The reflection coefficient from the bottom layer determined the final steady state value of the total reflection coefficient after the oscillations had settled down. The attenuation parameter determined the exponential decay of the reflection

coefficient envelope. The velocity parameter determined the spacing between the troughs and peaks.

As shown in Figure 4.4a, we observed that at 190 kHz, the total reflection for thin ice was dominated by the reflection from the air-ice interface. As the ice thickened, attenuation caused loss of signal from the the top interface. At approximately 8 cm thickness, almost all the reflected signal was from the bottom water-ice interface. The limited data for the thin ice allowed several velocities to fit the data equally well. Since the reflection coefficient dropped off quite rapidly we assumed a high attenuation of 2.86 dB/cm. Since after about 8 cm thickness, the reflection coefficient acheived a steady state, the bottom layer reflection coefficient was determined to be 0.12. By measuring the difference in echo arrival-times from the top and bottom layers for a 3 cycle signal, the velocity was found to be 3800 m/s.

The estimated standard deviation, σ', of the reflection coefficient is computed assuming that it has a normal distribution.

$$\sigma' = \frac{\sigma}{\sqrt{\text{no. of observations}}} t$$

where σ is the standard deviation of a particular data set. t is the adjustment factor derived from the t distribution that gives us a value that the data point has a 90% probability of lying within σ' of the mean. The value

of 't' is a function of the number of observations and the probability that data point lies within the specified range. Values for t were determined using the table on p692 of *Probability and Statistics* by Morris H. DeGroot.

On average we took about 5 measurements per thickness at 190 kHz. The variance of each data set was computed. The average standard deviation for the data sets was the square root of the average variance. The adjusted standard deviation of a typical data point, using the t distribution was then 0.04. Using information from the probability density function (p.d.f.), for the reflection coefficient we computed a standard deviation of 0.004.

For the 20kHz data the attenuation was almost a factor of 10 lower at 0.31dB/cm (See Figure 4.4b). This low attenuation allowed for a significant contribution of reflected signal from the air-ice interface. Phase cancellation between the upper and lower reflections caused a sharp drop in the total reflection coefficient at about 10cm. Unlike with the 190 kHz data the reflection coefficient did not drop off to a steady-state value. Rather, we noted an unusually high bottom-layer reflection coefficient of 0.35, very comparable to that of hard freshwater ice which has a reflection coefficient of 0.41. We took about 3-4 data points per thickness. The average standard deviation for the data points adjusted using the t-distribution is 0.08. The standard deviation of the reflection coefficient from the p.d.f data was 0.014. It might be noted that since the p.d.f. data for the lower frequencies is limited to 20

samples, it may not show the shape of a normal distribution. The velocity was estimated to be 3800 m/s which gave us the best fit to the data.

Results at the other lower frequencies showed consistently high reflection coefficients (See Figures 4.4c-4.4e). At 15kHz we observed a reflection coefficient of 0.6, an attenuation of 0.27 dB/cm and velocity of 3800 m/s. From the p.d.f. data we found the standard deviation of the reflection coefficient was 0.014. The average s.d. of a data point was 0.09.

At 17 kHz we observed a reflection coefficient of 0.4, an attenuation of 0.28 dB/cm and velocity of 3800 m/s. The standard deviation of the reflection coefficient from the p.d.f. was 0.0214. The average s.d. of a data point was 0.08.

At 25 kHz we observed a reflection coefficient of 0.4, an attenuation of 0.35 dB/cm. The velocity that provided a best fit for the data was 3950 m/s. The standard deviation of the reflection coefficient from the p.d.f. was 0.012. The average s.d. of a data point was 0.1.
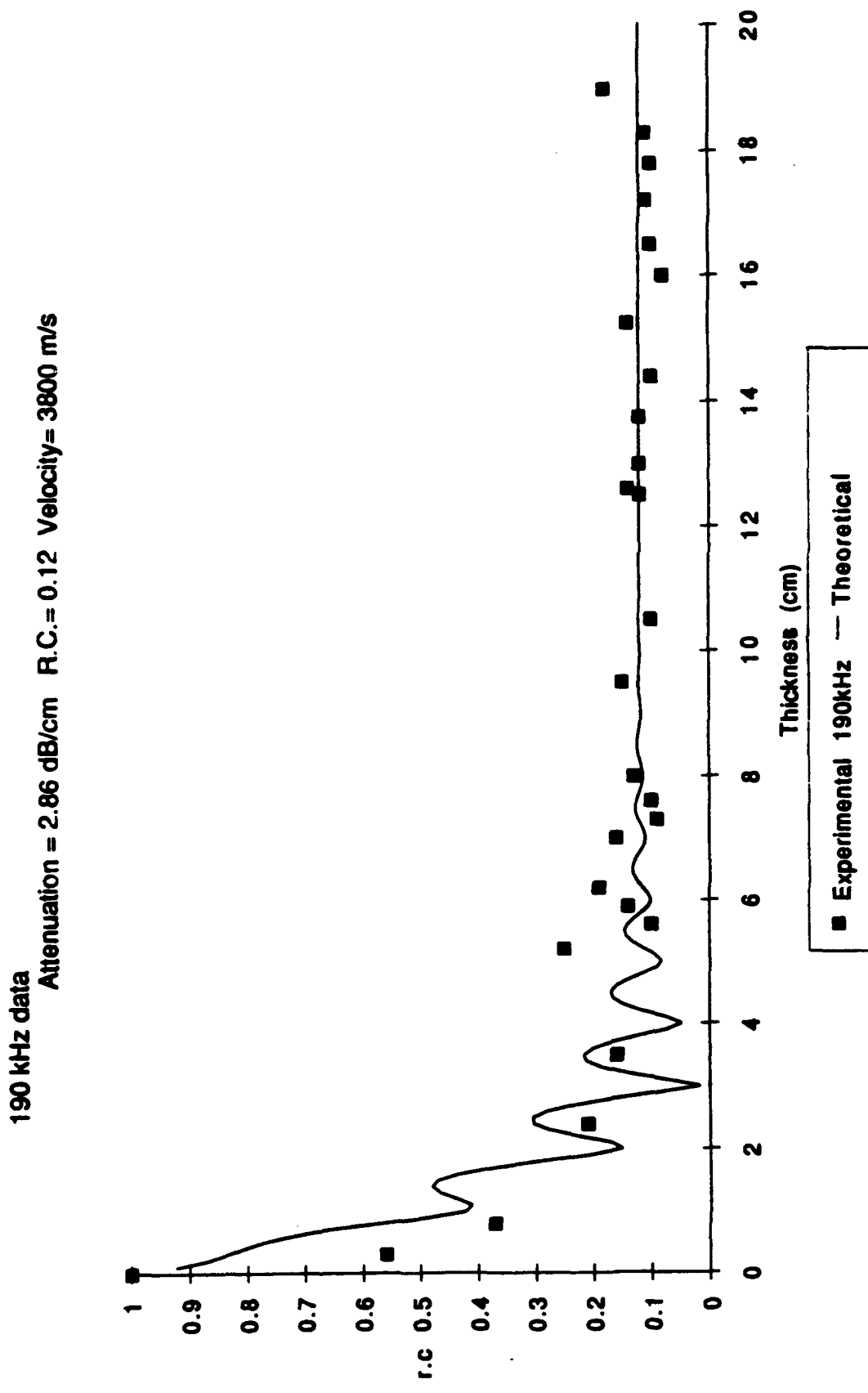
Figure 4.4a: Mean value of normalized echo amplitudes at 190 kHz as a function of ice thickness. Smooth curve was calculated using a simple plane wave reverberation model using the parameters shown.
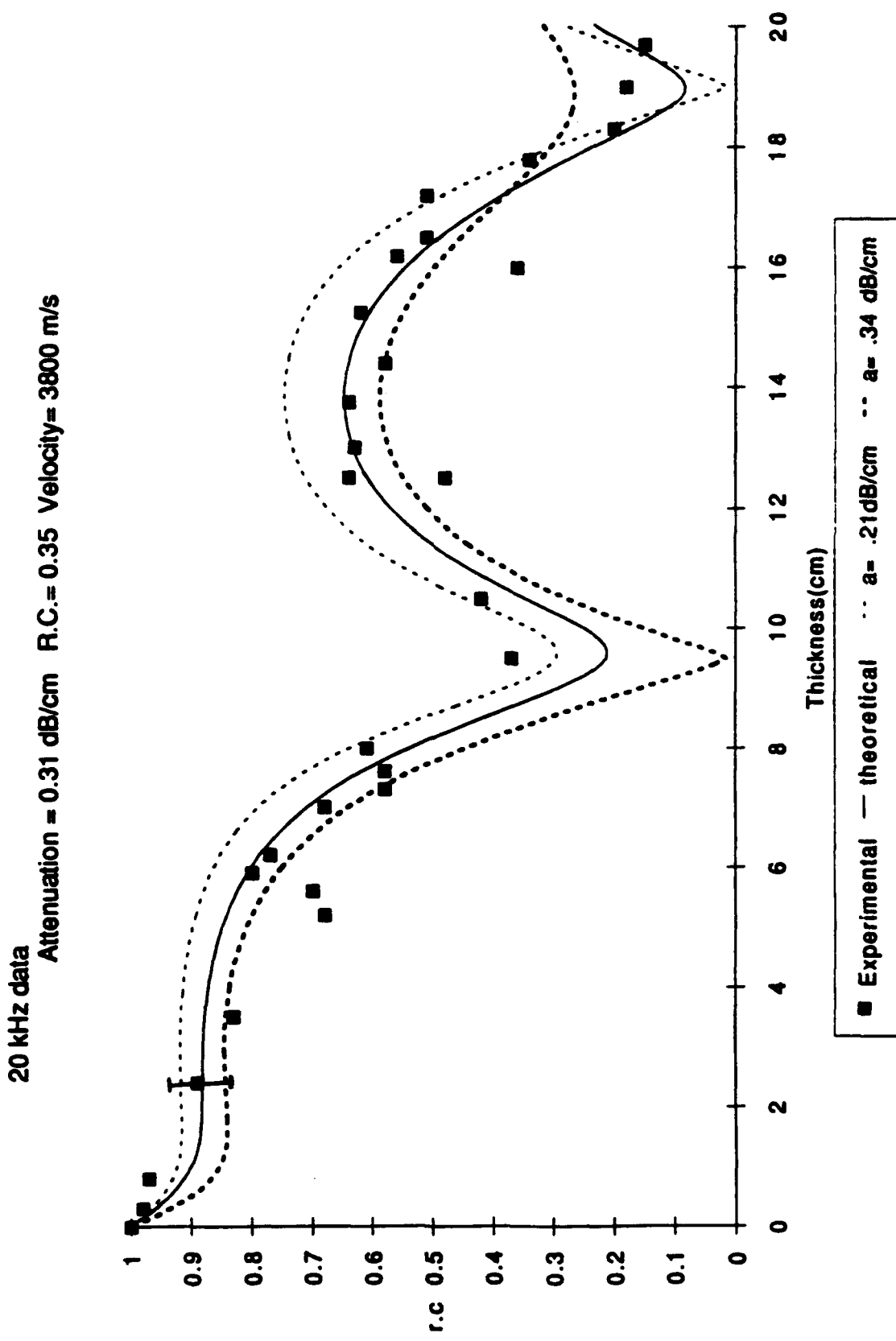
Figure 4.4b: Mean value of normalized echo amplitudes at 20 kHz as a function of ice thickness. Smooth curve was calculated using a simple plane wave reverberation model using the parameters shown. Also shows range of attenuation values.
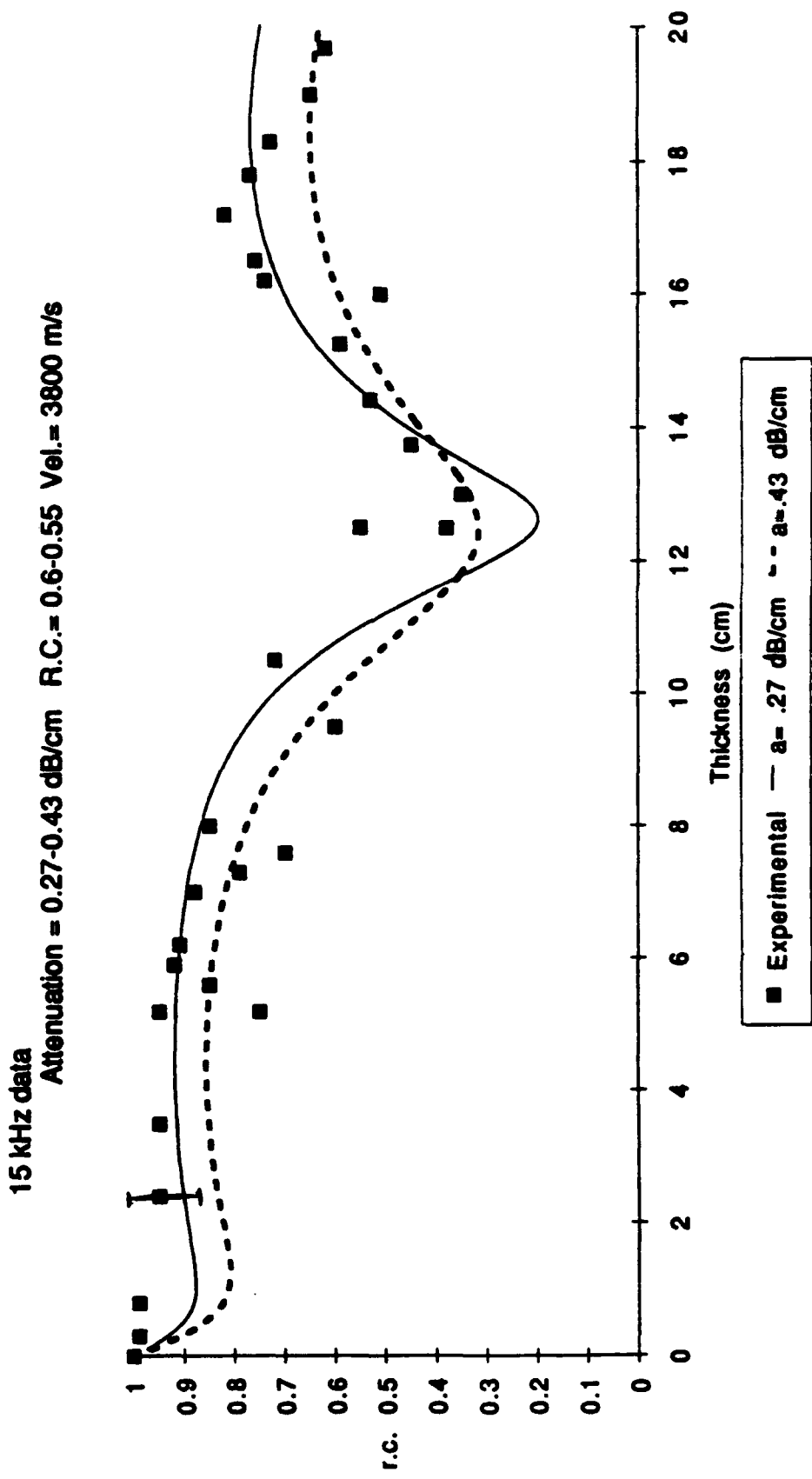
Figure 4.4c: Mean value of normalized echo amplitudes at 15 kHz as a function of ice thickness. Smooth curve was calculated using a simple plane wave reverberation model using the parameters shown. Also shows range of attenuation values.
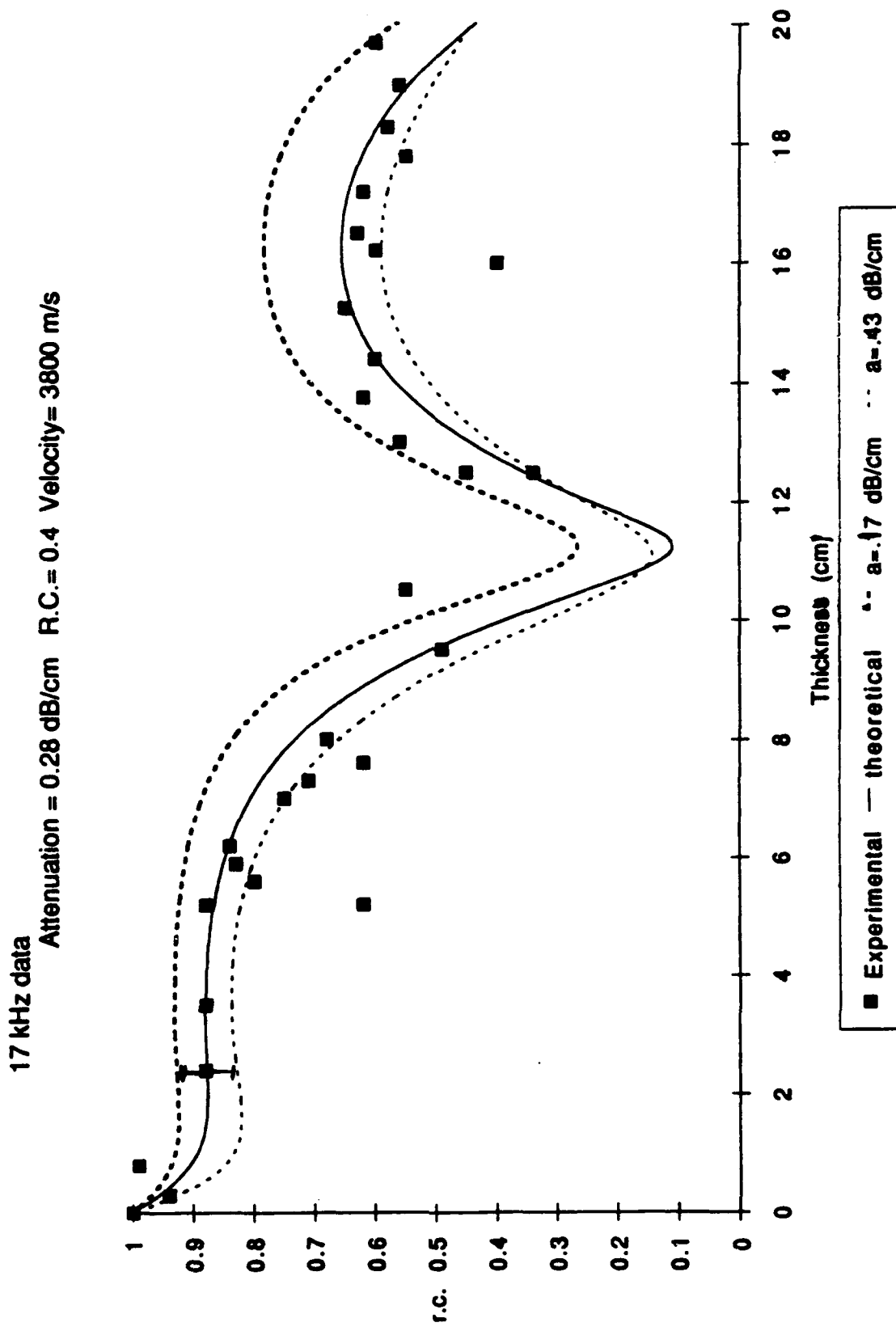
Figure 4.4d: Mean value of normalized echo amplitudes at 17 kHz as a function of ice thickness. Smooth curve was calculated using a simple plane wave reverberation model using the parameters shown. Also shows range of attenuation values.
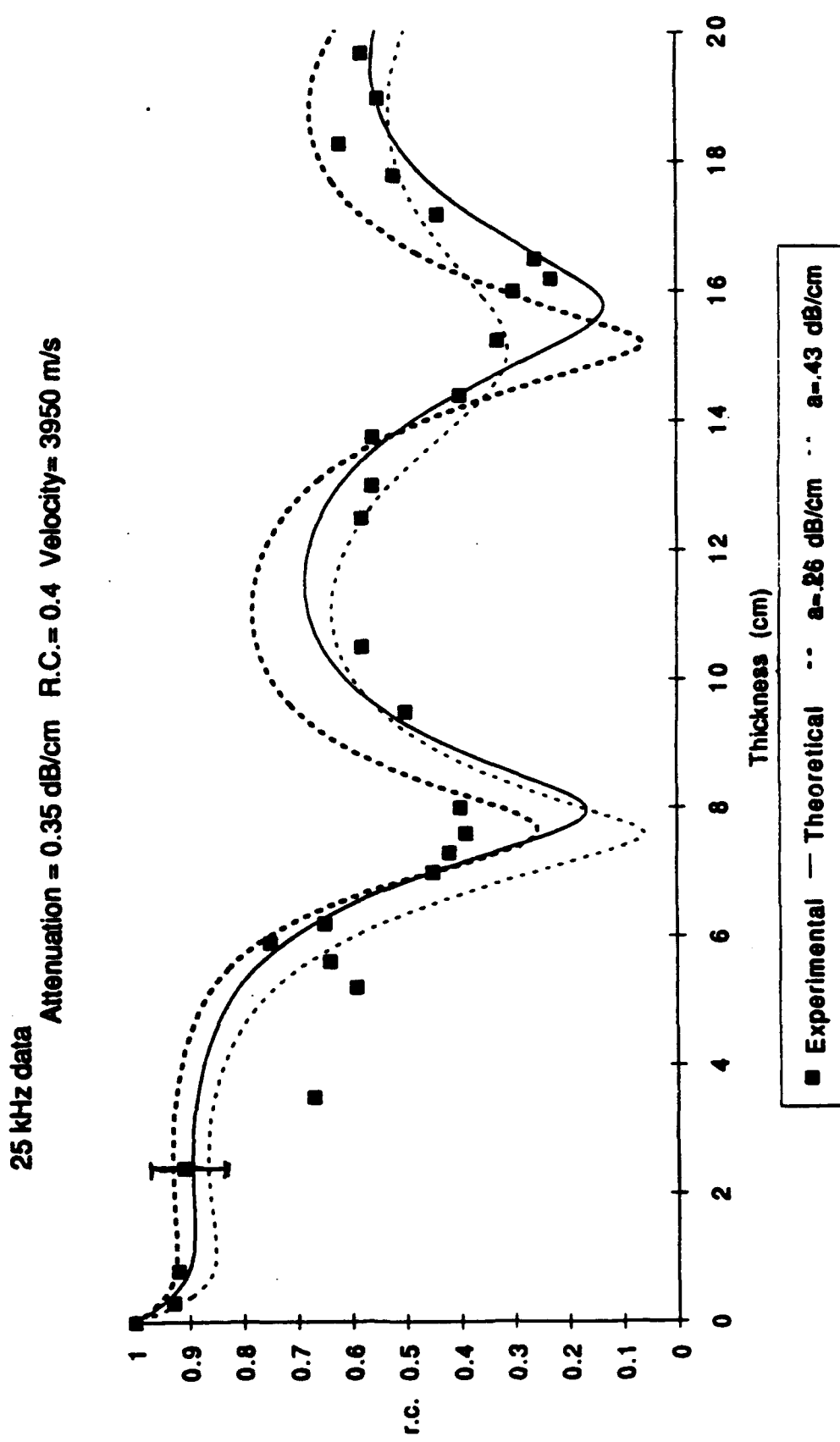
Figure 4.4e: Mean value of normalized echo amplitudes at 25 kHz as a function of ice thickness. Smooth curve was calculated using a simple plane wave reverberation model using the parameters shown.

Table 4.1

Summary of bulk acoustic values of the ice at various frequencies:

Freq.	r.c.	Avg. S.d.	Attenuation	Velocity
15 kHz	0.6	0.09	0.27 dB/cm	3800 m/s
17 kHz	0.4	0.08	0.28 dB/cm	3800 m/s
20 kHz	0.35	0.08	0.31 dB/cm	3800 m/s
25 kHz	0.4	0.1	0.35 dB/cm	3950 m/s
190 kHz	0.12	0.04	2.86 dB/cm	3800 m/s

4.4 Analysis

A comparison of experimentally derived values for urea ice showed marked differences from those derived from saline ice (See Figure 4.5a). Francois et. al. (1988) found low reflection coefficients for cold saline ice. This might indicate good coupling with the dendritic layer. As the ice warmed up, however, it experienced an upward change in reflection coefficient. It is speculated that warming temperatures may erode the complicated inter-connections between brine pockets formed during freezing, allowing freer flow of brine between the dendrites. This might reduce the attenuation suffered by the wave travelling through the ice. Hence, energy might be reflected from the stratigraphic discontinuities like bubble layers, higher in the ice and ultimately contribute to increased received signal levels. (Jezek et al. 1989)

For example, Francois found that at 20 kHz cold ice had a reflection coefficient of 0.07. Warm ice, however, had a reflection coefficient of 0.23, a tripling in value. At lower frequencies our data on urea ice showed even higher reflection coefficients, almost comparable to that of freshwater ice's reflection coefficient of 0.4.

In order to determine directly the reflection coefficient from the derived data, we analysed the waveform of the received pulse at a thickness of 19 cm.

The total distance travelled by the sound wave in the ice was thus 38 cm and at 3800 m/s it would take 100 µs before the reflection from the top surface would interfere with the reflection from the bottom surface. The pulse received from the 19 cm thick ice and the calibration pulse were digitized. The amplitude of the ice-reflected waveform was then compensated for $1/R$ losses based on its arrival time. By comparing the peak values before 100 µs of this waveform to the peak values before 100 µs in the calibration waveforms we derived the reflection coeff.ients for the bottom layer. These values were determined to be

Table 4.2

Frequency	Digitised r.c.	Model r.c.	Error
15 kHz	0.55	.6	-8.3%
17 kHz	0.45	.4	+12.5%
20 kHz	0.4	.35	+14%
25 kHz	0.45	.4	+12.5%
190 kHz	0.12	.12	

As shown above, these values agreed with the values that were used to fit the model with the experimental data within an error of 14 %, well within the allowable range of reflection coefficients.

We do not have a theory on the exact mechanism of reflection, but we

propose that clues might lie in the dendritic layer of the ice-water interface and the coupling effect it has on the transmission of acoustic energy into the ice. The porous nature of this layer, higher urinity, and permeability offer good acoustic coupling into the ice. Although not quantitatively measured, it appears that the dendritic tips of saline ice and urea ice are morphologically different. The saline ice dendrites have tips that are elongated and thin while the dendritic tips of urea ice appear shorter and sturdier. (See Figures 2.3, 2.4) Since the dendritic interface plays a major role in the incorporation of brine up into the body of the ice sheet, this might also have implications on the mechanism of brine incorporation into the two ice types. This might lead to changes in the volume of urea entrapped into the ice sheet. Consequently, the presence of a layer of high urea concentration close to the dendritic interface may lead to higher reflected energy. Unfortunately, unlike salinity measurements, no convenient method exists to accurately determine the urinity of an ice sheet as a function of its thickness.

Bogorodsky et al. (1975) proposed that most of the attenuation in young sea ice results from the viscous losses due to the presence of salt water in the inter-dendritic grooves. The results of experiments on elastic wave attenuation in ice structures show that the frequency dependence on attenuation is not very high, although absolute attenuation levels are very high. It is deduced that attenuation in sea ice is caused by losses due to viscosity or thermal conductivity, but not by scattering. (Bogorodsky et al.

1975) Thus they determined that calculation of the attenuation coefficient in sea ice gives the dependence

$$a \ (dB/m) = 7 \ (f \ (kHz))^{0.5}$$

A range of attenuation values were made to fit the data (See Figures 4.4a-4.4e). The central value that best fit the overall data yielded a close fit with Bogorodsky's et. al. predicted values at the lower frequencies. However, at higher frequencies Bogorodsky's attenuation was too low. It has been suggested by Jezek et al. (1990) that the changing structure of brine pockets due to the warming of the ice may affect the attenuation. A change in the brine incorporation mechanism as a result of morphological differences in the dendritic interface may lead to a difference in the viscosity o: the liquid-filled pockets. This might explain the discrepancy we observed in attenuation levels.

At lower frequencies, our data were below Jezek et. al. saline ice data. Saline ice reverberation data in the 8-20 kHz region suggests ice less than a few centimeters thick is less lossy than thicker ice, an observation that may be associated with a transition to a dendritic interface that occurs after 2 cm growth. (Jezek et al , 1989) This low attenuation allows considerable signal to be transmitted through the ice, contributing to very high total reflection coefficient of almost 0.9 for the thin ice thicknesses.

Over all frequency regimes, we measured attenuation greater than Langleben and Pounder (1970). Their measurements, however, were made at 1m depth on ice that was 2 m thick and the direction of propogation was perpendicular to the growth direction. This is also the low salinity portion of the ice column. Given the high urinity, porous and permeable nature of the dendritic interface, we hypothesize that the dendritic interface may play an important role in the acoustic attenuation process.

Reflection Coefficient vs Frequency

Legend: ■ Experimental △ Francois Cold Ice ✕ Francois Warm Ice ◇ Jezek et. al.
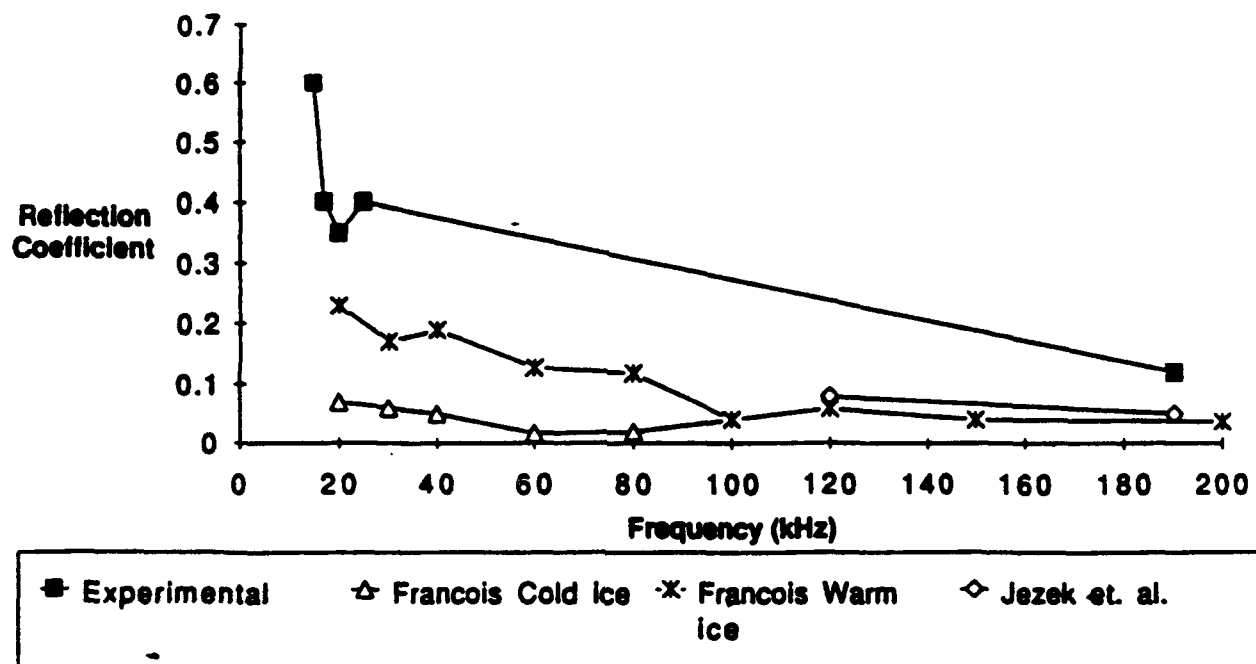
Attenuation vs Frequency

Legend: ■ Experimental — Bogorodski et.al. — Jezek et. al.
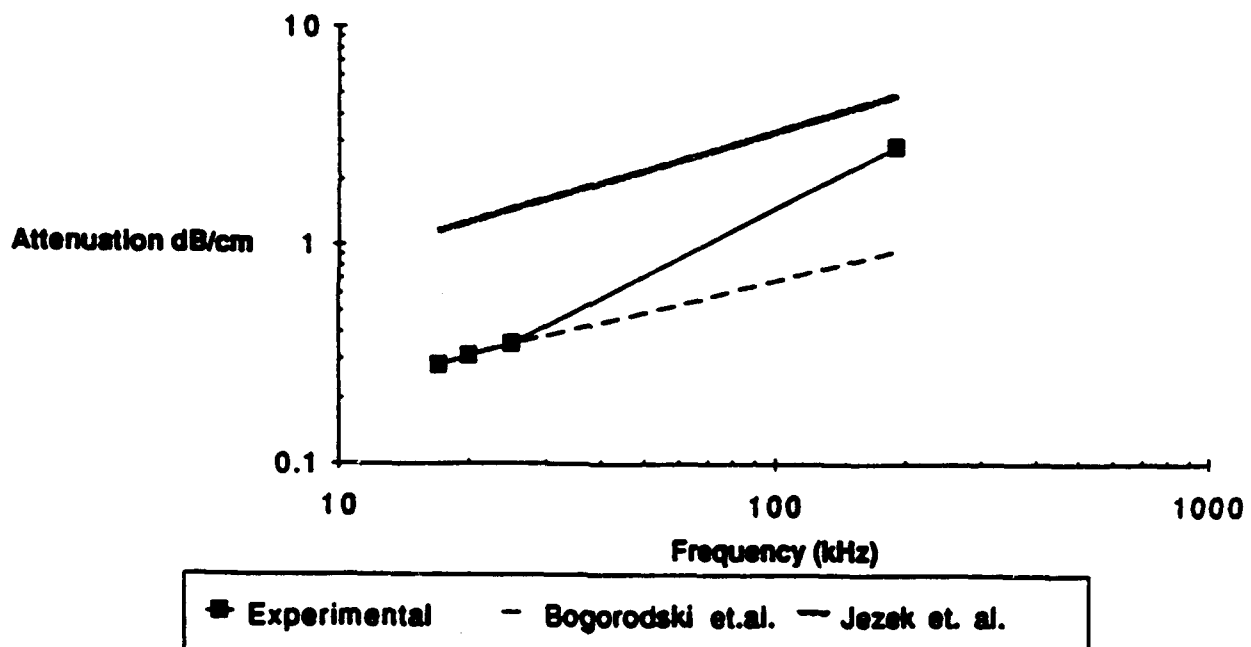
Figure 4.5: A comparison of the reflection coefficients and attenuation measured during our experiment with values computed by others over similar frequency range.

In order to determine the value of the attenuation independent of the models, the calibration and 19 cm thick ice digitised waveforms were used. The calibration waveform was reduced by multiplying it with the bottom surface reflection coefficient. This gave the waveform of the first reflection off the bottom water-ice interface. Then, this waveform was subtracted from the 19 cm thick ice waveform. The resultant waveform was reflection off the top surface of the ice and the subsequent multiple reflections.

Using the relationships of the pressure reflection coefficients derived in the theory of the plane wave reverberation model, we have

$$R_{12} = -R_{21}$$

and $$T_{12}T_{21} = 1 - R_{12}^2$$

Assume a lossly slab, bound at the top by medium 3 and at the bottom by medium 1. A normally incident wave of pressure P_i, is incident on the bottom surface. The 1st reflection from the bottom surface is simply

$$P_1 = P_i R_{12}$$

The second reflection i.e off the top surface is

$$P_2 = P_i T_{12}R_{23}T_{21}\exp(-a2h)$$

where h is the thickness of the slab and a is the attenuation.

The third reflection is

$$P_3 = P_i T_{12} R_{21} R_{23}{}^2 T_{21} \exp(-a4h)$$

Using these relationships we calculated the amplitudes of the reflections and noticed that they added up to the total amplitude of the observed waveform. The attenuation values were those used in the model.

Table 4.3

Frequency	R_{12}	2nd refl.	3rd refl.	Total	Observed 2nd+
15 kHz	.55	125mV	22mV	147mV	125mV
17kHz	0.45	380	55	435	420
20kHz	0.4	508	72	580	700
25kHz	0.45	160	12	172	220

The values of the attenuation used in the model are within ± 10% of the values found in the observed waveform data. We find that the attenuation values used in the model for 15 and 17 kHz are lower than those derived from the waveform. The opposite is true for 20 and 25 kHz.

The model values of attenuation seem to fit the data of the thicker ice better. By lowering the attenuation, about 10-20%, the model seems to have a better fit on the thin ice section of the data. This substantiates the hypothesis that attenuation rates change as the ice grows thicker.

15 kHz 2nd + reflections

Legend: □ 1st reflection   ■ Total reflection   — Resultant

Amplitude (V)
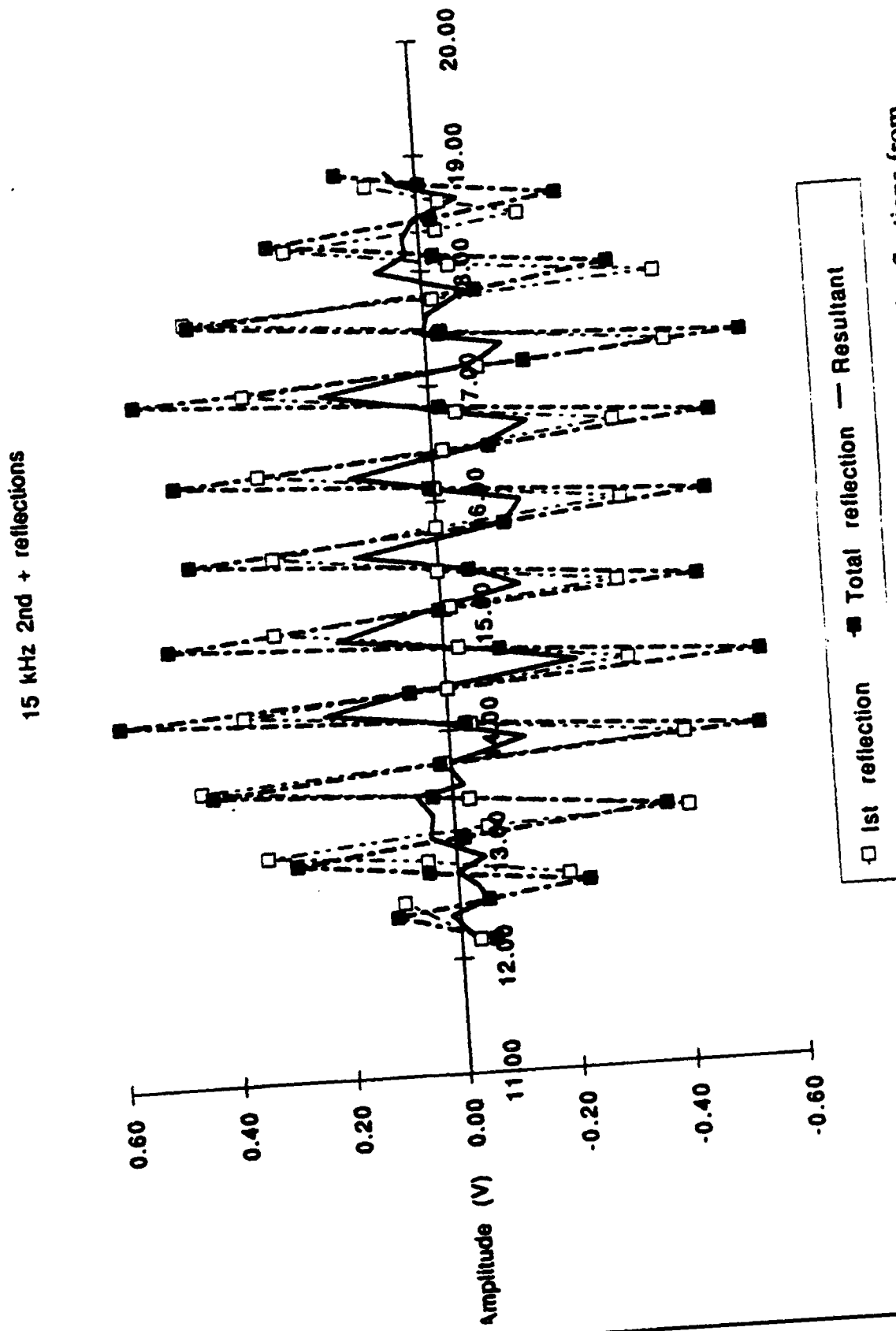
Fig 4.6a: Shows the resultant waveform of the 2nd and 3rd reflections from the ice sheet at 15 kHz. Gives an independent measure of the ice sheet at 15 kHz. Gives an independent measure of attenuation, velocity and r.c. $R_{12} = 0.55, T_{12} = 0.45, T_{21} = 1.55$. Incident signal = 600mV

17kHz 2nd+ reflections
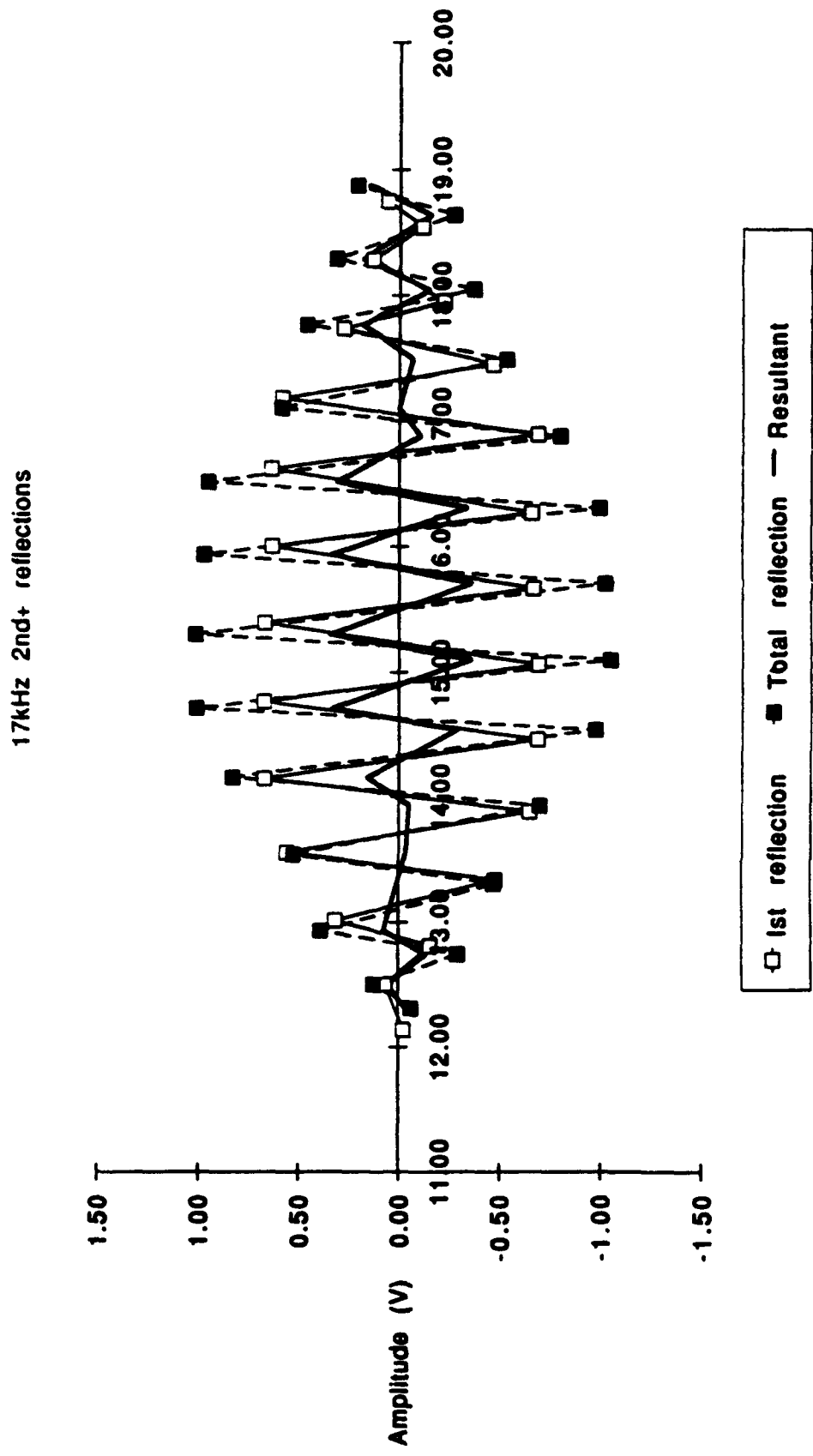
Fig 4.6b: Shows the resultant waveform of the 2nd and 3rd reflections from the ice sheet at 17 kHz. Gives an independent measure of attenuation, velocity and r.c. $R_{12} = 0.45, T_{12} = 0.55, T_{21} = 1.45$ Incident signal = 1.56V

20 kHz 2nd + reflections

□ 1st reflection ■ Total reflection — Resultant
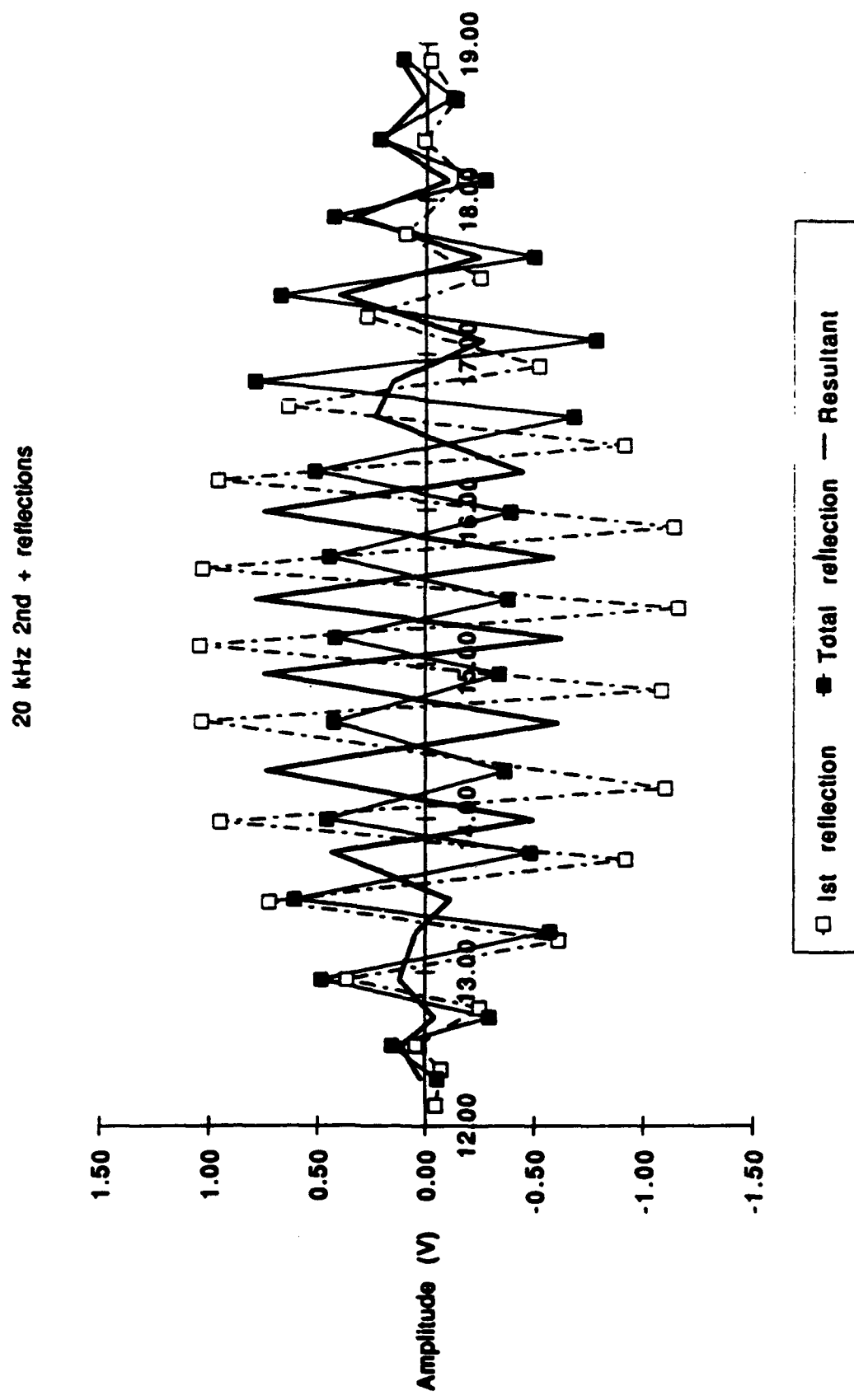
Fig 4.6c: Shows the resultant waveform of the 2nd and 3rd reflections from the ice sheet at 20 kHz. Gives an independent measure of attenuation, velocity and r.c. $R_{12}=0.4, T_{12}=0.6, T_{21}=1.4$ Incident signal = 2.36V

25 kHz 2nd + reflection
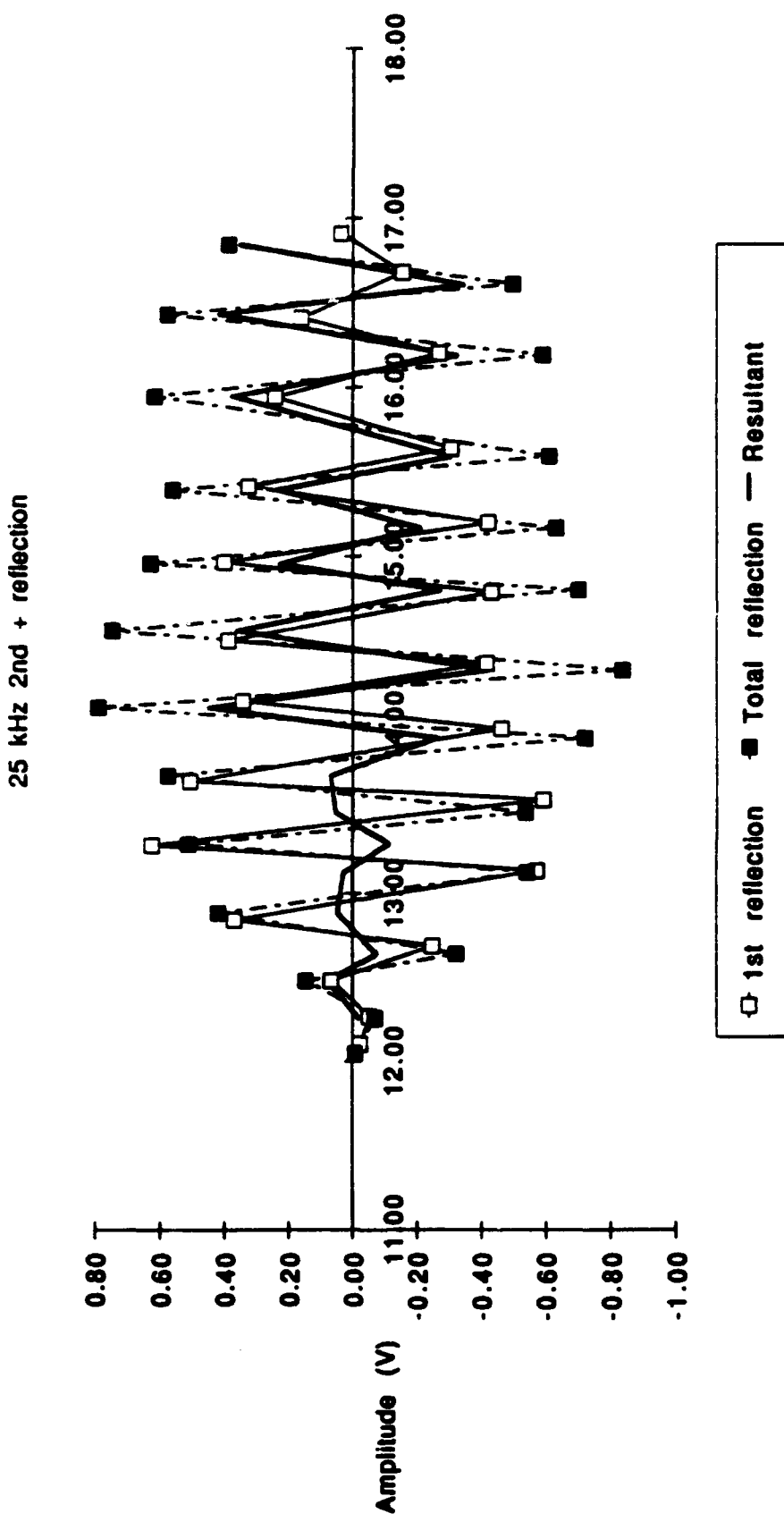
Fig 4.6d: Shows the resultant waveform of the 2nd and 3rd reflections from the ice sheet at 15 kHz. C:ves an independent measure of attenuation, velocity and r.c. $R_{12} = 0.45, T_{12} = 0.55, T_{21} = 1.45$ Incident signal = 900mV

5. Diffraction experiment:

5.1 DiffractionTheory

Diffraction can be qualitatively understood by graphical constructions using Huygen's principle. However in order to get a quantitative measure of the amplitudes of diffracted waves we can quantify Huygens principle by using the Helmholtz-Kirchoff (HK) integral. The H-K integral relates the wave field U on the scattering surface to the field U(Q) at a point Q. We find that U at the surface is approximately RU_s where U_s is the incident wave field and R is the reflection coefficient. The H-K integral is

$$U(Q) = \frac{1}{4\pi} \int_s R \frac{\partial}{\partial n} \frac{U_s e^{-ikr}}{r} \, dS \qquad (1)$$

where e^{-ikr}/r is the "point source" or Green's function for the Huygen's wavelets, r is the distance from dS to Q, $\partial/\partial n$ is the derivative along the normal to the surface and the $\partial/\partial n(\ )$ is evaluated at dS. This equation assumes that the source and receiver are in the same medium and that the reflection coefficient, R is constant over the entire rough surface. Since U_s has the form of an expanding wavefront, it has dimensions of m^{-1} and is generally a function of frequency. (Clay and Medwin, p 320)

Let,

$$U_s = \frac{e^{-ikr}}{r} \qquad (2)$$

Then,

$$U(Q) = \frac{R}{4\pi} \int_s \frac{\partial}{\partial n} \frac{e^{-2ikr}}{r^2} \, dS$$

To find the field strength at Q, we convolve U(Q) with P(f), the emission spectrum of the source, at range r_0 and get

$$p(t,Q) = r_0 \int_{-\infty}^{\infty} P(f) \, U(Q) \, e^{i2\pi ft} \, df \qquad (3)$$

For an impulsive source the frequency spectrum P(f) is a constant, P_δ, and we get

$$p(t,Q) = r_0 \, P_\delta \int_{-\infty}^{\infty} U(Q) \, e^{i2\pi ft} \, df$$

Defining,

$$u(Q,t) = \int U(Q) \, e^{i2\pi ft} \, df \qquad (4)$$

and substituting we find that

$$p(Q,t) = r_0 \ P_\delta \ u(Q,t) \tag{5}$$

Since we will only be calculating relative amplitudes, we need only calculate u(Q). By substituting the H-K integral into (4) and integrating we find that

$$u(Q) = \frac{R \ \delta\left(t - \frac{2z}{c}\right)}{2z} - \frac{zR}{4\pi} \int_{-\infty}^{\infty} df \int_{\theta_1}^{\theta_2} \frac{\exp\left(i\omega t - \frac{2i\omega r}{c}\right)}{r^2} \tag{6}$$

where the first term is the reflected wave when the source is under the surface. The second term represents the diffracted wave where the H-K integral has been transformed to a line integral over the polar azimuth, θ, measured in the plane of the diffracting surface. This integral appears often and we can define D(t) as follows to obtain Trorey's (1970) form:

$$D(t) = \frac{c^2}{4} \int_{-\infty}^{\infty} df \int_{\theta_1}^{\theta_2} \frac{\exp\left(i\omega t - \frac{2i\omega r}{c}\right)}{r^2} d\theta$$

We can calculate the diffracted boundary wave for a simple plate, and then construct more complicated surfaces by joining a number of plates together and superimposing the solutions of the individual plates (Jezek, 1980). Let the

source be on the vertical z axis and a flat plate of width r_1- r_2 measured on the x-axis, where the range vectors R_1 and R_2 are measured from the source at Q to the edges of the plate. The plate extends to plus and minus infinity on the y-axis. The diffracted wave from the edge at x_1 is generated as R_1 moves from $\theta = 0$ to $\pi/2$ and simultaneously as R_1 moves from $\theta = 0$ to $-\pi/2$. Thus, for the edge we have

$$u(Q) = \frac{R \ \delta\left(t-\frac{2z}{c}\right)}{2z} - \frac{R z}{\pi c^2} D(t) \tag{7}$$

where

$$D(t) = \frac{2T_x}{t}\left(t^2 + T_x^2 - T_1^2\right)^{-1}\left(t^2 - T_1^2\right)^{\frac{1}{2}} \qquad t > T_1$$

$$D(t) = 0 \qquad\qquad\qquad\qquad\qquad\qquad t < T_1$$

T_x is the time corresponding to the horizontal range to the diffractor divided by wave velocity and T_1 is the range to the diffractor divided by the wave velocity. As t tends to T_1 , D(t) becomes infinite and has an impulsive response. In order to estimate the amplitude of arrivals when $t=T_1$ we average the integral over a small time interval Δ . Letting $t= T_1 +\Delta$ and simplifying by dropping the second order terms, we find that for $T_1 \le t \le T_1+ \Delta$

$$D(t) = 2\left(T_1^2 \, \Delta\right)^{-1} \tan^{-1} \frac{\left(2T_1 \, \Delta\right)^{\frac{1}{2}}}{T_x} \tag{8}$$

Equation (7) is the solution for a semi-infinite strip when the source is over the strip and the other edge is very far away. In our experiment, this is the case when the transducers are under the ice sheet.

For the case where the source is not over the strip, and both edges are illuminated then

$$u(Q) = \frac{R \, z}{\pi c^2} \left(D_1(t) - D_2(t)\right)$$

Here the specular reflection is missing, and the integral over θ has two boundary waves. The boundary wave from the near edge of the strip (R_1) has a positive sign, and the boundary wave from the far edge (R_2) has a negative sign.

5.2 Procedure

For the diffraction phase a slot was cut in the ice when it was 19 cm thick. The slot was 1.84 m long and 1.8 m wide. Particular effort was spent on making sure that the edges of the ice were cut as straight as possible. The transducer shaft was removed from the tripod and mounted on a sliding apparatus that allowed the transducers to be moved gradually from completely under the ice, to under the edge, to completely under the open water. The transducers were excited at 20 kHz and short bursts of 200 μs were transmitted. The pulse generator put out a signal of 2 cycles.

To ensure that the transducers were horizontal, the transducer arm was mounted such that it followed a 3.6° slope as it traversed the length of the sliding apparatus. Accordingly, compensation had to be made to adjust for the difference in depth as the transducers were moved. The total change in depth for the entire length of the transducer traverse was 8.5cm. (See Figure 5.1a,b)

Measurements of the reflected and diffracted echo arrivals were made every 5 cm, from 85 cm away from the edge under the ice to 50 cm away from the edge under the open water. The first waveform was termed -85 cm, the waveform directly under the edge was termed 0cm, while the last waveform was termed 50 cm (See Figure 5.1c).

Figure 5.1a: Diffraction experiment set up showing the position of the
transducers and their motion under the edge. The transducers were
moved in increments of 5 cm.

Diffraction Experiment Set Up
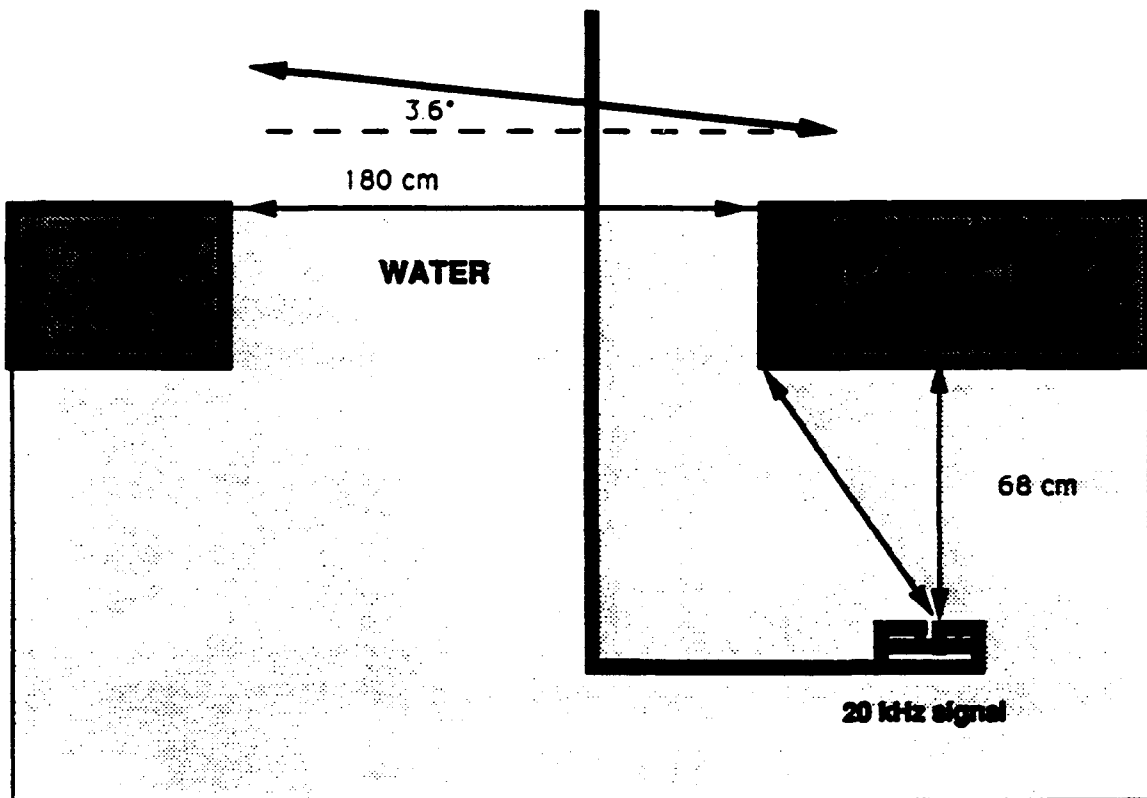
Lateral distance versus Surface distance

Distance from surface
(cm)

80.00
70.00
60.00
50.00
40.00
30.00
20.00
10.00
0.00

85 75 65 55 45 35 25 20 15 10 - 5 0 5 10 15 20 25 30 35 40 45 50

Lateral Distance from edge (cm)

FIG 5
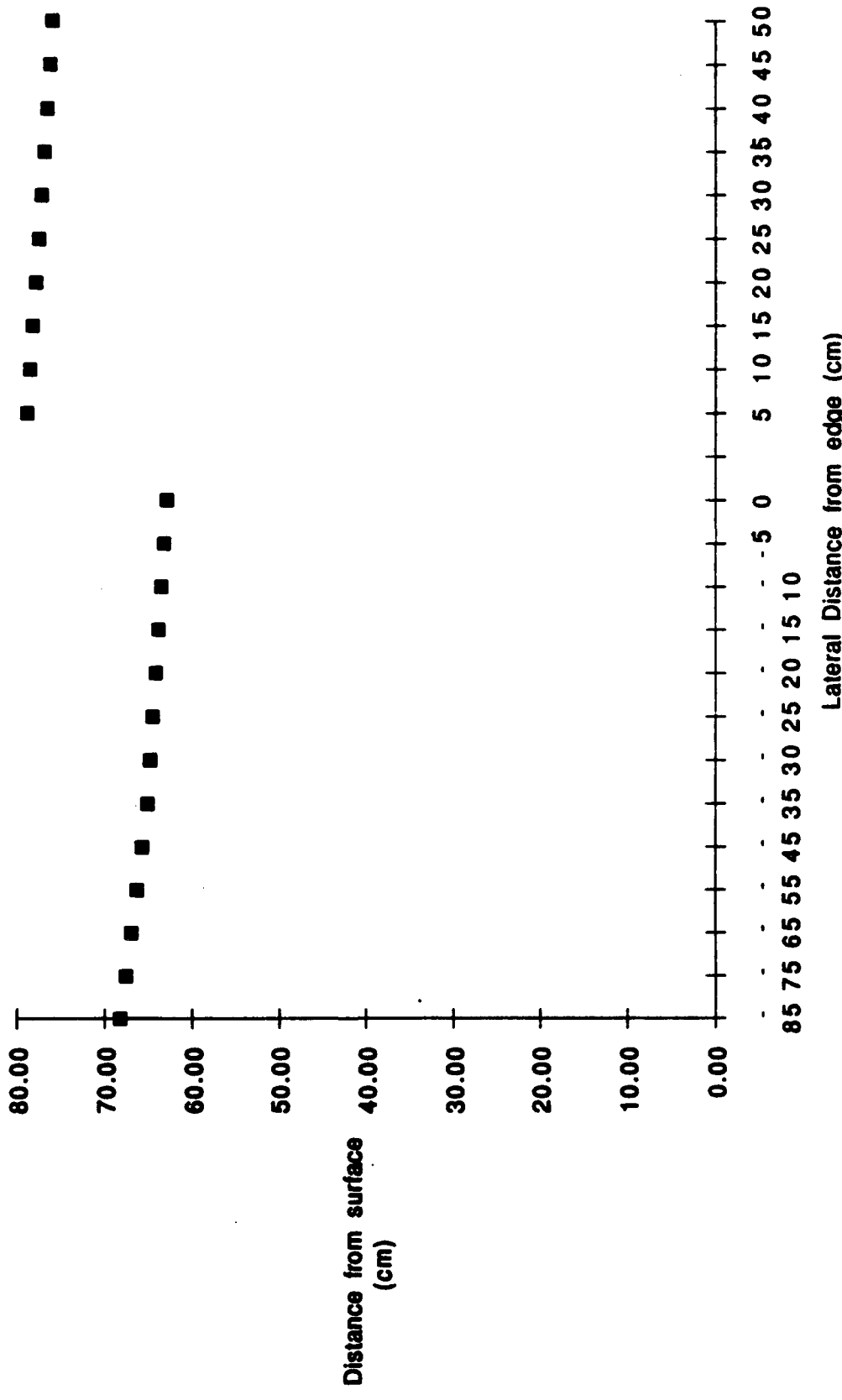
Figure 5.1c: The position of the tranducers when completely under the ice was termed -85 cm. The transducer was moved out towards the edge in increments of 5 cm. The position when the tranducers were under the edge was termed 0 cm. When the transducers were furthest to the left, the position was termed 50 cm.

Diffraction Experiment Co-ordinate system

ICE

180 cm

ICE

WATER

180 cm

135cm

0 cm

Transducers

86 cm
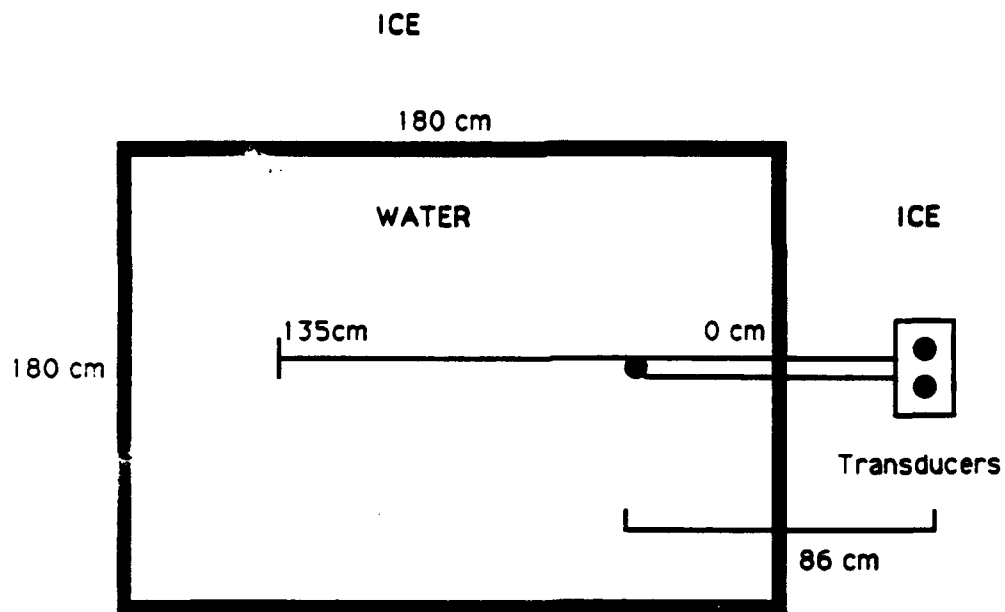
Transducer position

50 cm   0 cm   -85 cm
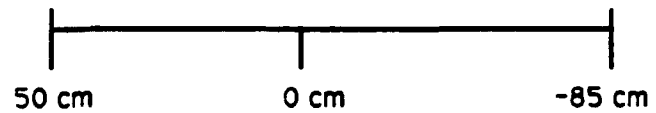
A number of reflections were received and diffracted echo from the edge of the ice sheet was isolated. While the transducers were under the ice sheet, echoes were received from the ice surface, the edge of the ice sheet, the edge of the water, and probably from the sidewalls. While the transducers were under the water, echoes were received from the edge of the ice, the edge of the water, the lateral edges and probably the sidewalls. (See Appendix 4). The travel times of reflected the diffracted arrivals were recorded by moving the second cursor to the beginning of the waveform of interest.

Since the pulsewidth was almost 200 microseconds, the diffraction pulse received from the edge merged with the reflection from the ice sheet when the transducers were about 25 cm away from the edge, under the ice. When the transducers were under the water the diffracted arrival could be detected until about 20 cm from the edge. Beyond that range, its arrival could be noted but it was swamped by the reflection from the water before the signal peaked (See Figure 5.2).

The diffracted arrival from the water edge was also noticed from about -45 cm until the edge. Once the transducers were underwater, the diffracted arrival from the water edge was swamped by the reflection from open water (See Figure 5.3a,b). The reflections from the surface of the ice and the surface of the water were easily observed, because of their relatively large amplitudes. (See Figure 5.4a,b)

In order to isolate the diffracted pulse from the total waveform we digitised the waveforms. The diffracted waveforms were digitised using the TEK 4010 digitiser. Software written by Lisa Belec of Thayer School of Engineering was used to download the data. The data was manipulated and plotted using Microsoft Excel 2.2 ®.

The waveforms were assumed to be linear between peaks and so only the peaks were recorded. The -35 cm reflection data, (which was taken 35 cm away from the edge under the ice) was considered to be purely reflection from the ice. This waveform was then superimposed and subtracted from the other (-35 to 0 cm) waveforms. The resultant waveform was assumed to be the diffracted arrival from the edge of the ice. Similarly, the 50 cm waveform (50 cm away from the edge, under the water) was considered to be exclusively reflection from water. This waveform was subtracted from the 5cm to 45 cm waveforms, to isolate the diffracted arrival.

There were several constraining factors that limited the sophistication of this approach. First, the photographs of the waveform was enlarged optically using a photocopier. The resulting enlargement was then mounted on a grid that determined the coordinates of the points that were to be digitised. Finally, the waveform was manually traced by clicking the cursor on the appropriate peaks and troughs. Each stage of this transfer of data might result in errors in the amplitude and travel times of the signal waveform.

Figure 5.2: The diffracted signal was observed directly, without interference only when the transducers were under water. Under the ice, the reflection from the ice interfered with the diffracted arrival.

Diffraction Travel times for ice edge
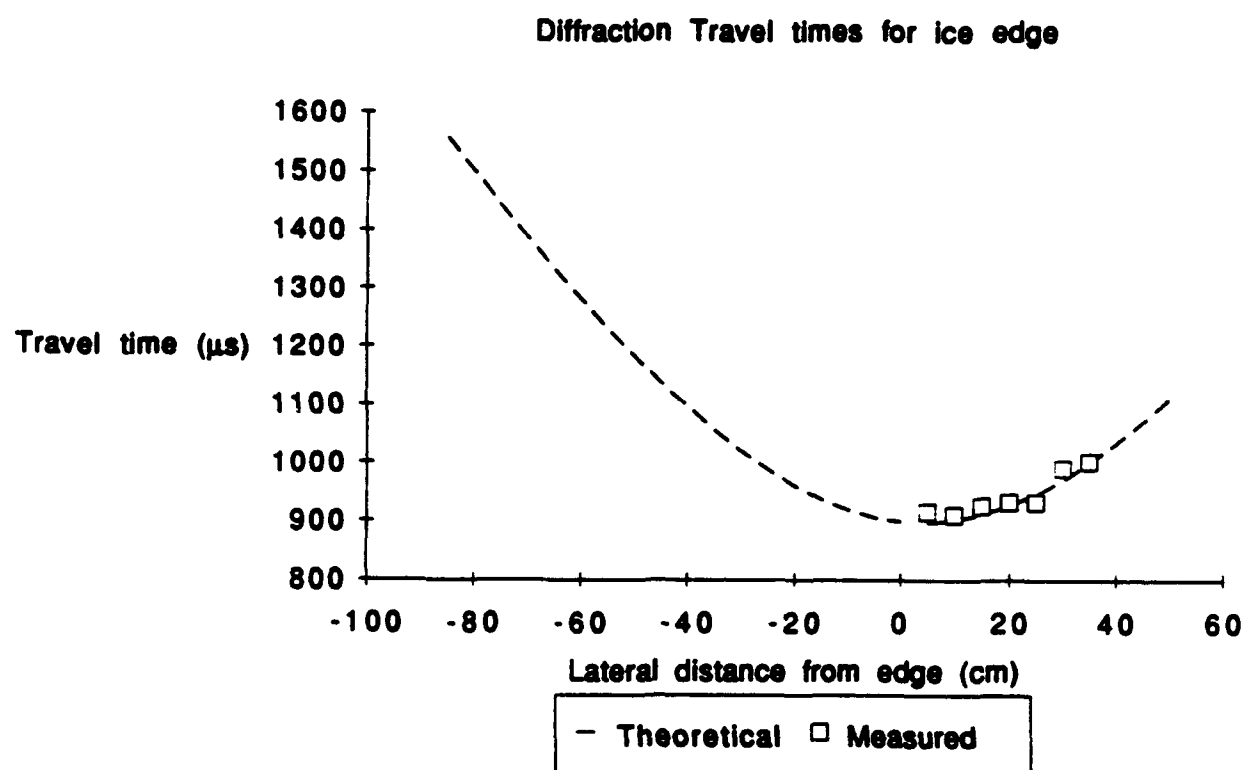
Figure 5.3a: The diffracted signal from the water edge was observed directly, without interference only when the transducers were under ice. Under the water, the reflection from the open water interfered with the diffracted arrival.

Diffraction Travel times for water edge
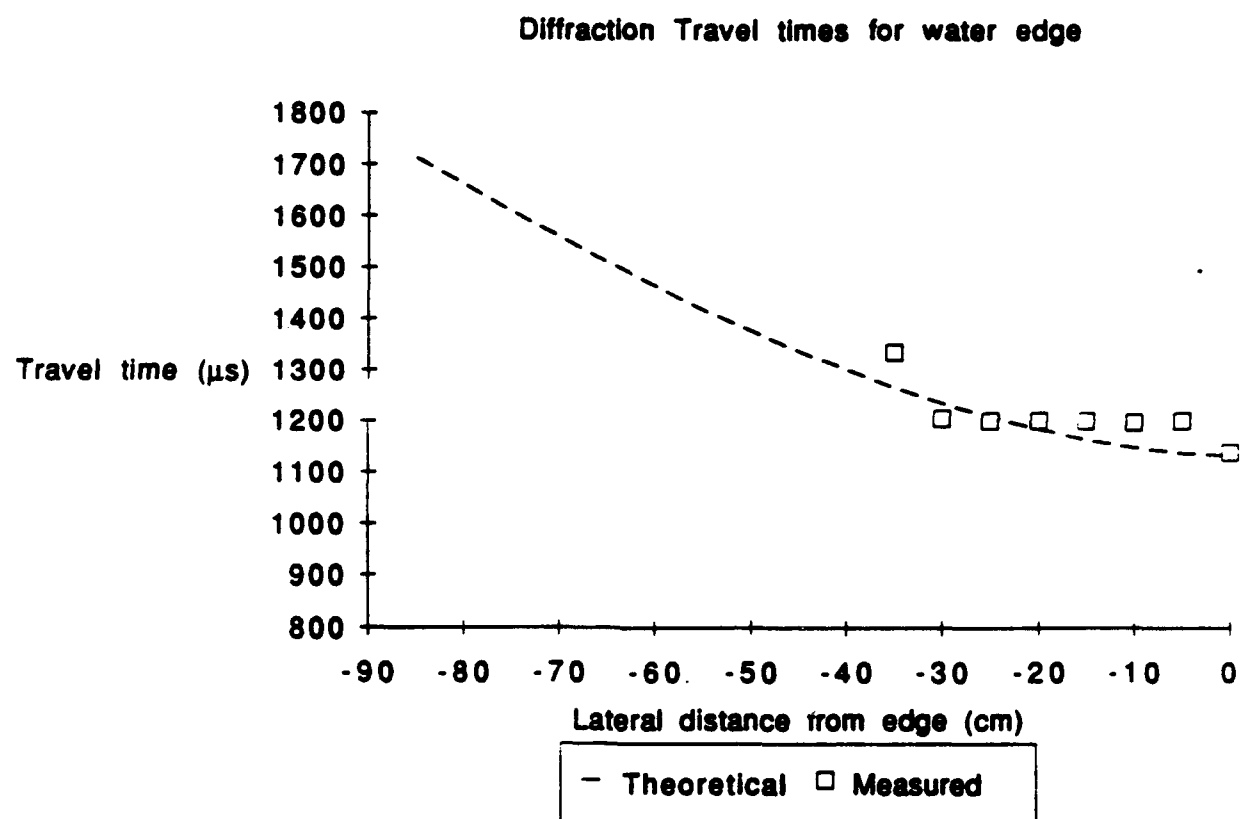
Figure 5.3b: The amplitude of the signal from the water edge could be observed directly when the transducers were under the ice. The amplitude increased gradually as we got nearer to the edge, qualitatively following the expected pattern.

Diffraction from water edge
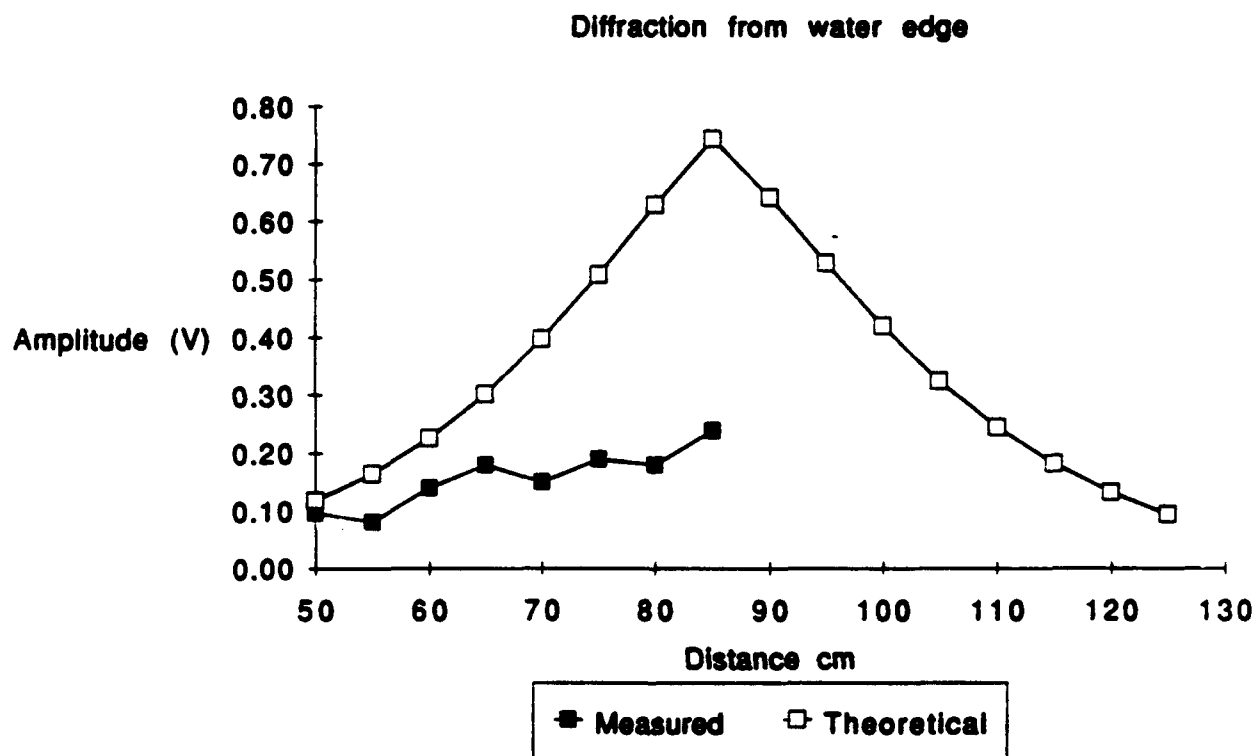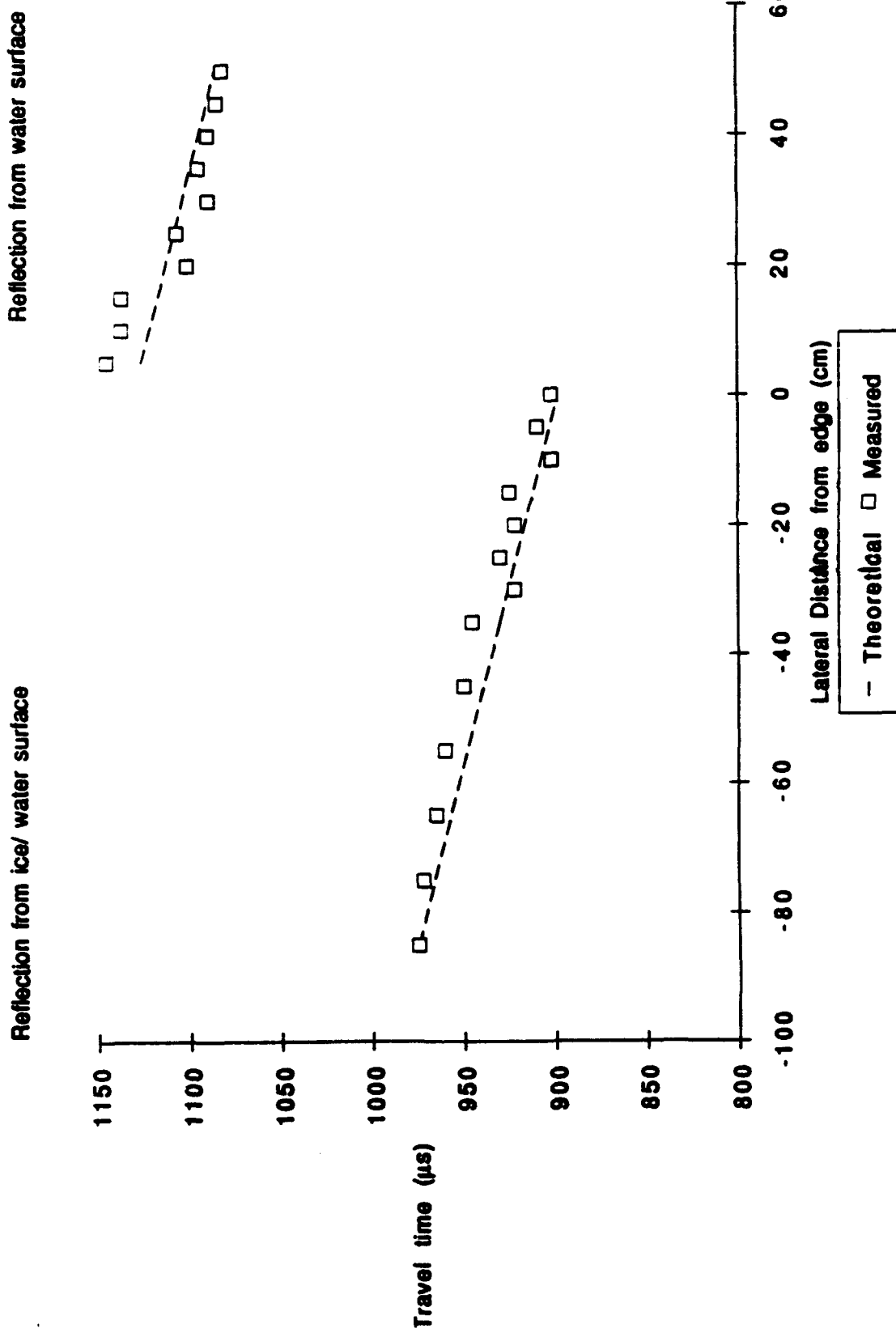
Figure 5.4₁;The travel times to the surface of the ice and the water decreased as the transducers were moved because of the incline of the transducer support.
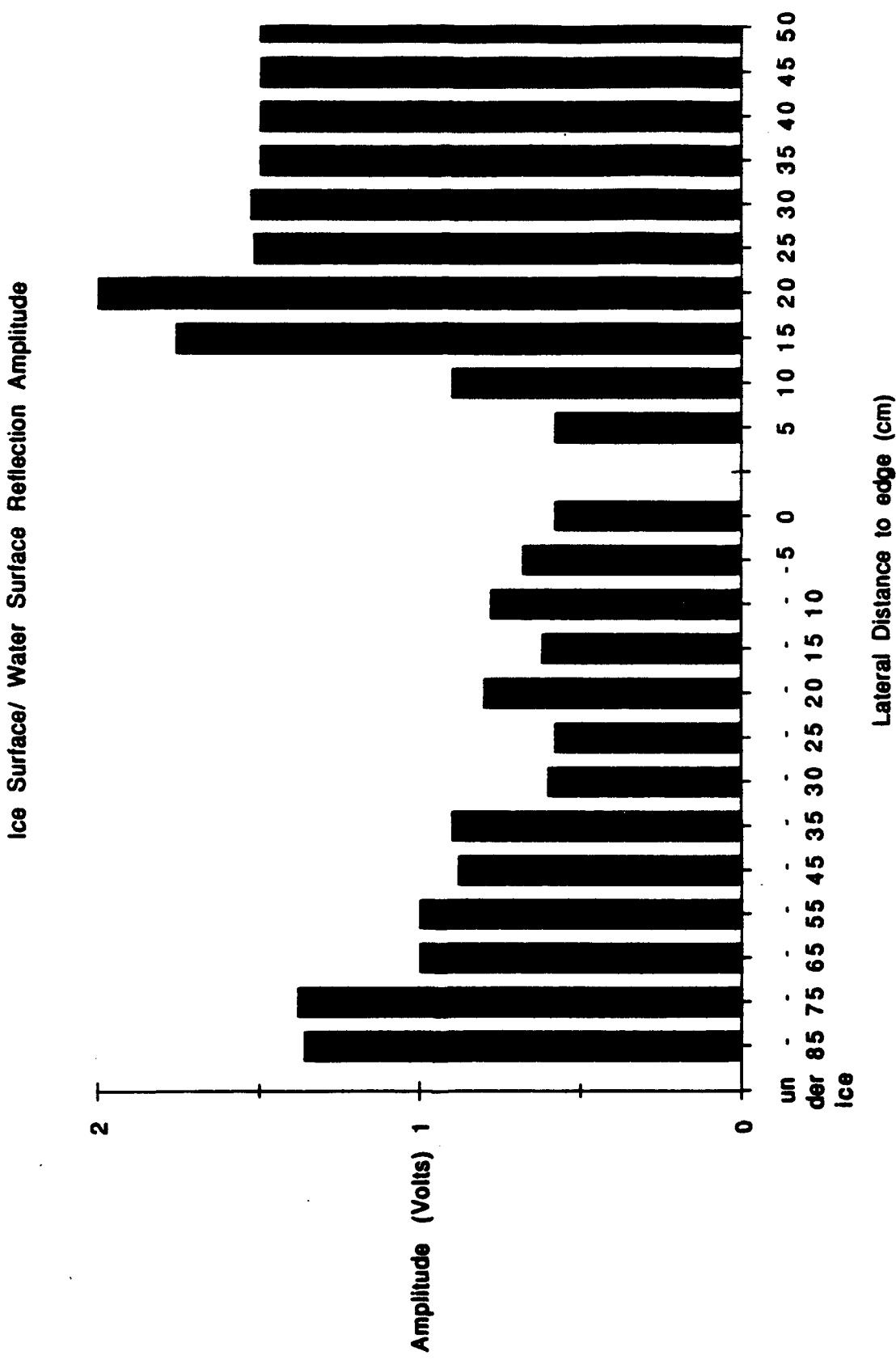
Figure 5.14 The amplitude of the reflections from the ice and the water was not stable, indicative of the interference from the diffracted arrival and possibly other reflections.

The next stage of the data reduction process involved isolating the diffracted arrival by subtracting the waveforms from each other. The -35 cm waveform was considered to consist of only an ice reflection. This waveform was subracted from the -30 to 0 cm waveforms by aligning the first peak of the two signals (See Figure 5.5). The following peaks were then considered aligned because no abrupt change in phase was observed, and any discrepancies were attributed to the data transfer process. The signals were then subtracted and the resultant waveform was considered to be the diffracted arrival since there were no other arrivals expected in that time frame.

For the case where the transducers were below the water the 50 cm waveform was considered to comprise of only an open-water reflection. This waveform was subtracted from the 5-30 cm waveforms. The diffracted arrival was observed before the reflection from the water. Hence, the two waveforms could no longer be aligned by comparing their first peaks. Instead, their maximum peaks were aligned, assuming that the reflection from the water was steady enough and large enough relative to the diffracted arrival to be unaffected by the interference of the diffracted arrival (See Figure 5.6). The most significant limitation of this approach was that by pre-aligning the peaks, phase changes in the diffracted signal arrival could not be accounted for. In addition, because only the peak values had been recorded, the subtraction process was extremely sensitive to the proper alignment of the

peaks. In effect, a 45° phase difference could dramatically alter the results of the subtraction of two waveforms; from a subtraction between two peaks to a subtraction of a trough from a peak.

Figure5.5: Shows subtracted waveform.
    a)Only ice surface reflection waveform (-35 cm)
   b) under ice waveform
    c) resultant diffracted arrival

(a) -35 cm
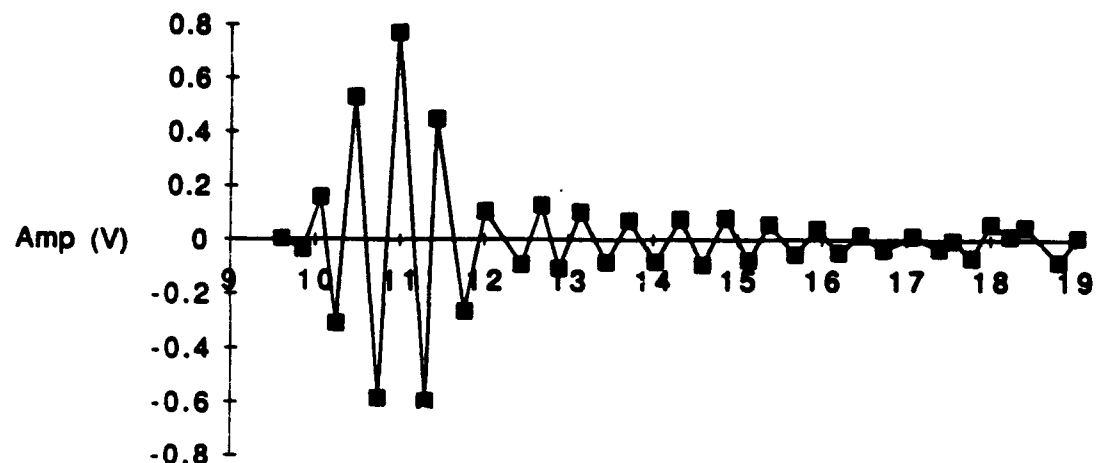
(b) -15cm
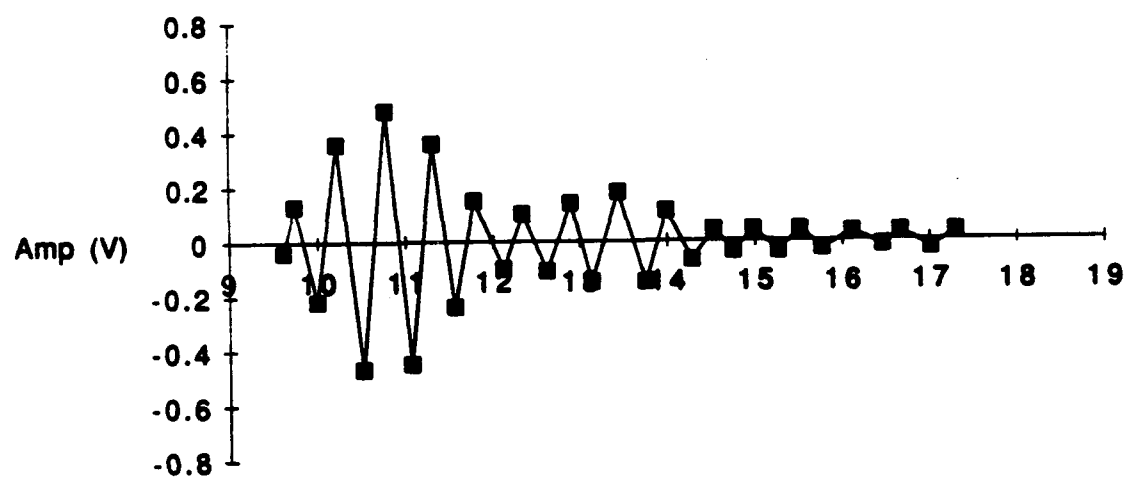
(c) -15 diffraction
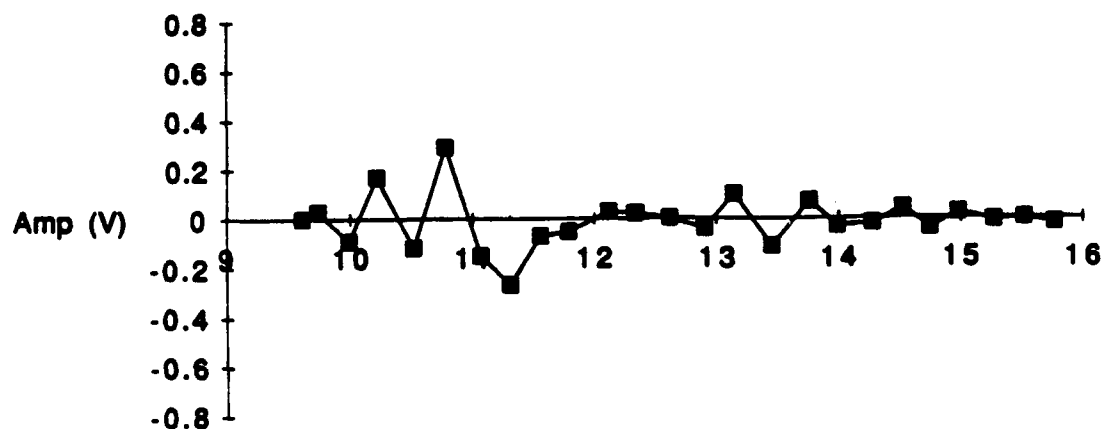
Figure5.6: Shows subtracted waveform.
a)Only open water reflection waveform (50 cm)
b) under water waveform
c) resultant diffracted arrival

(a) 50 cm

(b) 15 cm
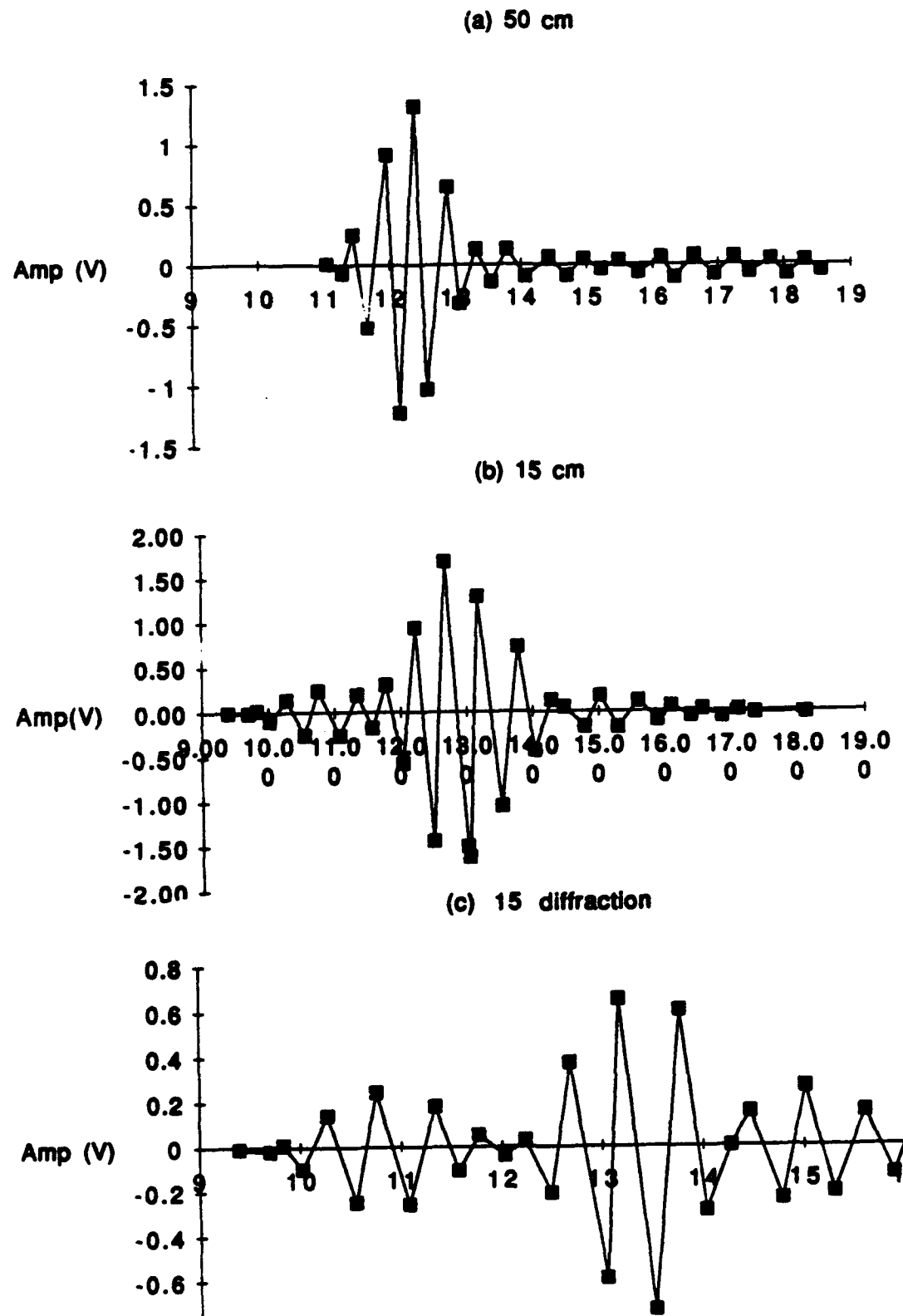
(c) 15 diffraction

5.3 Observations:

The amplitude of the diffracted signal was recorded by visual observation of the the received waveform. However, the pulsewidth of the signal (almost 200 μs), caused the reflection from the the ice sheet to dominate the diffracted arrival when the transducers got within 25 cm laterally from the edge. In addition, interference between the arrivals from the water edge and the ice edge was observed. When the transducers were under the water the beginning of the diffracted arrival was observed upto about 20 cm away from the edge, after which most of the difracted arrival was swamped by the reflection off the open-water. Close to the edge there was considerable interference between the reflection from the open-water and the edge of the water as well as the bottom of the ice sheet.

In order to isolate the diffracted arrival from the waveform, we employed the subtraction procedure described above. When the transducers were under the ice, the diffracted signal was recovered by subtracting the under-ice signal from the total reflected signal. Similarly when the transducers were completely under water, the diffracted signal was recovered from the total signal by careful subtraction of the open-water signal from the total reflected signal.

In order to compare these values we developed a diffraction model on the

basis of the theory in Section 5.1. For the case where the transducers were under the ice, it was assumed that the ice sheet was an infinite strip with one edge being the diffracting edge and the other edge being at infinite distance. Assuming the incident signal to be an impulse function, the values for the reflection from the ice sheet were derived using the first part of equation 7. To calculate the peak value of the impulse response of the diffracted signal, equation 8 was used to find the instantaneous value of $D(t=T)$, and then combined in equation 7 to derive the peak value of the diffracted signal. The signal was normalized by dividing the diffracted arrival by the reflected arrival. This gave us a ratio that when multiplied by the reflection from the ice gave us the theoretical value of the diffracted signal. Finally, the signal was compensated for the beam pattern effects of the transducers to get the theoretical value received at the receiver. These values were compared to the peak values that we observed and the values derived from the subtraction. (See Figures 5.7a, 5.7b, 5.7c)

There are several assumptions made in the model in order to simplify the computation. The model is strictly only valid for the region where the transducers are under the ice sheet. Once the transducers are under the water then the diffracting edge is no longer illumined on only one side. In order to properly account for the diffraction, the vertical face of the ice sheet would have to be taken into consideration. This would require that a value for $D(t)$ be computed for this second sheet and then superimposed on the value

computed for the horizontal sheet. However, the effective surface area of the vertical sheet is very small compared to the total area illumined by the transducers. We have assumed in the model that the source is a spherically radiating source. A compensation for beam pattern, which assumes that the entire edge is equally illumined, has been made. However, the beam pattern of the transducers, causes the different positions along the edge to be illumined at different intensities. The assumption may be justified because at 20 kHz the beam pattern is approximately 50°, which is sufficiently wide. The model assumes that the source is an impulse function. Accordingly, it calculates the impulse response of the reflected and diffracted arrivals. However, the amplitude of $D(t)$ at $t=T_1$ is infinity. We handle this infinity and the source function infinity as shown in Equation 8. The value of Δ, the time interval, affects the computation of $D(t)$ since $D(t)$ is inversely proportional to the square root of Δ. The value of the reflected signal is inversely proportional to Δ. The net effect is that increasing Δ causes the diffracted values to increase at a more gradual rate. (See Figures 5.7a, 5.7b, 5.7c) Assuming Δ to be the pulsewidth of our signal (i.e. 200μs) we were able to get a reasonably good fit, within ± 10%, with the subtraction data. Surprisingly the observed data fit the model very well for the region where the transducers were below the water. This might indicate that the effect of the vertical edge does not form a substantial part of the total diffracted arrival.

Diffraction Values delta = 10µs
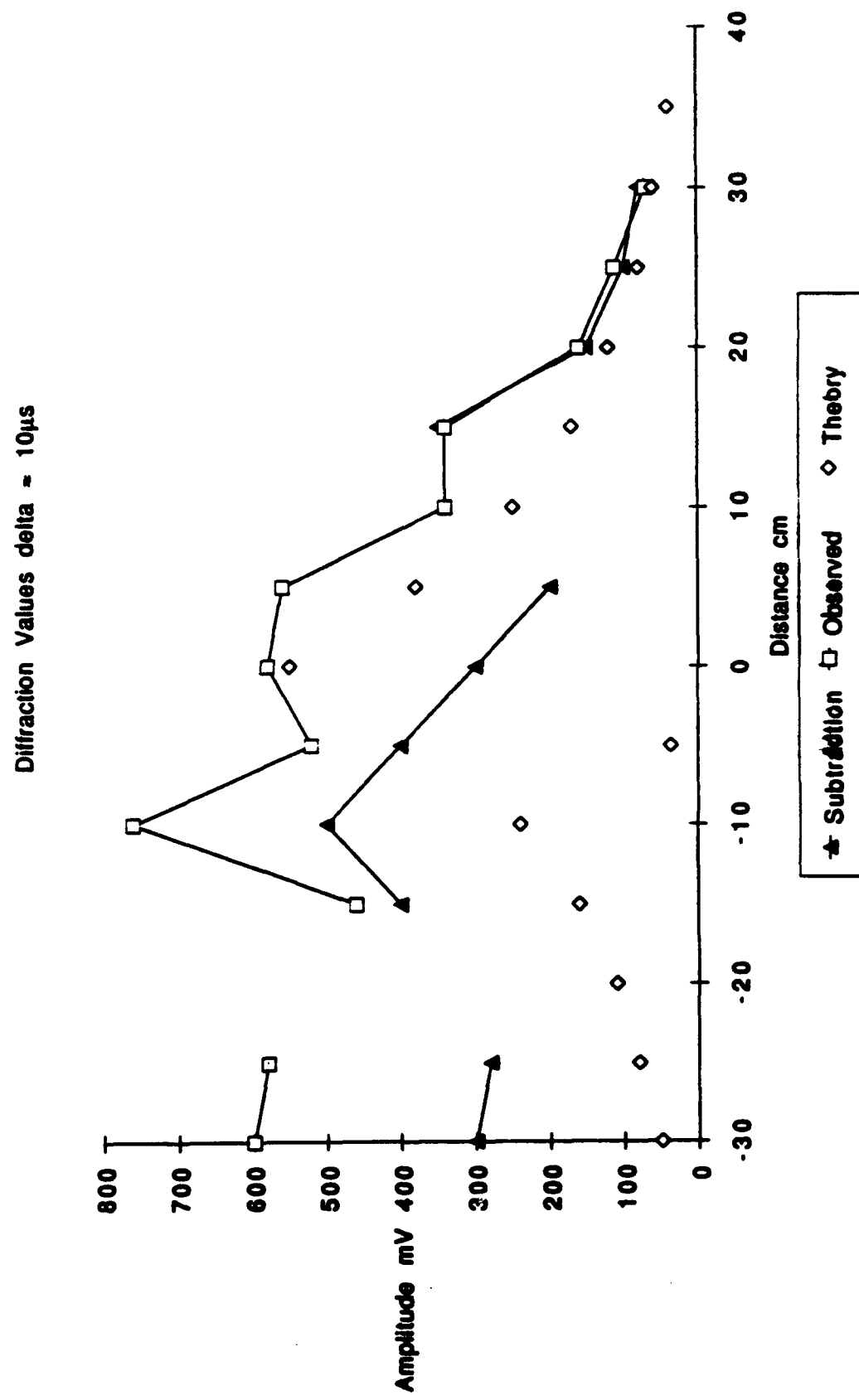
Figure 5.7a: Theoretical values of diffracted arrival using a time step of 10µs compared to the observed arrivals and the values of the diffracted arrivals obtained by subtraction analysis.
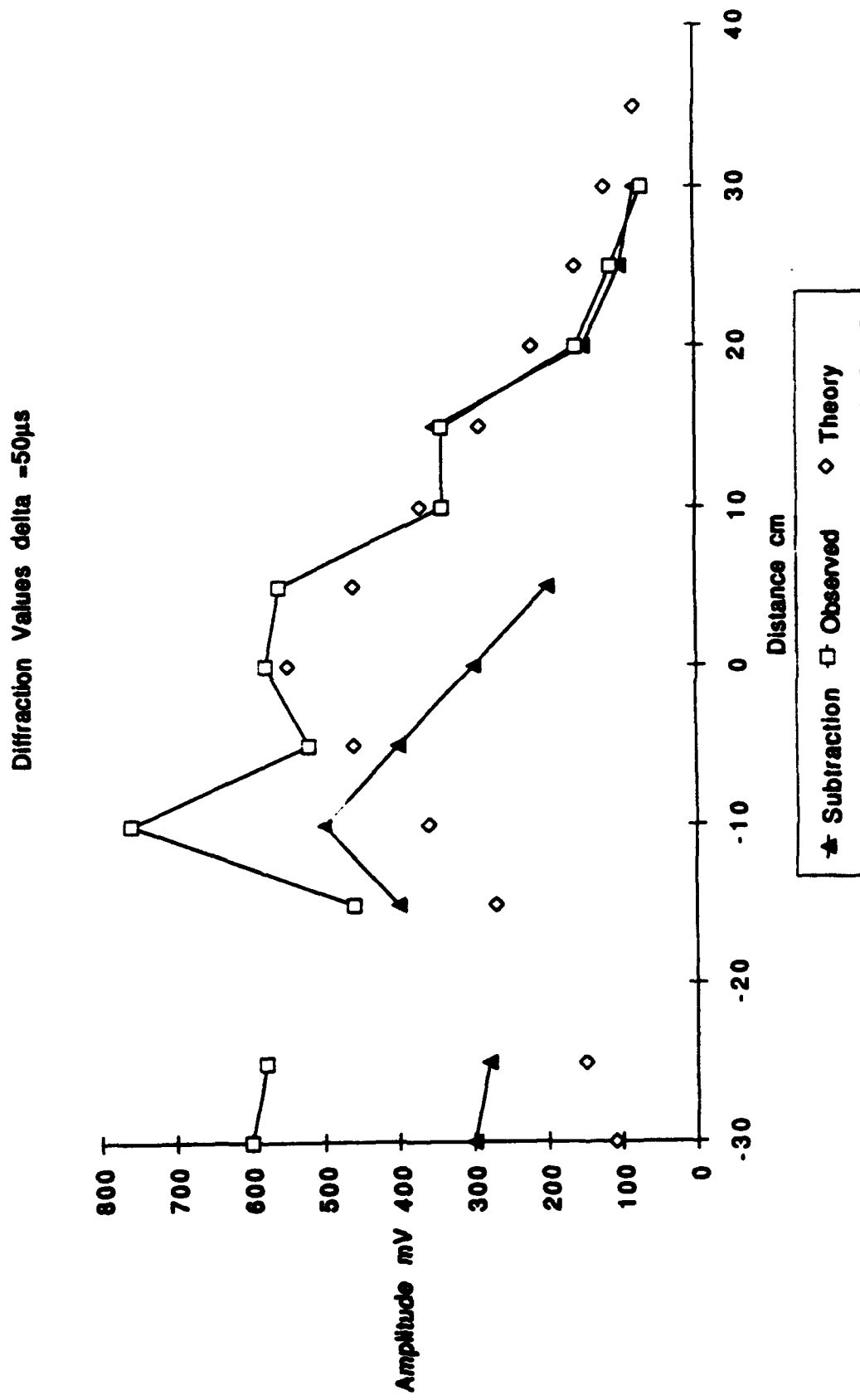
Figure 5.7b: Theoretical values of diffracted arrival using a time step of 50µs compared to the observed arrivals and the values of the diffracted arrivals obtained by subtraction analysis.
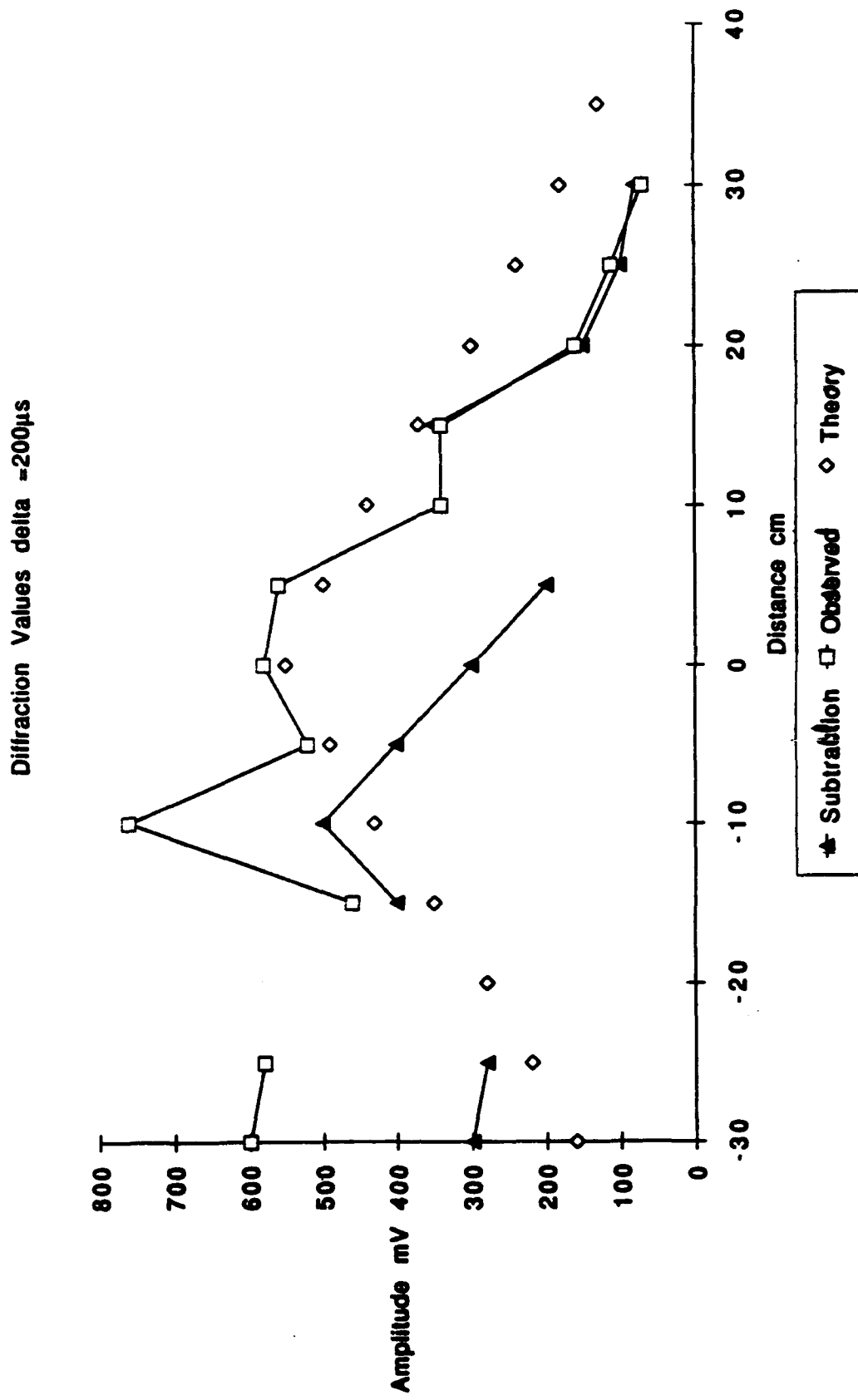
Figure 5.7c: Theoretical values of diffracted arrival using a time step of 200μs compared to the observed arrivals and the values of the diffracted arrivals obtained by subtraction analysis.

6. Error Analysis:

The measurement error in the 1/R calibration data could be averaged to be about 10%. This error accounts for the instability we noticed in the system for the duration of the experiment. In fact, considering that the transducers had been removed from the water and soaped before re-calibration, the actual calibration error may be even less. The reflection coefficient, R, is a function of two independent variables

$$R = \frac{Signal}{Calibration}$$

The signal error and the calibration error are considered statistically independent processes. Taking the derivative, and eliminating the cross terrms, we find that

$$\% \ error = \frac{dR}{R} = \left(\left(\frac{dSigl}{Sigl} \right)^2 + \left(\frac{dCal}{Cal} \right)^2 \right)^{\frac{1}{2}}$$

For 190 kHz, $\left(\frac{dSigl}{Sigl} \right)^2$ is negligible. This is determined by knowing the shape of the distribution to be Gaussian and thereby determining the error in the mean. The specific process to derive the standard deviation is derived in the Section 4.3. Therefore the resultant error is simply,

$$\frac{dCal}{Cal} = 23 \ \%$$

But this can largely be attributed to the fact that the narrow total beamwidth of the 190 kHz transducers, $2\text{Sin}^{-1}(1.15/ka) = 5.2°$, coupled with the finite spacing between them leads to a variation in the $1/R$ dependence when the transducers are close to the water surface.

At the lower frequencies we note that the reflaction coefficient does not lend itself to a percentage error calculation. The standard deviations of the data points are summarised as follows:

Table 6.1

Frequency	S.d. (Data)	S.d. (PDF)
15 kHz	0.09	0.014
17kHz	0.08	0.021
20kHz	0.08	0.014
25kHz	0.1	0.012
190kHz	0.04	0.004

The errors in the reflection coefficient may arise from various factors in the system. The error in measuring the correct travel time and amplitude owing to misplacing the cursor on the waveform, especially when the waveform does not show a steady state signal, might lead to catastrophic errors. The lower error in the 190 kHz data may be attributed to the fact that the transmit/receive electronics was devoid of amplifiers that have an error

associated with them.

All the reflection coefficient measurements were pegged against the value of the reflection coefficient off the open water. Even though only one measurement was made at 0 thickness, the calibration value was very stable. The calibration errors for the lower frequencies are summarised below.

Table 6.2

Frequency	Calibration error percentage
15 kHz	7%
17kHz	7%
20kHz	10%
25kHz	11%

This error takes into account the robustness of the system during the course of the experiment. It may be biased high since the transducers were removed from the water before recalibration, necessitating resoaping of their surface. This might have led to the higher amplitudes observed in the post experiment calibration.

The plane-wave reverberation model used to predict the bulk acoustic properties of the ice sheet was sensitive to the various parameters. At 190 kHz, a wide range of velocities, from 3200 m/s 4200 m/s, fit the theoretical plot to the data. Because of the limited number of data points at the thin ice thicknesses (upto 3 cm), the attenuation could be varied between

2.5 dB/cm to 3.4 dB/cm. The value of the reflection coefficient was relatively stable around 1.2 ± 0.025. One additional facet of error that might not be reflected in the model is the lateral shift of the data owing to errors in the thickness of the ice. Over the entire pool the ice varied in thickness ± 1 cm from the area that we collected our samples from. As the transducers swept an arc of almost 1 m radius the ice thickness may have varied from 0.5-1 cm. This might help explain some of the discrepancy in the position of the peaks and troughs in the thin ice thickness data.

For the lower frequencies, the model was much more sensitive to changes in the velocity parameter. The velocity could be varied between 3650 m/s and 3900 m/s before a noticable difference in the model fit could be observed. At 25 kHz the velocity could be varied between 3900-4100 m/s. The attenuation at the lower frequencies was very low and variation in the attenuation parameter caused the sharpest differences in the values of the reflection coefficient at the nulls. A range of attenuations is used to fit the model to the theory. At the lower frequencies, the attenuation values that fit the thin ice data best were about 10-15% lower than those that fit the thicker ice data. This indicates that the ice could be better modeled using a multi-layered model. However, the attenuation change was not very large. A summary of the attenuation values used to fit the data is given below:

Table 6.3

Frequency	Range of attenuation values	Model value
15 kHz	0.27-0.43 dB/cm	0.27 dB/cm
17kHz	0.17-0.43 dB/cm	0.28 dB/cm
20kHz	0.21-0.34 dB/cm	0.31 dB/cm
25kHz	0.26-0.43 dB/cm	0.35 dB/cm

The values of the reflection coefficients varied between ±0.5 of their final values. The values of the reflection coefficients of the bottom layer derived from the subtraction data varied within ±14 % of those derived using the model.

For the beam pattern analysis, we observed a strong correlation between the theoretical and measured beamwidths. In the case of the beam pattern tests done parallel to the shaft on which the transducers were attatched, we noticed that the measured loss was within 1 dB of the theoretical estimates. In the case of the beam pattern tests done perpendicular to the shaft, we noticed that the measured power values were 2-3 dB higher than the theoretical predictions when the target was above the receiving transducer. When the target was over the transmitting transducer, the measured values were 2-3 dB lower than the theoretical predictions. This might be owing to the shape of the bulb which was not a perfectly spherical target. Its reflectivity may have varied as a function of its position over the transducers. Overall, the

difference in theoretical and measured beamwidths was about 10%.

Although the diffraction model was strictly valid only under the ice sheet, the model values fit the data fairly closely, especially when allowances are made in the value of the time interval, Δ. Changing the value of Δ smoothed the curve of the diffraction amplitude as it peaked just below the edge of the ice. The subtraction method we used was subject to limitations described above, the most severe of which were experienced when the transducers were under the water. The results of the subraction analysis are within 20-25 % of the theoretical predictions when the transducers are under the ice sheet. However, under the water they are almost an order of 2 lower than the theoretical values. The observed values of the diffraction data follow the opposite trend. Since the diffraction signal was swamped by the ice reflection 25 cm from the edge, no direct observations were possible. However, when the transducers were below the water, the diffracted signal could be observed directly. Using a Δ of 50 μs, the theoretical model predictions were within $\pm 10\%$ of the observed value of the diffracted signal.

7. Conclusion:

In conclusion, we propose that the dendritic water-ice interface plays a critical part in the attenuation and normal incidence reflection of acoustic energy from the ice sheet. A small variation in the morphology of this interface may cause a significant variation in the bulk acoustic properties of the ice. A qualitative study of the interface reveals urea ice dendrites that are much wider and sturdier than the saline ice dendrites. Although the morphology of the urea and saline ice seem similar, urea ice has significantly higher reflection coefficients than saline ice at the tens of kHz range. In the hundreds of kHz region, the data is more comparable to contemporary studies done on saline ice. Attenuation rates are lower than those observed for saline ice. We hypothesize that the difference may be a result of dissimilarities in the concentration of the liquid filled pockets, due to the difference in the brine incorporation mechanism between the two ice types.

From the above, it might therefore be concluded that urea ice is a viable simulant for saline ice in acoustic experiments at the hundreds of kHz frequencies but may not be a suitable substitute at the tens of kHz frequencies.

A comparison of the normal incidence refelection coefficients observed for several types of cold saline ice and freshwater ice at 188kHz is summarised below. Laboratory data were collected using facilities at the US Army Cold Regions Research and Engineering Laboratory. Field data for saline ice types were collected in the Fram Strait while data on fresh lake ice were collected on a small lake near CRREL. Total measurement error for all data types was ±10%.

Table 7.1

Ice Type		Reflection Coefficient	
		Laboratory	Field
Saline	New	0.04	0.09
	Cellular	0.12	0.16
	Altered		0.27
	Slush	0.42	
Fresh Lake			0.4
Urea	15kHz	0.6	
	17kHz	0.4	
	20kHz	0.35	
	25kHz	0.4	
	190kHz	0.12	

The phase velocity of the acoustic wave in ice was found to be 3800m/s ± 5%. This velocity is in agreement with that observed by others as summarised in the table from Wallerstedt et al. below:

Table 7.2:

Principal Author	Velocity (m/s)
Bunney	3840
Bennet	3830
Clarke	3817
Bogorodski	3800
Roethlisberger	3960
McCammon	3593
& McDaniel	3832
Wallerstedt	3387
Vahanvaty	3800

Finally, the diffraction values were in agreement with those predicted using simple Helmholtz-Kirchoff theory. It appears that the vertical edge of an ice lead may not contribute significantly to normally incident acoustic backscatter from the edge.

8. Further work:

Much further work could be done in order to bettter interpret the results
of this experiment. The plane-wave reverberation model may be enhanced by
assuming a multi-layered ice-sheet. This would allow a better fit between the
data and theoretical predictions since there would be a greater number of
parameters to vary. We could then account for the ice properties like
attenuation that change as a function of thickness. In order to make a more
rigorous comparison of the urea ice results with saline ice, the experiment
could be repeated using the identical set-up and equipment, using a sheet of
saline ice.

Tests to measure the urinity profile of the ice sheet might determine infact
if there is a difference in the brine inclusion processes of urea and saline ice.
A more quantitative study of the denoritic interface would also substantiate
the hypothesis that there is a qualitative difference in the dimensions of the
dendritic interface of the two ice types.

Better transducers, with resonances that allow greater signal to noise ratios
and shorter pulsewidths, would greatly improve the results of the diffraction
phase of this experiment. This would also allow us to study the change in
backscatter from the edge of a lead, as the acoustic properties of the ice change
as a function of its thickness.

Further work might include developing a more sophisticated signal processing technique to isolate the diffracted arrival from the reflected pulse. As an improvement I would definitely recommend automating the data gathering process. Not only would this alleviate the long and tedious task of monitoring the growing ice sheet but it might also allow digitisation of the waveforms, thereby permitting more sophisticated signal processing of the received pulses.

1/RCalibration table

Pre experiment Calibration

travel time μ:	15Khz Voltage (mV)	17Khz (V)	20kHz (V)	25Khz (V)	190kHz (mV)
840	800	2	3.16	1.24	125
1215	520	1.32	2.2	0.9	190
1145	560	1.44	2.36	0.94	200
1080	640	1.5	2.5	0.94	172
1011	680	1.68	2.64	1	200
945	690	1.9	3	1.04	212
875	800	2.04	3.4	1.1	216
800	840	2.2	3.56	1.24	·180
900	800	2.16	3.7	1.28	
1140	560	1.6	2.6	1.12	
1078	620	1.76	2.72	1.08	
1008	700	1.52	3.28	1.28	
940	800	1.68	3.7	1.32	
870	640	2.08	3.92	1.48	
800	760	2.24	4.2	1.6	

Post Experiment Calibration

t t	15kHz	17kHz	20kHz	25kHz	190kHz
Mean tt	976.47				
Mean Pre	691.25	1.76	2.85	1.05	~~186.88~~
Mean Post	697.14	1.86	3.45	1.31	
Mean Prepost	694.00	1.81	3.13	1.17	186.88

Table 1

1/RCalibration table

	Travel time* voltage				
:	15Khz	17Khz	20kHz	25Khz	190kHz
Pre Experiment	672000	1680	2654.4	1041.6	105000
	631800	1603.8	2673	1093.5	230850
	641200	1648.8	2702.2	1076.3	229000
	691200	1620	2700	1015.2	185760
	687480	1698.48	2669.04	1011	202200
	652050	1795.5	2835	982.8	200340
	700000	1785	2975	962.5	189000
	672000	1760	2848	992	144000
Post Experiment	720000	1944	3330	1152	
♦	638400	1824	2964	1276.8	
	668360	1897.28	2932.16	1164.24	
	705600	1532.16	3306.24	1290.24	
	752000	1579.2	3478	1240.8	
	556800	1809.6	3410.4	1287.6	
	608000	1792	3360	1280	
STDeviations Pre	24654.91	74.27	115.55	45.65	42531.04
STDeviations Post	68206.28	155.13	216.82	59.45	
STDeviations Pre Pos	47985.62	119.81	304.59	124.26	42531.04
Mean Pre	668466.25	1698.95	2757.08	1021.86	185768.75
Mean Post	664165.71	1768.32	3254.40	1241.67	
Mean Prepost	666459.33	1731.32	2989.16	1124.44	185768.75

Error percentages = stdev/ mean					
Pre	0.04	0.04	0.04	0.04	0.23
Post	0.10	0.09	0.07	0.05	
Prepost	0.07	0.07	0.10	0.11	0.23

Table

Beam pattern analysis

Post calibration Beam pattern analysis

Perpendicular to shaft   depth=   52.29

lat dist	amplitude:	tt µs	tot. distance		P/P0	angle	power dB	Theoretical
40	68	997	65.8		0.68	37.41	-3.32	-6.19
35	82	950	62.9		0.75	33.80	-2.48	-5.16
30	88	900	60.3		0.74	29.84	-2.61	-4.12
25	116	842	58.0		0.90	25.55	-0.90	-3.09
20	120	812	56.0		0.87	20.93	-1.20	-2.13
15	100	785	54.4		0.68	16.01	-3.29	-1.28
10	120	780	53.2		0.79	10.83	-2.08	-0.60
5	136	747	52.5		0.87	5.46	-1.22	-0.16
0	158	747	52.3		1.00	0.00	0.00	0.00
-5	124	777	52.5		0.79	-5.46	-2.03	-0.14
-10	108	782	53.2		0.71	-10.83	-2.99	-0.57
-15	92	800	54.4		0.63	-16.01	-4.01	-1.25
-20	88	827	56.0		0.64	-20.93	-3.90	-2.11
-25	76	875	58.0		0.59	-25.55	-4.57	-3.08
-30	0	0	60.3		0.00	-29.84		-4.12
-35	0	0	62.9		0.00	-33.80		-5.16
-40	0	0	65.8		0.00	-37.41		-6.19

Parallel to shaft   depth=   52.29

lat dist	amplitude	tt µs	tot. distance		P/P0	angle	power dB	Theoretical
35	52	912	62.9		0.50	33.80	-5.51	-5.69
30	68	897	60.3		0.59	29.84	-3.92	-4.18
25	92	832	58.0		0.74	25.55	-1.98	-2.90
20	115	805	56.0		0.87	20.93	-0.65	-1.86
15	120	775	54.4		0.85	16.01	-0.78	-1.04
10	144	762	53.2		0.98	10.83	0.43	-0.46
5	165	757	52.5		1.10	5.46	1.38	-0.12
0	152	722	50.5	50.54	0.93	0.00	0.00	0.00
-5	128	752	50.8		0.85	-5.65	-0.82	-0.12
-10	112	756	51.5		0.77	-11.19	-1.73	-0.46
-15	100	722	52.7		0.72	-16.53	-2.31	-1.04
-20	64	805	54.4		0.49	-21.59	-5.66	-1.86
-25	52	825	56.4		0.43	-26.32	-6.82	-2.90
-30	0	870	58.8		0.00	-30.69		-4.18
-35	0	0	61.5		0.00	-34.70		-5.69

	Beamwidth	
	Measured	Theoretical
Perpendicular	45	50
Parallel	45	52

Table

Beam pattern analysis

Pre calibration Beam pattern analysis
Perpendicular to shaft   depth=   52.5

lat dista	amplitude:tt	μs	real distance	P/P0	angle	power dB	Theoretical
40	72	985	66.0	0.73	37.30	-2.74	-6.19
35	80	930	63.1	0.74	33.69	-2.61	-5.16
30	92	877	60.5	0.78	29.74	-2.13	-4.12
25	128	820	58.1	1.01	25.46	0.06	-3.09
20	135	795	56.2	0.99	20.85	-0.08	-2.13
15	140	787	54.6	0.97	15.95	-0.26	-1.28
10	152	780	53.4	1.01	10.78	0.08	-0.60
5	152	760	52.7	0.98	5.44	-0.15	-0.16
0	156	750	52.5	1.00	0.00	0.00	0.00
-5	152	777	52.7	0.98	-5.44	-0.15	-0.14
-10	120	797	53.4	0.80	-10.78	-1.97	-0.57
-15	112	805	54.6	0.78	-15.95	-2.20	-1.25
-20	96	835	56.2	0.70	-20.85	-3.04	-2.11
-25	84	872	58.1	0.66	-25.46	-3.60	-3.08
-30	52	925	60.5	0.44	-29.74	-7.09	-4.12
-35	56	950	63.1	0.52	-33.69	-5.70	-5.16
-40	0	0	66.0	0.00	-37.30		-6.19

Parallel to shaft   depth=   53.2

35	0	0	63.7	0.00	33.34		-5.69
30	76	895	61.1	0.70	29.42	-3.15	-4.18
25	88	825	58.8	0.75	25.17	-2.54	-2.90
20	100	812	56.8	0.79	20.60	-2.02	-1.86
15	124	798	55.3	0.93	15.75	-0.63	-1.04
10	136	790	54.1	0.98	10.65	-0.19	-0.46
5	144	780	53.4	1.01	5.37	0.08	-0.12
0	144	760	53.2	1.00	0.00	0.00	0.00
-5	144	785	53.4	1.01	-5.37	0.08	-0.12
-10	128	802	54.1	0.92	-10.65	-0.72	-0.46
-15	120	837	55.3	0.90	-15.75	-0.92	-1.04
-20	96	862	56.8	0.76	-20.60	-2.37	-1.86
-25	72	902	58.8	0.61	-25.17	-4.29	-2.90
-30	60	937	61.1	0.55	-29.42	-5.21	-4.18
-35	0	0	63.7	0.00	-33.34		-5.69

	Beamwidth Measured	Theoretical
Perpendicular	57	50
Parallel	50	52

Table

Reverberation Model :

```
DIM h(500), r(500)

OPEN #1: name "moosedat", access output, create newold, organization text
ERASE #1


PRINT "Alpha -> ";
INPUT alpha


PRINT "Velocity -> ";
INPUT vice


PRINT "Coefficient -> ";
INPUT r12


PRINT "Frequency -> ";
INPUT freq


LET k2 = (2*3.14*freq)/(vice*100)


FOR j = 1 to 220 step 1

    LET h(j) = j/10

    LET u = r12^2 + exp(-4*h(j)*alpha)
    LET u = u - r12*exp(-2*alpha*h(j))*2*cos(2*k2*h(j))

    LET d = 1 + r12^2 * exp(-4*h(j)*alpha)
    LET d = d - r12*exp(-2*alpha*h(j))*2*cos(2*k2*h(j))

    LET r(j) = (u/d)^.5

    SET #1: POINTER END
    PRINT #1: h(j);chr$(9);r(j)

NEXT j


CLOSE #1

END
```

Appendix 3

diffract theory values

	A	B	C	D	E	F	G	H
1	D(t)= (2/(T1^2*D))*arctan((((2*T1*D)^0.5)/TX) for T1<t<T1+D							
2								
3	D(t)= 2*TX/((((t^2+TX^2-T1^2)*(t^2-T1^2)^0.5))) FOR t>T1							
4	Diffraction of ice edge							
5	D(T)= 0 for t<T1							
6	Delta (s)=	0.00005	z (m) =	0.66	R=	0.5041		
7	D(t) for t<T1	Specular r	distanc	T1	TX=2x/c	time(μs)	D(t) for t=T1	u(Q)=(Rz/πc^2)*D(t)
8	0	7638.136	0.001557	0	-0.0012143	1557	-5.184E+09	-280.0850653
9			0.001443	10	-0.0010714	1443	-6.545E+09	-353.6178365
10			0.001333	20	-0.0009286	1333	-8.433E+09	-455.6206778
11			0.001231	30	-0.0007857	1231	-1.109E+10	-598.9377104
12			0.001138	40	-0.0006429	1138	-1.493E+10	-806.4265176
13			0.001056	50	-0.0005	1056	-2.067E+10	-1116.888175
14			0.00102	55	-0.0004286	1020	-2.462E+10	-1330.27646
15			0.000988	60	-0.0003571	988	-2.957E+10	-1597.81178
16			0.00096	65	-0.0002857	960	-3.585E+10	-1936.641957
17			0.000937	70	-0.0002143	937	-4.374E+10	-2363.112727
18			0.000919	75	-0.0001429	919	-5.354E+10	-2892.552134
19			0.000906	80	-7.143E-05	906	-6.519E+10	-3522.15104
20			0.000899	85	1E-99	899	7.7743E+10	4200.233871
21			0.000897	90	7.1429E-05	897	6.6451E+10	3590.165519
22			0.000901	95	0.00014286	901	5.5511E+10	2999.0955
23			0.000911	100	0.00021429	911	4.5952E+10	2482.670341
24			0.000926	105	0.00028571	926	3.8107E+10	2058.807733
25			0.000946	110	0.00035714	946	3.1778E+10	1716.863755
26			0.000971	115	0.00042857	971	2.6672E+10	1440.98874
27			0.001001	120	0.0005	1001	2.2522E+10	1216.784319
28			0.001035	125	0.00057143	1035	1.9147E+10	1034.460873
29			0.001072	130	0.00064286	1072	1.6397E+10	885.8648669
30			0.001113	135	0.00071429	1113	1.4109E+10	762.2844837
31								

diffract theory values

	I	J	K	L	M	N
6			Diffraction from vertical edge			
7	diffracted u(Q)/ specular	u(Q) Theoretical diffracted	time T1	Tx=2x/c	D(t) for t=T1	u(Q)=(Rz/πc^2)*D(t)
8	-0.04	-0.04				
9	-0.05	-0.05				
10	-0.06	-0.06				
11	-0.08	-0.08				
12	-0.11	-0.11				
13	-0.15	-0.15				
14	-0.17	-0.17				
15	-0.21	-0.21				
16	-0.25	-0.25				
17	-0.31	-0.31				
18	-0.38	-0.38				
19	-0.46	-0.46				
20	0.55	0.55				
21	0.47	0.47	0.000897	0.00094286	1.529E+10	6258.340663
22	0.39	0.39	0.000901	0.00094286	1.5187E+10	12431.70684
23	0.33	0.33	0.000911	0.00094286	1.4932E+10	18335.04372
24	0.27	0.27	0.000926	0.00094286	1.4563E+10	23842.8126
25	0.22	0.22	0.000946	0.00094286	1.4094E+10	28843.54845
26	0.19	0.19	0.000971	0.00094286	1.3542E+10	33255.63942
27	0.16	0.16	0.001001	0.00094286	1.2924E+10	37029.16454
28	0.14	0.14	0.001035	0.00094286	1.2278E+10	40204.3004
29	0.12	0.12	0.001072	0.00094286	1.1634E+10	42854.52372
30	0.10	0.10	0.001113	0.00094286	1.0981E+10	44946.9104
31						

Bibliography:

Bishop G., A bistatic, high frequency, under ice acoustic scattering model I, Theory, 1989 *Journal of Acoustical Society of America* 85 p.1903-1911

Bishop G., A bistatic, high frequency, under ice acoustic scattering model II, Applications, 1989 *Journal of Acoustical Society of America* 85 p.1912-1924

Bogorodsky V.V., Smirnov G.E., Smirnov S.A.

Branch G.H., Posey J.W., High frequency acoustic reflection from Arctic ice layers, 1985 *Journal of Acoustical Society of America* Suppl 1 77, S56

Brown J.R.,Brown D.W., Reverberation under Arctic sea ice, 1966 *Journal of Acoustical Society of America* 40 p.399-404

Brown J.R.,Milne A.R., Reverberation under Arctic sea ice, 1967 *Journal of Acoustical Society of America* 42 p.78-82

Chin Bing, S.A. The influence of water/ice layers on the reflection coefficient a..d high frequency backscatter from an ice keel, 1985 *Journal of Acoustical Society of America* Suppl 1 78 p. 557

Chin Bing S.A., Two numerical models-one simplistic, the other sophisticated- applied to under-ice acoustic propagation and scattering, 1987 *Journal of Acoustical Society of America* Suppl 1 82 , S31

Clay C.S., Medwin H., Acoustical Oceanography:Principles and Applications Jnn Wiley and Sons, New York, 1977, 544 pp

Francois R.E., Garrison G.R., Wen T., Reflectivity of sea ice, 1988 *Journal of Acoustical Society of America* 83 Suppl 1 p. S46-S47

Garrison G.R., Francois R.E., Early E.W., Wen T. Comprehensive studies of Arctic pack ice in April 1976, 1978*Applied Physics Laboratory, University of Washington Report No. APL-UW 7724*

Garrison G.R., Francois R.E., Wen T., Stein R.P., Measurements of acoustic reflection from the end of a cylindrical block of arctic ice,*Applied Physics*

Laboratory, University of Washington Report No. APL-UW 8506 42pp

Gow A.J., Crystalline structure of urea ice sheet used in modelling experiments in the CRREL test basin, 1984 *CRREL report CR 84-24* 48pp

Jezek K.C., Radar Investigations of the Ross Ice Shelf, Antarctica, 1980 Doctoral Dissertation, University of Wisconsin- Madison

Jezek K., Stanton T., Gow A., Attenuation of sound through laboratory grown saline ice (abstract), 1987 *Journal of Acoustical Society of America* 82 Suppl 1 p. S30

Jezek K.C. , Stanton T.K., Gow A.J., in press, Acoustic properties of laboratory grown saline ice, 1988. In Proceedings Third International Symposium. Sea ice and Sea of Okhotsk, Monbetsu, Japan

Jezek K.C. , Stanton T.K., Gow A.J., High frequency acoustic properties of saline ice, 1989. In Proceedings, Arctic Technology Workshop, J. Richter-Menge, W.B. Tucker and M.M. Klienerman, eds., CRREL special report 89-39, p 9-23

Jezek K.C. , Stanton T.K., Gow A.J., Lange M.A., in press, Influence of environmental conditions on acoustic properties of sea ice, 1990

Langleben M.P., Attenuation of sound in sea ice 10-500k Hz 1969 *Journal of Glaciology* 8, p. 399-406

Mayor W.G., Behravesh M., Plona T.J. Determination of sonic velocities from Reflectivity losses at sea ice-water boundaries, 1985 *Journal of Acoustical Society of America* 57 p.39-46

McCammon D.F., McDaniel S.T., The influence of physical properties of ice on reflectivity, 1985 *Journal of Acoustical Society of America* 77, p.499-507

Posey J.W., Branch G.H., Chin Bing S.A. and Tango G., High frequency reflection from flat sea ice, *Proceedings of the Arctic Oceanographic conference and Workshop* 11-14 June 1985 p. 80-89

Perey F.J.G., Pounder E.R., Crystal orientation in ice sheets, 1958 *Canadian*

Journal of Physics 36 p494-502

Stanton T.K., Jezek K.C., Gow A.J., Acoustical reflection and scattering from the underside of laboratory grown sea ice: Measurements and predictions, 1986 *Journal of Acoustical Society of America* 80 p.1486-1494

Weeks W.F., Lee O.S. Observations of the physical properties of sea ice at Hopedale, Labrador, 1958 *Arctic* 11 p 134-155